Spectro-photometry of Phobos simulants I. Detectability of hydrated minerals and organic bands

Antonin Wargnier, Thomas Gautier, Alain Doressoundiram, Giovanni Poggiali, Pierre Beck, Olivier Poch, Eric Quirico, Tomoki Nakamura, Hideaki Miyamoto, Shingo Kameda, et al.

Icarus 421 (2024) 116216

Contents lists available at ScienceDirect

Icarus

journal homepage: www.elsevier.com/locate/icarus

Research Paper

Spectro-photometry of Phobos simulants I. Detectability of hydrated minerals and organic bands

Antonin Wargnier [a,b,*], Thomas Gautier [b,a], Alain Doressoundiram [a], Giovanni Poggiali [a,c], Pierre Beck [d], Olivier Poch [d], Eric Quirico [d], Tomoki Nakamura [e], Hideaki Miyamoto [f], Shingo Kameda [g], Pedro H. Hasselmann [h], Nathalie Ruscassier [i], Arnaud Buch [i], Sonia Fornasier [a,j], Maria Antonietta Barucci [a]

[a] LESIA, Observatoire de Paris, Université PSL, CNRS, Université Paris Cité, Sorbonne Université, 5 place Jules Janssen, Meudon, 92195, France
[b] LATMOS, CNRS, Université Versailles St-Quentin, Université Paris-Saclay, Sorbonne Université, 11 Bvd d'Alembert, Guyancourt, F-78280, France
[c] INAF-Astrophysical Observatory of Arcetri, largo E. Fermi n.5, Firenze, I-50125, Italy
[d] Univ. Grenoble Alpes, CNRS, IPAG, Grenoble, F-38000, France
[e] Department of Earth Science, Tohoku University, Sendai, Japan
[f] Department of Systems Innovation, University of Tokyo, 7-3-1 Hongo, Bunkyo-ku, Tokyo, Japan
[g] Rikkyo University, Tokyo, Japan
[h] INAF - Osservatorio di Roma, Monte Porzio Catone, Italy
[i] Laboratoire Génie des Procédés et Matériaux, CentraleSupélec, Université Paris-Saclay, Gif-sur-Yvette, France
[j] Institut Universitaire de France (IUF), 1 rue Descartes, Paris Cedex 05, F-75231, France

ARTICLE INFO

Dataset link: https://doi.org/10.26302/SSHADE/EXPERIMENT_LB_20240713_001, https://doi.org/10.26302/SSHADE/EXPERIMENT_OP_20240717_001, https://doi.org/10.26302/SSHADE/EXPERIMENT_OP_20240717_002, https://dx.doi.org/10.5281/zenodo.11087841

Keywords:
Martian satellites
Infrared spectroscopy
Spectrophotometry
Laboratory astrophysics

ABSTRACT

Previous Mars Reconnaissance Orbiter and Mars Express observations of Phobos and Deimos, the moons of Mars, have improved our understanding of these small bodies. However, their formation and composition remain poorly constrained. Physical and spectral properties suggest that Phobos may be a weakly thermal-altered captured asteroid but the dynamical properties of the martian system suggest a formation by giant collision similar to the Earth moon. In 2027, the JAXA's MMX mission aims to address these outstanding questions.

We undertook measurements with a new simulant called OPPS (Observatory of Paris Phobos Simulant) which closely matches Phobos reflectance spectra from the visible to the mid-infrared wavelength range. The simulant was synthesized using a mixture of olivine, saponite, anthracite, and coal.

Since observation geometry strongly influences the photometry and spectra of the light reflected from planetary surfaces, we evaluated the parameters obtained by modeling the phase curves – obtained through laboratory measurements – of two different Phobos simulants (UTPS-TB and OPPS) using Hapke IMSA model. Our results show that the photometric properties of Phobos simulants are not fully consistent with those of carbonaceous chondrites and martian meteorites. We also investigated the detection of volatiles/organic compounds and hydrated minerals, as the presence of such components is expected on Phobos in the hypothesis of a captured primitive asteroid. To investigate their detectability, we examined the variability of the 3.28 μm and 3.42 μm absorption bands related to aliphatic/aromatic carbon (as a proxy of organic material), as well as the 2.7 μm O–H feature in a Phobos laboratory spectroscopic simulant. The results indicate that a significant amount of organic compounds is required for the detection of C–H bands at 3.4 μm. The bands at 3.28 and 3.42 μm are faint (less than 2%) when ~3 wt% of organic compounds are present in the simulant and are likely undetectable by the MIRS spectrometer onboard the MMX mission. When the concentration of aliphatic and aromatic compounds is increased to 6 wt%, a positive detection starts to become more plausible using remote sensing infrared spectroscopy. In contrast, the 2.7 μm absorption band, due to hydrated minerals, is much deeper and easier to detect than C–H organic features at the same concentration levels. The feature

* Corresponding author at: LESIA, Observatoire de Paris, Université PSL, CNRS, Université Paris Cité, Sorbonne Université, 5 place Jules Janssen, Meudon, 92195, France.
E-mail address: antonin.wargnier@obspm.fr (A. Wargnier).

https://doi.org/10.1016/j.icarus.2024.116216
Received 3 May 2024; Received in revised form 8 July 2024; Accepted 9 July 2024
Available online 14 July 2024

is still clearly detectable even when the simulant contains only 3 vol.% of phyllosilicates, corresponding to 0.7 wt% OH groups.

Posing limits on detectability of some possible key components of Phobos surface will be pivotal to prepare and interpret future observations of the MIRS spectrometer as well as TENGOO and OROCHI cameras onboard MMX mission.

1. Introduction

Phobos and Deimos, the two martian satellites, are the targets of the JAXA Martian Moons eXploration sample return mission (Kuramoto et al., 2022). The origin of the two moons is still not well understood and several hypotheses for their formation have been suggested. According with the in-situ scenario, a giant impact between Mars and a protoplanet would have formed Phobos and Deimos by accretion from a disk of debris originated by Mars and the impactor (e.g., Craddock 1994, 2011, Rosenblatt 2011, Hyodo et al. 2017). In contrast, the asteroid captured hypothesis proposed that the two martian moons were primitive asteroids captured in Mars orbit (Pang et al., 1978; Pajola et al., 2013). More recently, the hypothesis of a captured comet has also been proposed to explain the origin of Phobos (Fornasier et al., 2024).

The detection, or not, of certain specific absorption features on the surface of Phobos may be of major importance to decipher its origin. In particular, organics and hydrated minerals are expected to be present on Phobos surface in the case of the captured asteroid hypothesis. In this theory, to match the spectroscopic observations, Phobos would be a primitive asteroid in the D-type class according to Bus - DeMeo taxonomy (DeMeo et al., 2009). Nevertheless, organics and hydrated minerals have never been unambiguously detected on Phobos (and Deimos) surface since all the past visible and near-infrared observations have shown a red spectrum with a gap in the 2.7 μm region and with no strong absorption bands (Fraeman et al., 2012; Poggiali et al., 2022). This may be due to several reasons: (1) The surface of Phobos may be desiccated and strongly altered by space weathering (Poggiali et al., 2022). (2) The presence of opaque materials could severely reduce the absorption bands (Cloutis et al., 1990, 2009). (3) The size of the grains, which has an impact on the absorption bands, could also prevent their detection as absorption features are shallower for fine grains (Sultana et al., 2021). On the other side, organic compounds have been observed on dark and primitive asteroids, especially for C-, B-, and P-types which can exhibit a 3.4 μm absorption band (Hromakina et al., 2022), as well as on D-type like Jupiter Trojans (Brown, 2016; Wong et al., 2023).

In this context, D-type asteroids, also thought to be very primitive and with a spectral slope close to Phobos spectrum, are particularly rare and seldom observed. They are usually found in the main belt or in the Trojans and known to be spectrally close to comets (Fornasier et al., 2007; Vernazza and Beck, 2017). For the 67P/Churyumov-Gerasimenko comet, a large part of the comet's mass could be associated with organic compounds (Quirico et al., 2016; Bardyn et al., 2017; Choukroun et al., 2020). The Rosetta mission has observed infrared signatures of organics, especially near 3.4 μm due to aliphatic carbon (Raponi et al., 2020). Hence, if Phobos comes from a captured asteroid, it could be expected that organic materials are also found on Phobos.

This range of the spectrum will be measured on Phobos for the first time using the MIRS spectrometer (Barucci et al., 2021) onboard MMX. MIRS is an infrared spectrometer (0.9–3.6 μm) developed by the LESIA laboratory with the support of CNES and several institutions in France and Japan. It will measure Phobos spectra with high spatial and spectral resolution (resp. up to 20 m/px and ~20 nm). The MMX mission will also bring back samples (>10 g) from Phobos to Earth in 2031 which will allow precise measurements of the organic content of Phobos. The visible part of the spectrum will be covered by the OROCHI and TENGOO cameras (Kameda et al., 2021). In particular, OROCHI will observe Phobos with 7 different filters to obtain UV–VIS spectrophotometry: 390 ± 50 nm, 480 ± 30 nm, 550 ± 30 nm, 650 ± 40 nm, 730 ± 40 nm, 860 ± 40 nm, 950 ± 60 nm.

This part of this study is a continuation of the work presented in Wargnier et al. (2023a). We used here different organic compounds (with aliphatic/aromatic signatures) compared to the previous study, which is more representative of the type of organics expected on Phobos in the case of the captured asteroid hypothesis. We searched to assess the detectability of organic materials (i.e. the necessary quantity of organics to detect the bands) in a Phobos spectroscopic simulant by adding different volume fractions of CH-rich organics. We are also interested in the detection level of phyllosilicates in the simulants. The presence of hydrated minerals has already been discussed for Phobos (e.g., Giuranna et al. 2011, Fraeman et al. 2012, 2014, Glotch et al. 2018). The presence of hydrated minerals can provide valuable insights into its origins. The mid-infrared (MIR) spectra of Phobos were analyzed using data from the Mars Express Planetary Fourier Spectrometer (PFS) and the Thermal Emission Spectrometer (TES) onboard Mars Global Surveyor. The results indicate that a linear mixture of antigorite and biotite phyllosilicates can well reproduce the MIR spectrum of Phobos (Giuranna et al., 2011; Glotch et al., 2018). Phobos spectra show also a good agreement with a nepheline spectrum (Giuranna et al., 2011). Antigorite is a phyllosilicate from the serpentine subgroup. Biotite, a bright black mineral, is a phyllosilicate from the micas family. Nepheline, specifically eleolite, is a greyish-brown feldspathoid mineral that is rich in aluminum. Although these three endmembers were detected (as minor phases for biotite and nepheline) in some carbonaceous chondrites (Rubin, 1997) their presence in Phobos composition is not unambiguously expected in the giant impact formation scenario (Sautter and Payre, 2021; Cuadros et al., 2022; Liu et al., 2023). Therefore, we added to our sample set also saponite (McLennan et al., 2014) as a primitive martian crust material. However, interestingly, saponite was also detected as a major component in Ryugu grains (e.g., Nakamura et al. 2023, Nakato et al. 2023). Saponite may be expected to be present in both the giant impact hypothesis and primitive asteroid capture. Saponite is a greenish/brownish mineral of the smectite family. The hydroxyl feature at 2.7 μm has been observed on numerous primordial asteroids (Takir and Emery, 2012; Rivkin et al., 2022) and recently detected on (162173) Bennu (Hamilton et al., 2019) and (101955) Ryugu (Kitazato et al., 2019) by OSIRIS-REx and Hayabusa 2 observations as well as on their samples (Pilorget et al., 2021; Nakamura et al., 2023; Hamilton et al., 2024). Phyllosilicates are expected to be detected in the case of the captured asteroid hypothesis. However, they may also be detected in the giant impact scenario with a low heating formation process and high water content (Ronnet et al., 2016; Pignatale et al., 2018). It is worth noticing that no unambiguous indication for this usually deep band was detected by varied observations of Phobos. Ground-based observations are hampered, in the 2.7 μm region, by the atmosphere but can still be consistent with the presence of a hydroxyl feature (Rivkin et al., 2002; Takir et al., 2022). Based on CRISM observations, Fraeman et al. (2014) found the possible presence of asymmetric band edges at 2.7 μm although the CRISM data between 2.70 and 2.76 μm is not usable.

In the second objective of our work, we search to improve the spectral match of Phobos to our simulants (Wargnier et al., 2023a,b) in the mid-infrared range. We create a new Phobos simulant adding phyllosilicates into the initial mixture (olivine, anthracite, DECS-19 coal, see Wargnier et al. 2023b) as suggested by Giuranna et al. (2011). We prepared varied samples of powdered materials to reproduce characteristic features of the Phobos spectrum from the VNIR to the MIR.

We noticed however that other works propose materials and mixtures as simulants to Phobos composition (Pajola et al., 2013; Rickman et al., 2016; Landsman et al., 2021; Miyamoto et al., 2021). Two of the most used in the community are the Tagish Lake meteorite and the University of Tokyo Phobos Simulant (UTPS, Miyamoto et al. 2021). Therefore, we compare results on our simulants with the results obtained on the Tagish-based UTPS (UTPS-TB) simulant.

We also investigate the effect of the geometry of observation which is an important parameter as it affects the slope and reflectance. Specifically, the phase curve, which represents the evolution of reflectance with phase angle, is critical to understand the texture of the surface in addition to spectroscopic observations, more sensitive to the composition.

Finally, we remind the readers that this paper is the first in a series on the spectro-photometry of Phobos simulants. We plan studying the spectro-photometric modifications of different Phobos simulants adding the effect of several properties of a surface and processes that can alter the surface of a material (e.g., space weathering, increase of porosity/roughness, ...). Therefore, we will be able to compare the results with the observations of Phobos taken at different phase angles from ground-based and remote-sensing observations with laboratory data, and help to constrain the Phobos surface properties from the future MIRS observations.

2. Materials and methods

2.1. Preparation of samples, mixtures, and simulants

This work presents the results of three main investigations: (1) the evaluation of the 2.7 μm and 3.4 μm features in Phobos-like material, (2) the update of our previous spectroscopic simulant (Wargnier et al., 2023b), and (3) the computation of photometric properties of Phobos simulants. To achieve these results, we used various materials including silicates, phyllosilicates, organics, and opaque materials. The endmembers were selected based on their representativeness in the context of the Phobos surface, as well as their spectral properties that match well with the Phobos spectra in the visible, near-infrared, and/or mid-infrared. Some of these endmembers were previously presented in other works (Wargnier et al., 2023a,b). We have previously discussed the presence of olivine and opaque materials. The olivine used in this work was purchased from Donghai Crystal products and is a green forsterite with half-centimeter-sized crystals. It has a very similar Mg/Fe ratio (Section 2.2) and spectral properties (Section 3.2) compared to the previous olivine. We used anthracite as a darkening agent to reproduce the flat, dark, and featureless VNIR Phobos spectrum. Despite its interesting optical properties, anthracite is not a plausible analog material for the surface of a small body, as its formation requires a high pressure and high temperature (~200 °C) over a period of more than 0.1 Myr (Quirico et al., 2016). This is a very mature coal with about 92% of carbon content. In literature, several opaque materials were found (i.e., FeS and Fe_3O_4) to be common minerals in carbonaceous chondrites. Despite the good mineralogical representativeness of FeS, we found that this material reproduces poorly the red spectral slope of Phobos in the near-infrared (Wargnier et al., 2023a). The use of anthracite in this study is solely for the purposes of simulating opaque materials and not as a representative organic material for the Phobos surface. Furthermore, the utilization of anthracite as opaque material was primarily driven by its ease of use in the context of a simulant, in comparison with FeS, which tends to rapidly oxidize. Elementary composition, grain size, density, and origins are presented for each endmembers in Table A.1.

To investigate the presence and detectability of phyllosilicates on Phobos, we used antigorite (provided by the Museum National d'Histoire Naturelle (MNHN), Haute-Garonne, France), biotite (#53220.12100.136, Canada, purchased from Kremer Pigmente), saponite (SapCa-2, California, USA, purchased from the Clay Mineral Society), and nepheline (provided by MNHN, Brevig, Norway). Antigorite was about 1-cm size grain and 1.1 g. Nepheline was three small pieces of about 1 gram in total and biotite was fined grain powder (0–250 μm in size).

The presence of organics was already discussed for Phobos in the Introduction (Section 1), and it is only expected in the case of the captured asteroid hypothesis. In this scenario, a coal from the Penn State Coal Sample Bank (DECS-19) is particularly useful for its strong red slope in the visible (Wargnier et al., 2023b). DECS-19 is a low-volatile bituminous coal provided by the Coal Sample Data Bank from Penn State University. This mature coal has a mean-maximum vitrinite reflectance of 1.71%, H/C = 0.65, O/C = 0.027 and N/C = 0.01. Ashes account for ~4.6%, and total sulfur form for 0.74%. Coals have been used as optical analogs of extraterrestrial insoluble organic matter (IOM, Moroz et al. 1998), though their structure and composition display substantial differences (Quirico et al., 2009, 2016; Alexander et al., 2017). DECS-19 is a quite mature coal, which better fits with organic matter hosted by a thermally metamorphosed chondrite, and possibly with organics in micro-meteorites that were heated through collision with Phobos, thereby generating its regolithic surface. Titan tholins were used to reproduce the simulant proposed in Wargnier et al. (2023a). The preparation of the different materials was similar to Wargnier et al. (2023a): endmembers were ground using a cryogenic grinder Retsch Cryomill at Laboratoire Génie des Procédés et Matériaux (LGPM). A single steel ball with a diameter of one centimeter was used for dry grinding. Endmembers were then successively dry-sieved in different grain size ranges: 0–25 μm, 25–50 μm, 50–100 μm, and 100–450 μm. Because we expect for Phobos grains a size of about 80 μm (Kuehrt et al., 1992; Giuranna et al., 2011; Miyamoto et al., 2021) we chose, in particular, to extract grains between 25–50 μm and grains between 50–100 μm. Biotite was purchased pre-grounded and then sieved using the same protocol. Hyperfine dark materials were already prepared as submicrometric particles. The protocol to obtain the hyperfine dark powders is described in Sultana et al. (2021, 2023). The submicrometric particles increase the darkening power of these materials. Although extraterrestrial materials do not necessarily exhibit such a distribution of opaque material sizes, the Ryugu samples demonstrate the presence of very fine opaque grains in relatively large quantities (e.g., Nakato et al. 2023). The endmembers were then mixed together using an agate mortar to obtain an intimate mixture. Mixtures were made in volume percentages (Wargnier et al., 2023b). Density values for some endmembers have been obtained directly for our samples. This is the case for olivine and anthracite (Sultana, 2021). Other mean density values were obtained from the literature (see Table A.1). Prepared mixtures for this work are described in Table 1. Images of endmembers and simulants are shown in Fig. 1.

We also use two different Phobos simulants: (1) the University of Tokyo Phobos simulant (UTPS, Miyamoto et al. 2021) based on Tagish Lake mineralogical and spectral properties. A 500-g UTPS piece was ground and sequentially sieved to different grain size (0–25 μm, 25–50 μm, 50–100 μm and 100–450 μm) (2) Phobos Simulant for Detectability (PSD, Wargnier et al. 2023a) based on Phobos spectral properties in the VNIR, including slope and reflectance. The simulant is prepared with 50–100 μm olivine, submicron anthracite, and Titan tholins (~400 nm). Additionally, the simulant has the advantage of showing no absorption in the relevant wavelength range, making it an excellent choice for detectability studies on a Phobos-like surface.

2.2. Samples characterization

Elemental investigation of endmembers was obtained using energy-dispersive X-ray spectroscopy (EDX) and for the biotite sample, Laser-Induced Breakdown Spectroscopy (LIBS). EDX analysis was performed using an EDAX Metek New XL30 coupled to a FEI Quanta200 environmental SEM at LGPM with an accelerating voltage of 15 kV. LIBS emission spectrum of biotite was obtained using the TX1000 instrument

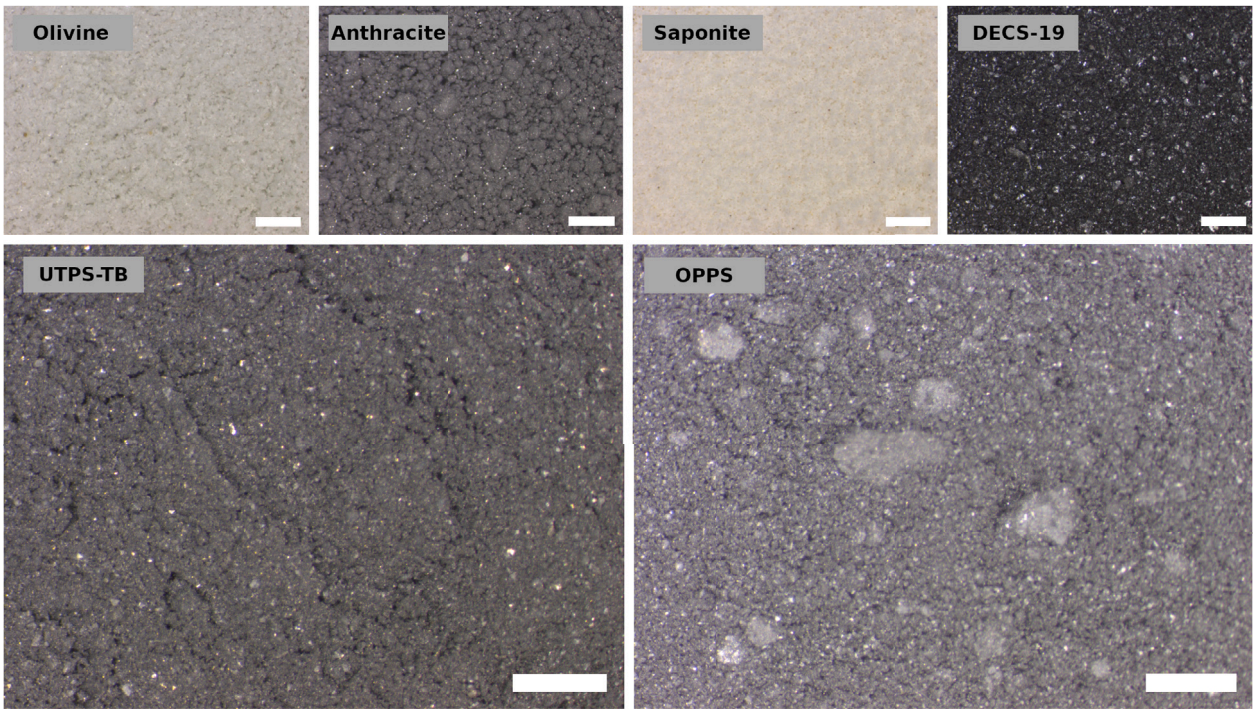

Fig. 1. Mosaic of optical images of the surfaces of the two Phobos simulants (UTPS and OPPS) that were investigated, as well as the endmembers of the OPPS. The bright spots visible in OPPS correspond to those in DECS-19. DECS-19 grains tend to have large facets and diffuse light in specular reflection, resulting in bright spots. Each scale bar represents 1 mm. Grains morphology and size were investigated using SEM images (see Fig. A.1).

from Iumtek. We performed SEM images in low vacuum mode with magnification between 250 and 4000.

For grain size measurements, we used both SEM images – which allow also to analyze the state of the mixture – and a laser diffraction analyzer. The particle size analyzer is a Malvern Mastersizer 3000 with the Hydro MV accessory. We dispersed the samples in ultrapure water (15 MOhm cm) using both stirrer and sonicator to disrupt the aggregates that may form. We acquired data for 30 s with two laser at different wavelength to cover different grain size ranges and repeat at least 6 times the measurements. Averaging the measurements, we can obtain a particle size distribution of our samples in a wide range, from nanometers to millimeters.

2.3. Detectability of organics and hydrated minerals: estimation of hydroxyl and hydrocarbon groups content

The MIRS spectrometer onboard MMX will observe for the first time the 3.4 μm region of the Phobos spectrum with sufficient SNR. Using ground-based observations, Takir et al. (2022) have shown the absence of C–H stretching mode absorption bands in the upper limit of 15–20%: if the bands are weaker than these values, they are not detectable from these observations due to measurement uncertainties. However, organics on Phobos could be altered by space weathering and hence, less detectable. It also important to note that other small bodies have shown features in this wavelength range related to organic materials, such as Bennu (Kaplan et al., 2021), Ryugu (Yada et al., 2021; Pilorget et al., 2021; Hatakeda et al., 2023), 67P (Raponi et al., 2020), Ceres (De Sanctis et al., 2017, 2019) and in insoluble organic matter (IOM) of meteorites (Orthous-Daunay et al., 2013; Kaplan et al., 2019). Presence of organics in primitive asteroids are particularly discussed in Hromakina et al. (2022). They found no 3.4 μm signature in the spectrum of the D-type Bononia (Takir and Emery, 2012), despite the good signal-to-noise ratio, but Jupiter trojans asteroids have shown signatures of organics (Brown, 2016; Wong et al., 2023). In this context, it appears important to study beforehand the detection of this type of organic feature to interpret future MIRS observations. We added organic compound (DECS-19) in different proportions from 5 to 30 volume percent in PSD. Based on the vitrinite reflectance (1.71%) of DECS19 and the relationship with aliphatic groups obtained through linear regression of the data from Wei and Tang (2018), we were able to derive the contribution of aliphatic and aromatic carbon (Fig. 2). Our analysis revealed that 16% of carbon is involved in aliphatic structures and 84% in aromatic structures. This is consistent with the results of the RMN measurements on DECS-19 presented in Vinogradoff et al. (2021). Therefore, it is possible to estimate the minimum quantities of aliphatic and aromatic carbon structures required for detection by IR spectroscopy (Table 2). For instance, the addition of 10 vol.% of DECS-19 to the PSD mixture results in the incorporation of 5.37 wt% of carbon, with 4.51 wt% corresponding to aromatic carbon structures and 0.87 wt% to aliphatic structures.

Because hydrated minerals can be expected for Phobos but were never unambiguously detected, our aim is also to investigate the detectability of hydrated minerals in a Phobos simulant, in preparation for future MIRS observations. We decided to use the antigorite as the phyllosilicates part for the study of detectability of the 2.7 μm feature characteristic of hydrated minerals. As for organics, using the Phobos simulant PSD from Wargnier et al. (2023a), we added the phyllosilicate in various quantities from 1 to 20 vol.% (Fig. 7(a)). The composition and density of the material were also considered in order to express the phyllosilicate quantities in terms of OH groups, which is an important parameter for the detectability of the 2.7 μm band. For example, 10 vol.% of antigorite in the mixture corresponds to 2.46 wt% of hydroxyl groups (Table 3). This approach allows for the straightforward extension of this work to other phyllosilicates with varying OH compositions.

2.4. Reflectance measurements

In this study, we performed bidirectional reflectance spectra from visible to mid-infrared using different instruments. Reflectance spectra in the VNIR (0.6–4.2 μm) were made at room temperatures using the Spectro-photometer with cHanging Angles for Detection Of Weak

Table 1
Composition of the prepared mixtures in olivine, anthracite, DECS-19, and phyllosilicates. Quantities are given in vol.%. PSD (Wargnier et al., 2023a) is composed of olivine (77 vol.%, 100 μm), anthracite (20 vol.%, <1 μm), and Titan tholins (3 vol.%, 400 nm). PSD is only used for the detectability study as it exhibits no absorption associated to a reflectance and spectral slope similar to Phobos spectra. Mixing ratios for the simulant mixtures were determined after several attempts based on their spectroscopic properties (Wargnier et al., 2023a,b). Name of the simulant mixtures were determined by the phyllosilicate composition: ATG for a simulant containing antigorite, BIO for biotite, NEP for nepheline, and SAP for saponite. Each of these mixtures contains also olivine, anthracite, and DECS-19 (Wargnier et al., 2023b).

	Grain sizes Mixtures	PSD	Olivine 50–100 μm	Anthracite <1 μm	DECS-19 50–100 μm	Antigorite 50–100 μm	Biotite 50–100 μm	Nepheline 50–100 μm	Saponite 50–100 μm
Detectability tests	CH-rich-5	95	–	–	5	–	–	–	–
	CH-rich-10	90	–	–	10	–	–	–	–
	CH-rich-15	85	–	–	15	–	–	–	–
	CH-rich-20	80	–	–	20	–	–	–	–
	CH-rich-30	70	–	–	30	–	–	–	–
	Hydmin-rich-1	99	–	–	–	1	–	–	–
	Hydmin-rich-3	97	–	–	–	3	–	–	–
	Hydmin-rich-5	95	–	–	–	5	–	–	–
	Hydmin-rich-10	90	–	–	–	10	–	–	–
	Hydmin-rich-15	85	–	–	–	15	–	–	–
	Hydmin-rich-20	80	–	–	–	20	–	–	–
Simulant mix.	SIM-ATG-BIO-1	–	30	20	–	25	25	–	–
	SIM-ATG-BIO-2	–	25	15	10	25	25	–	–
	SIM-ATG-BIO-3	–	20	20	20	20	20	–	–
	SIM-ATG-BIO-4	–	15	25	10	25	25	–	–
	SIM-NEP-1	–	25	15	10	–	–	50	–
	SIM-NEP-2	–	20	20	20	–	–	40	–
	SIM-NEP-3	–	15	25	20	–	–	40	–
	SIM-ATG-SAP-1	–	25	15	10	25	–	–	25
	SIM-ATG-SAP-2	–	20	20	20	20	–	–	20
	SIM-SAP-1 (OPPS)	–	20	20	20	–	–	–	40

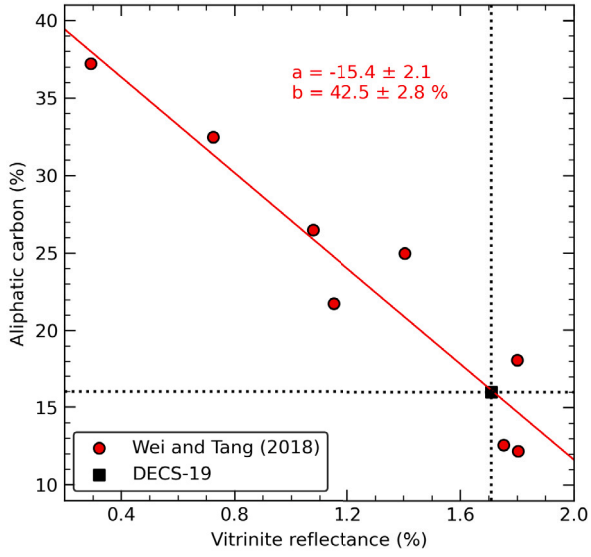

Fig. 2. Aliphatic carbon percentage as a function of vitrinite reflectance percentage. From the linear fit of the data (red points) from Wei and Tang (2018), the aliphatic carbon percentage of DECS-19 is derived knowing the vitrinite reflectance.

Table 2
Estimation of hydrocarbon CH_x groups in each mixtures for organics detectability study.

Mixtures	DECS-19 (vol.%)	DECS-19 (wt.%)	Carbon (wt.%)	Aliphatic (wt.%)	Aromatic (wt.%)
CH-rich-5	5	3.08	2.64	0.42	2.21
CH-rich-10	10	6.28	5.37	0.87	4.51
CH-rich-15	15	9.62	8.23	1.33	6.91
CH-rich-20	20	13.11	11.22	1.81	9.41
CH-rich-25	30	20.55	17.59	2.83	14.75

Signals (SHADOWS, Potin et al. 2018) at Institut de Planétologie et d'Astrophysique de Grenoble (IPAG, France). We acquired also spectra

Table 3
Estimation of hydroxyl OH groups in each mixtures for hydrated minerals detectability study.

Mixtures	Antigorite (vol.%)	Antigorite (wt.%)	OH (wt.%)
Hydmin-rich-1	1	0.9	0.24
Hydmin-rich-3	3	2.7	0.73
Hydmin-rich-5	5	4.5	1.22
Hydmin-rich-10	10	9.1	2.46
Hydmin-rich-15	15	13.7	3.70
Hydmin-rich-20	20	18.3	4.94

in the VNIR with the SpectropHotometer with variable INcidence and Emergence (SHINE, Brissaud et al. 2004), also hosted at IPAG. SHINE is a VNIR spectrophoto-goniometer that measures reflectance spectra from 0.6 to 4.2 μm. SHINE was used in the Gognito mode (Potin et al., 2018) which allow us to reduce the size of the illumination, and hence to observe smaller and darker samples. These spectrogonio-radiometers measure in both visible and near-infrared using two different detectors: a silicon detector for the visible part and an InSb detector cooled at 77 K for the NIR. The spectral resolution of SHADOWS and SHINE is wavelength-dependent, spectral sampling is 20 nm. Spectral resolution of the spectrogognio-radiometers is comparable to the expected MIRS spectral resolution (Barucci et al., 2021). For each wavelength, the intensity is obtained with a 300 ms integration time. This measurement is repeated 20 times. The calibrated reflectance is then given by the mean value of these 20 measurements for a wavelength and the error on the measurement is given by the standard deviation. Instrumental and atmospheric effects were suppressed by taking reference measurements using a Spectralon© reference in the visible and an Infragold© reference in the near-infrared. In this paper, unless otherwise stated, we used the nominal SHADOWS and SHINE geometrical configuration (incidence i = 0°, emission e = 30°, and azimuth ϕ = 0°). Measurements at different phase angles have been also performed from 5° to 130°. Due to instrument limitations, spectra at phase angle smaller than 5° cannot be obtained.

Near- and mid-infrared spectra were obtained with a Fourier-Transform Infrared Spectrometer (FTIR) Bruker VERTEX 70 V (1.25–20 μm) at IPAG. The instrument is mounted with a Bruker accessory (A513/QA) for bidirectional measurements. The MCT detector is cooled

with liquid nitrogen (LN-MCT) and the sample chamber is purged with dry air. For each measurement, we performed 100 scans with a spectral resolution of 4 cm^{-1}. Reference was taken with direct flux with i = 90° and e = 90°. Using this method for reference, the spectrum is not in absolute unit. Therefore, a calibration procedure has been defined for FTIR spectra using a multiplicative factor to overlap the spectrum measured with SHADOWS. To take into account the possible variation of the sample surface, we measured the reflectance spectrum for each sample three times, re-preparing each time the sample.

2.5. Spectral and photometric analysis

2.5.1. Reflectance, slope, and band depth

In the VNIR, three main parameters were studied: the spectral slope, the reflectance and the band depth. Spectral slopes were obtained between 720 and 900 nm, 1.5 μm and 2.4 μm, and 3.7 and 4.0 μm using the formula given in Wargnier et al. (2023a). The spectra were normalized and the slope then computed at the starting wavelength of each interval, namely 720 nm, 1.5 μm, and 3.7 μm.

Reflectance level was directly obtained by the SHADOWS measurements, with an absolute precision of about 1% (Potin et al., 2018) and measured at 600 nm, 1.8 μm, and 4.0 μm, averaging 10 measurements at each wavelength. Bands depth were computed using the following procedure: the absorption bands at 3.28 and 3.42 μm were characterized using a linear fit for the continuum as shown in Fig. 3. Anchor points for the linear continuum were fixed at various wavelengths in the vicinity of the edge of the features, as slight variations were observed with modifications of the anchor points' positions. This allows obtaining an uncertainty on the definition of the continuum. We take also into account the uncertainties of the SHADOWS measurements (Fig. 3). We chose to not include the 3.0 μm absorption band in the linear continuum because we focused our work on the 3.4 μm and because this feature is mainly due to water absorption in our sample. However, due to the presence of the 3.0 μm feature, the 3.42 μm absorption band will be probably a bit overestimated compared to the 3.28 μm absorption feature. The band depth was computed using the formula from Clark and Roush (1984). X-axis error bars have been obtained with the uncertainty of the balance. Y-axis error bars have been computed using the propagation of uncertainties and by taking into account the two sources of uncertainties described above. The hydrated mineral band depth was computed using a similar method, with anchor points for the linear continuum defined at 2.4 and 4.0 μm.

For MIR spectra, we measured reflectance spectra and converted spectra in emissivity using an approximation of the Kirchhoff's law: $E = 1 - R$, where R is the reflectance and E the emissivity (Salisbury et al., 1991, 1994). Although it is an approximation of an emissivity spectrum, it is useful for qualitative study and comparison with in situ MIR spectra of Phobos (Sultana et al., 2023). Position and shapes of bands are not significantly modified (Salisbury et al., 1991; Martin et al., 2024). In particular, we focused on phyllosilicates bands, Reststrahlen bands (RB), Transparency features (TF), and Christiansen features (CF). These three last features are particularly important for compositional identification. CF generally corresponds to a maximum of emissivity and is caused by an important change in the refractive index of the material (e.g., Salisbury et al. 1991, Martin et al. 2022). RBs are due to fundamental molecular vibration bands (Salisbury et al., 1991) whereas TF depends on the low absorption coefficients in some wavelength region due to the presence of grain with size smaller than 75 μm (Salisbury and Walter, 1989; Salisbury et al., 1991; Hamilton, 2000; Morlok et al., 2019; Martin et al., 2022). Hence, TF depends on the composition of the materials (Salisbury et al., 1991). TF can be generally observed around 10–12 μm (e.g., Mustard and Hays 1997, Mustard and Glotch 2019, Pisello et al. 2022, Poggiali et al. 2023, Morlok et al. 2023).

In this work, we compared experimental spectra with the TES red unit spectrum of Phobos (Glotch et al., 2018). Main features observed in this spectrum are: a double CF at 8.49 μm and 9.17 μm, a RB at 9.8 μm, and a TF at 12.4 μm.

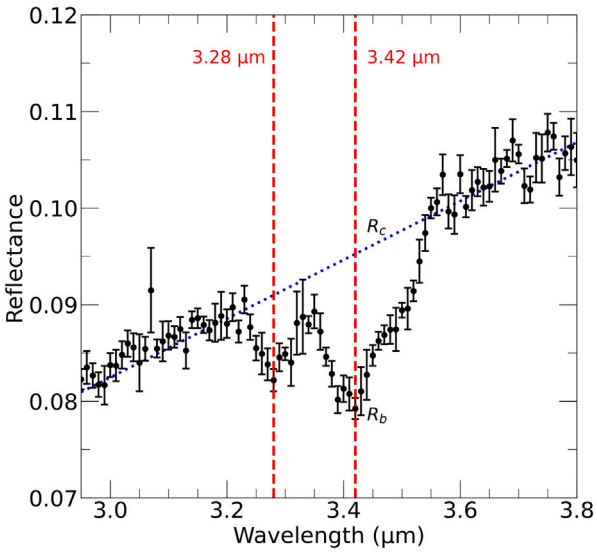

Fig. 3. SHADOWS spectrum with the associated uncertainties of the 3.4 μm region of the mixture CH-rich-30. Uncertainties were measured by SHADOWS with the standard deviation of ten points for a given wavelength. Red dashed vertical lines represent the 3.28 μm and 3.42 μm wavelength. Blue dotted line is the continuum. Reflectance of the continuum at 3.42 μm is noted R_c and R_b is defined as the reflectance in the band. By obtaining these parameters we can determine the band depth. (For interpretation of the references to color in this figure legend, the reader is referred to the web version of this article.)

2.5.2. Hapke modeling

To compare our results with other Phobos observations or with other bodies and laboratory experiments, it is particularly interesting to apply the Hapke model as explained below.

The model.

For this work, we used the Hapke IMSA model (Hapke, 2012) for bidirectional reflectance with a two term single-scattering phase function:

$$r(i,e,\alpha) = \frac{K\omega}{4}\frac{\mu_i}{\mu_i+\mu_e}S(i,e,\alpha,\bar{\theta}) \times \left[P_{hg}(\alpha,b,c)\cdot B_{sh}(\alpha,B_{sh,0},h_{sh}) + B_{cb}(\alpha,B_{cb,0},h_{cb})\cdot M\left(\frac{\mu_i}{K},\frac{\mu_e}{K},\omega\right)\right] \quad (1)$$

The model has an important number of parameters and functions: α is the phase angle, ω is the single scattering albedo, μ_i and μ_e are respectively equal to cos(i) and cos(e) – where i is the incidence angle and e the emission angle.

The B_{sh} and B_{cb} function describes the opposition effect. Each of these functions take into account for different physical effect that occurs at small phase angle: the coherent backscattering effect (CBOE) and the shadow-hiding opposition effect (SHOE). The reader is referred to Hapke (2002) for more details on these effects. The CBOE occurs for very small phase angle (<1°, Helfenstein et al. 1997, Hapke et al. 1998) and considering the lack of data at these phases due to instrument limitations, the contribution of this function can be ignored. The SHOE function is defined as:

$$B_{sh}(\alpha,B_{sh,0},h_{sh}) = \frac{B_{sh,0}}{1+\frac{\tan\alpha/2}{h_{sh}}} \quad (2)$$

where h_{sh} is the half-width of the SHOE. In principle, $B_{sh,0}$ is expected to be between 0 and 1 (Hapke, 1986). However, new models have shown that values of the opposition effect intensity up to 3 can be observed for the rough and irregular surfaces observed on small bodies (Li et al., 2015).

The K parameter has been added in Hapke (2008) and correspond to the porosity factor. We will use here the approximation of the porosity factor given in Helfenstein and Shepard (2011):

$$K \approx 1.069 + 2.109h_{sh} + 0.577h_{sh}^2 - 0.062h_{sh}^3 \quad (3)$$

P_{hg} is the double-term Henyey–Greenstein (2T-HG) function (McGuire and Hapke, 1995):

$$P_{hg}(\alpha, b, c) = \frac{1+c}{2}\frac{1-b^2}{(1+2b\cos\alpha+b^2)^{3/2}} + \frac{1-c}{2}\frac{1-b^2}{(1-2b\cos\alpha+b^2)^{3/2}}, \quad (4)$$

where b and c are related to the scattering behavior of a particle: b is linked to the phase function shape and c to the type of scattering. A negative c value indicates forward scattering whereas a positive c corresponds to backscattering. It is important to note that there are multiple definitions of 2T-HG in the literature, which can result in slightly different bounds for the c parameter. M is the Hapke's multiple scattering function (Hapke, 2002) and the macroscopic roughness function S is presented in details in Hapke (1993). One of the parameters of this function is the surface roughness $\bar{\theta}$ (Hapke, 1984). This parameter dominates for large phase angle data (Helfenstein and Veverka, 1989). Sometimes an another parameter called filling factor is described in the Hapke model. This parameter is related to the porosity of the medium. For consistency throughout this study, the filling factor used in some other studies was converted to the h_{sh} parameter using the relation given in Helfenstein and Shepard (2011).

We searched for the Hapke parameters: ω, b, c, B_0, h, and $\bar{\theta}$. These six free parameters give physical information of the surface (Hapke, 1981, 2002). We searched the parameters inside the following boundaries: w = [0,1], b = [0,1], c = [−1,1], B_0 = [0,3], h = [0,0.15], θ = [11,50]. The boundaries were chosen to explore parameters within the typical range of laboratory experiments (Beck et al., 2012; Pommerol et al., 2013) and to include photometric parameters determined for Phobos (Fornasier et al., 2024). The model is applied on phase curve obtained using reflectance spectra at different geometries of observation. We followed the recommendation from Schmidt and Fernando (2015) and applied the Hapke modeling on the entire dataset at the same time, including measurements at different incidence angle.

Inversion methods.

The Hapke model inversion was performed using various methods because the Hapke equation is non-linear equation with highly correlated parameters. Therefore, the equation generally shows several local minima which makes it difficult to converge to the global minimum. For all these methods, we tried to minimized the reduced χ^2:

$$\chi^2 = \sum_{i=1}^{n} \frac{\left(r_{i,exp} - r_{i,Hapke}(i,e,\alpha)\right)^2}{\sigma_i} \quad (5)$$

Initially, we attempted to use a Levenberg–Marquardt (LM) algorithm, which is based on the gradient and Gauss–Newton algorithms (Levenberg, 2018; Marquardt, 1963; Newville et al., 2015). However, the LM algorithm is more stable than the Gauss–Newton alone. Nonetheless, a good estimate of the initial Hapke parameters is still required. The LM routine was then run with various and random initial parameters (not too far from the estimate). This method enables us to determine whether we converge to local minima instead of the global minimum.

We also tried to fit our experimental using a basin-hopping algorithm (Wales and Doye, 1997). Basin-hopping is a global optimization algorithm that performs several cycles of local optimization combined to random perturbation/step around the solution. At each step, a Metropolis test is performed. We chose to use a Broyden–Fletcher–Goldfarb–Shanno (BFGS) algorithm (Fletcher, 2000) as local optimizer. BFGS is a quasi-Newton method mainly based on approximation of the Hessian matrix to solve nonlinear optimization problem.

We finally tested a Bayesian method to fit the Hapke model using Markov Chain Monte Carlo (MCMC) methods based on the *emcee* MCMC python implementation (Foreman-Mackey et al., 2013). This method takes longer to run, but one of its advantages is that it provides a a-posteriori probability density function (PDF) of the values of the different parameters. This is particularly useful because nonlinear problem (such as Hapke's equation inversion) with several parameters does not have a unique solution and bayesian inference allows to explore the parameter space. For the six Hapke parameters, we considered a prior uniform PDF. We performed the MCMC for 50 000 steps and considering a burn-in period of 5000 steps. The best parameters were chosen from the median of the posterior probability distribution. We also computed the Maximum Likelihood Estimation (MLE) in order to obtain more information about the results. With this setup for the MCMC inversion, we obtained a typical mean acceptance fraction of 0.283.

To give an indication about the difference between the data and the fit, the results of the different methods will be presented associated with the residuals and/or with the root mean square residual (RMS). Considering the methods explored in this work, it appears that MCMC is a very good approach to inverse the non-linear Hapke equation with a relatively high number of free parameters. However, the bayesian inference is a very time-consuming computation method and while the number of point in our dataset is quite small, it can be more complicated to use this Monte Carlo strategy for large dataset.

Parameters uncertainties.

Determining uncertainties in the inversion of the Hapke model can be challenging. They are often under- or over-estimated because all the parameters are correlated. Depending on the methods, we estimated the uncertainties with various manners: (1) For the LM algorithm we took the uncertainties as the diagonal terms of the covariance matrix. However, the uncertainties appears so large that we decided to computed the uncertainties based on the variability of the fit when varying the initial estimations of the parameters and parameters space. This method appears unfortunately also prone to large errors. (2) For the basin-hopping method, we obtained the uncertainties with the inverse of the Hessian matrix, and (3) For the MCMC inversion, we assumed that the uncertainties are given by the 16-50-84 percentiles.

Several others studies were trying to have a good estimate of the uncertainties when fitting the Hapke model (e.g., Gunderson et al. 2006, Shepard and Helfenstein 2007, Schmidt and Fernando 2015). Shepard and Helfenstein (2007) estimated the uncertainties by taking into account the variation of the obtained parameters values when fitting variants description of the Hapke model. Schmidt and Fernando (2015) used synthetic datasets and inversion using MCMC to explore the parameters space and obtained realistic uncertainties for Hapke modeling of photometric measurements. They found that uncertainties on the Hapke parameters can be less than 10% in very favorable conditions such as with a full BRDF from almost 0 to 180 degrees of phase angle, and/or with small uncertainties on the data (<5%), etc. Therefore, there is not a unique method to obtain uncertainties and the coverage of the dataset in terms of illumination angles can drastically change the values of the parameters and especially of the associated uncertainties.

3. Results

3.1. Physical properties and elemental composition of endmembers

EDX analysis reveals an Mg-rich composition for the olivine (Mg# defined as the atomic ratio Mg/(Mg+Fe) = 0.90). We performed also EDX on the various phyllosilicate samples. For example, antigorite appears to be mostly dominated by magnesium. It is also composed of silicon and iron. EDX analysis of the different materials including phyllosilicates is presented in Table A.3. LIBS spectrum has shown that biotite is mostly composed of aluminum, magnesium, iron, silicon, potassium, and calcium. We observed also a minority of lithium, sodium, and titanium; and traces of rubidium, strontium, beryllium,

barium, chromium, zinc, and tin. For the three last elements, the content is about 20 ppm. Light elements such as oxygen, nitrogen, and hydrogen cannot be investigated with the LIBS instrument. Chromium, zinc, and tin are not expected to be found in biotite but could be due to the grinding process. Lithium, sodium, and titanium are classically found as traces in biotite samples (Ellis et al., 2022; Redin et al., 2023). The LIBS instrument is here particularly sensitive to these two first elements. Whereas calcium is found as a major element in the biotite, it is not expected. However, it has already been observed in biotite samples and was explained by contamination of the natural biotite by calcic rocks (Lovering, 1972). LIBS spectrum of biotite in McMillan et al. (2007) shows also important calcium emission bands.

DECS-19 was already fully characterized and additional information can be found on the Penn State Coal Sample Bank website. Saponite SapCa-2 was characterized by the Clay Mineral Society and information can be found on their website. We also reported elemental composition of phyllosilicates given by the EDX measurements in Appendix A (Table A.3).

For UTPS and olivine grain size, we obtained a distribution (Fig. A.2 in Appendix A) peaked at 50–100 μm, as expected because the samples were sieved at this grain size range. Although most of the distribution is in this range, we also noticed a tail toward small grains. This is because small grains tend to clump together with larger grains, forming relatively large aggregates that do not pass through the sieve, but are disrupt by the sample preparation for the particle size analyzer. For the anthracite, the laser granulometry was probably less efficient because the SEM images showed that most of the grains are hyperfine (<1 μm), but the laser method shows a complicated behavior of the distribution with several modes. In particular, even with the precaution of disrupting the aggregate, we noticed that some grains re-aggregate after some time. Laser diffraction granulometry is then a useful complementary method to SEM and the combination of the two techniques allows the full characterization of the grain size of the samples.

3.2. Spectral properties of the endmembers

3.2.1. In the VNIR

The olivine spectrum (Fig. 4(a)) exhibits a typical 1 μm absorption band due to iron ions transition (Cloutis et al., 2012a; Sultana et al., 2021). An important feature at 3.0 μm is also visible on the spectrum and is attributed to the adsorption of atmospheric water in olivine powder. The attribution was confirmed by the total removal of the band when measuring under vacuum (see Fig. C.1). The reflectance of olivine is quite high (70%). Anthracite is featureless and red-sloped from 0.6 to 4.2 μm with a reflectance of 2% at 0.6 μm and 4% at 4.2 μm. Titan tholins are relatively bright, in particular between 1 and 3 μm, with a reflectance up to roughly 70%, and exhibit a deep feature due to N–H stretching modes at 3 μm which has been particularly discussed and studied in Wargnier et al. (2023a). DECS-19 exhibits C–H stretching modes at 3.28 μm and 3.42 μm (Fig. 4(a)). The absorption band at 3.28 μm is assigned to aromatic groups. The 3.42 μm feature is attributed to C–H stretching modes of methylene (CH_2) aliphatic structures (Moroz et al., 1998; Vinogradoff et al., 2021). From the information provided by the Penn State Coal Sample Bank, DECS-19 has a H/C of 0.6 which corresponds to a composition with 85% of carbon. Such a H/C is notably in agreement with the H/C on asteroid Bennu, which would be between 0.3 and 0.6 (Kaplan et al., 2021). Although coals could be representative of the composition of a small body such as Phobos, Bennu, and Ryugu; they were chosen for their spectral properties and their aromatic/aliphatic features. DECS-19 presents another absorption band near 3 μm which is due to water adsorption in the coal powder (see Fig. C.1 in Appendix A). It is also red-sloped between 0.6 and 4.2 μm, and the reflectance varies from 2.5% at 0.6 μm to 17% at 4.2 μm.

Pertaining to phyllosilicates (Fig. 4(b)), antigorite shows overtone features between 0.6 and 2.5 μm and a reflectance on average of 0.6 in this wavelength range. A deep 2.7 μm O–H feature can be observed, accompanied by a molecular water absorption band at 3.0 μm (Fig. C.1). Biotite, from 0.6 to 2.5 μm, exhibits a red slope and is darker than antigorite with a reflectance of 0.1 at 0.6 μm. Reflectance of biotite becomes higher than antigorite after 2.5 μm and up to 4.2 μm. Biotite shows also a 2.7 μm absorption band and a 3.0 μm feature (Fig. C.1). Nepheline spectrum is flat from 0.6 to 4.2 μm with a reflectance of 0.6 at 0.6 μm. Because nepheline is a feldspathoid, the 2.7 μm feature is not present in the spectrum. But a 3 μm band can be observed, due to molecular water and/or O–H defects due to the natural origin of the nepheline. Saponite is relatively bright especially for $\lambda < 1.3$ μm with a reflectance of 0.8. It presents also deep absorption feature at 1.45 μm (OH), 1.9 μm (OH/H_20), and 2.3 μm (Mg–OH) (Cloutis et al., 2012a). The 2.7 μm band is visible and is associated with a deep and large 3 μm trough. This is because saponite, a clay mineral, absorbs a significant amount of atmospheric water. Despite using a calcium-rich saponite, a faint feature was observed in the 0.65–0.7 μm regions, possibly due to Fe^{2+}–Fe^{3+} charge transfer (Cloutis et al., 2012a,b). The antigorite spectrum also exhibits this feature, with a larger band and a center position around 0.7–0.75, also in this case due to iron charge transfer, as noted by Cloutis et al. (2012a). An additional feature is also visible in the antigorite spectrum at 0.9 μm, probably due to an octahedral Fe^{2+} crystal field transition (Cloutis et al., 2012a).

3.2.2. In the MIR

Mid-infrared spectra of olivine, anthracite, and DECS-19 were already discussed in details in Wargnier et al. (2023b). None of these materials showed spectroscopic features similar to Phobos in the MIR. Olivine shows a CF at ~9 μm, anthracite at ~7.9 μm, and DECS-19 at ~7 μm.

It should be noted that the measurements were taken under standard atmospheric conditions and at room temperature. Although this may affect the VNIR spectrum, the effects on the MIR spectrum are more pronounced and therefore not entirely representative of the conditions on Phobos. This could result in variations, such as differences in feature position or intensity (Salisbury and Walter, 1989; Salisbury et al., 1991; Cooper et al., 2002). However, it is important to note that the approximation of Kirchhoff's law to obtain emission spectra may also potentially modify the band position and intensity. Only few studies have investigated the spectral effect of the approximation of the Kirchhoff's law (e.g., Salisbury et al. 1991, 1994), but they found only slight variations in band positions and spectral contrast, mainly due to variations of the thermal gradients. The Kirchhoff' law is therefore a useful and correct approximation for qualitative studies. In this work, MIR spectra are used to qualitatively compare with the Phobos spectrum; variations may occur under different experimental conditions.

Several phyllosilicates spectra were investigated in the MIR (Fig. 5) and the choice of the best phyllosilicates endmembers for the following measurements, was based on the comparison with TES red unit spectrum of Phobos (Glotch et al., 2018). CF of nepheline is also shifted toward smaller wavelength compared to the TES spectrum, but the overall spectrum better matches the Phobos spectrum. Saponite and antigorite spectra have a CF respectively that match well the first CF of the Phobos spectrum and their RB is close to the position of the band observed in Phobos spectrum. The best match in the MIR for a single endmember is the biotite. Positions of the three important features (CF, RB, and TF) match the position of the same features in the Phobos spectrum. As suggested by Giuranna et al. (2011), a linear mixture of biotite and antigorite in equal quantities was also measured. However, looking only at the positions of CF, RB, and TF, pure biotite is more in agreement with the Phobos observation. Note that determining the mineralogical composition with a double CF can be complicated. This type of complex CF may result from the combination of two distinct endmembers that can be spectrally resolved, and therefore manifest themselves as two distinct peaks (Salisbury et al., 1991).

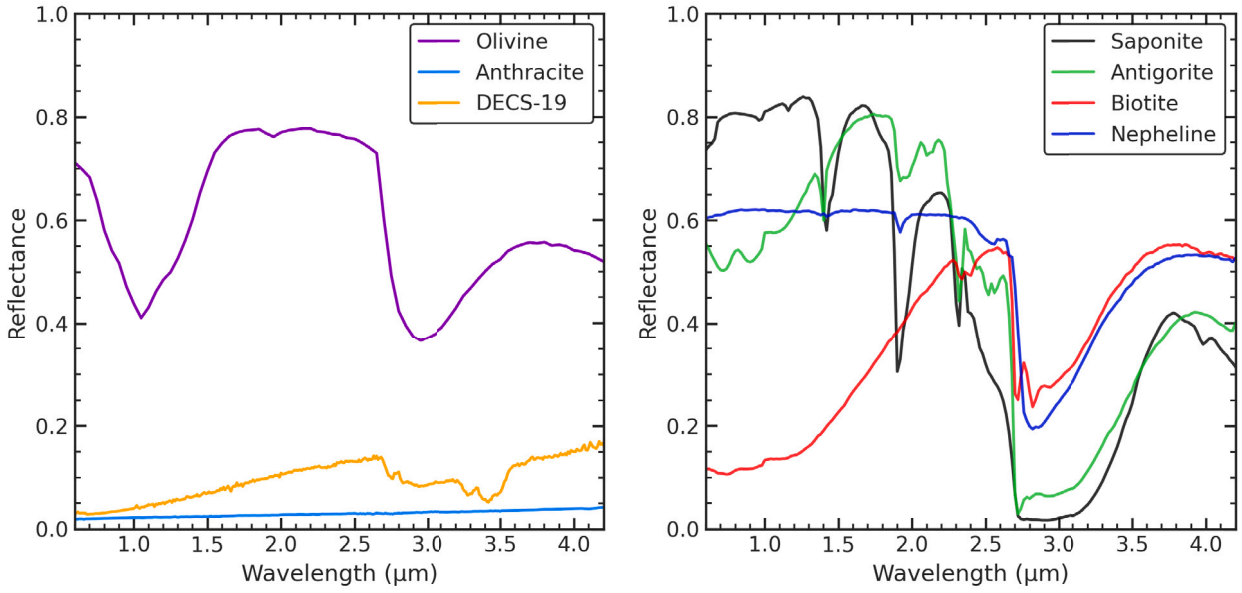

(a) (b)

Fig. 4. (a) Bidirectional reflectance spectra in the visible and near-infrared of the endmembers used in the Phobos simulant proposed in Wargnier et al. (2023b). The 3 μm-band visible in the olivine and DECS-19 spectra is mainly due to adsorbed atmospheric water in the sample powder. Grain size of olivine and DECS-19 is 50–100 μm, and anthracite is <1 μm. (b) Bidirectional reflectance spectra in the visible and near-infrared of some of the phyllosilicates used in this study. Phyllosilicates spectra were made on powders with the same grain size range (50–100 μm) for the different endmembers using the SHADOWS instrument.

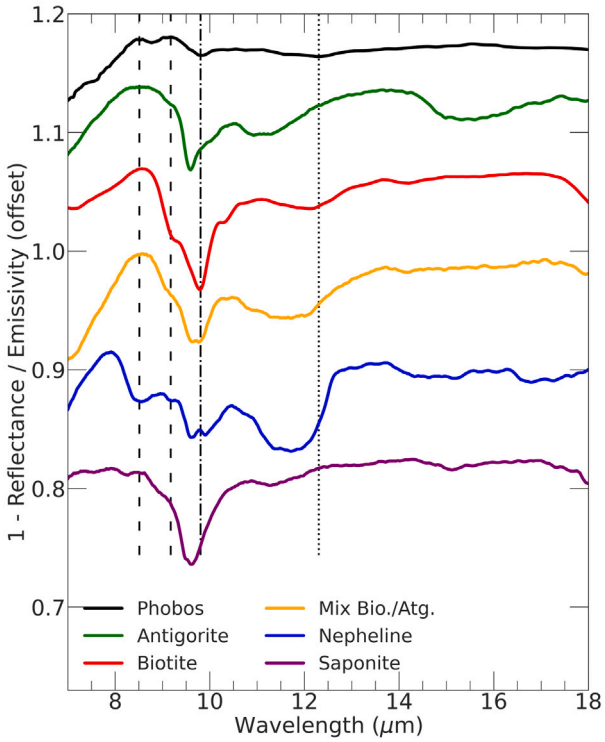

Fig. 5. Bidirectional 1-reflectance spectra in the mid-infrared of phyllosilicates used in this study compared to the TES red unit emissivity spectrum of Phobos (Glotch et al., 2018). The "Mix Bio./Atg." is a 50:50 vol.% mixture of biotite and antigorite. Grain size of the phyllosilicates is 50–100 μm (Table 1). The vertical dashed line indicates the positions of the Christiansen features of the Phobos spectrum. The vertical dash-dotted and dotted line show respectively the positions of the Phobos reststrahlen band and of the transparency feature. Note that the biotite spectrum was re-scaled and divided by a factor of 4, for clarity. Positions of the CF, RB, and TF of the biotite are in relatively good agreement with the Phobos mid-infrared features.

3.3. Detection of aliphatic/aromatic bands in Phobos spectral simulants

The two organic features at 3.28 μm and 3.42 μm are clearly observed (Fig. 6(a)). We study, here, the evolution of the absorption band depth as the proportion of DECS-19 increases, to determine the detectability of 3.4 μm organics. Results of this investigation are shown in Fig. 6(b). The depth of the 3.28 μm and 3.42 μm features increases with the DECS-19 volume percentage quantity. Using a linear fit, we find a slope of 0.34 ± 0.03%/μm with a zero-point of 0.60 ± 0.58% for the 3.28 μm feature. For the 3.42 μm absorption band, we compute a slope of 0.49 ± 0.07%/μm and 2.76 ± 1.37% for the zero-point.

These results can be compared with those presented in Wargnier et al. (2023a), obtained using tholins as an organics source. The 3 μm N–H feature linked to the presence of organics was much bigger than the aliphatic/aromatic bands in this work and the limit of detectability was reached for 5 vol.% of tholins in the simulant. For the same geometry, the N–H band depth is around 25%. But the bands studied in this work, are more representative of what we expect on the Phobos surface in the case of the captured asteroid hypothesis.

Finally, Fig. 6(b) highlights the quite high values of band depth for the 3.42 μm feature for organic-rich composition. The maximum value obtained – for the 3.42 μm absorption band and for 30% of DECS-19 in PSD – is slightly larger than 18%. However, the band depth is strongly dependent on the organic quantity in the simulant.

3.4. Detectability of hydrated minerals

We found, as expected, that bands depth increase with increasing quantity of phyllosilicates (Fig. 7(b)). A linear fit of band depth as a function of phyllosilicates quantity gives a zero-point of 3.13 ± 0.60% and a slope of 0.99 ± 0.05%/μm. Hence, the 2.7 μm antigorite band increases particularly rapidly as the quantity of hydrated minerals increases. The O–H stretching mode feature appears to be narrow and intense. The minimum of the band is always centered at 2.72 μm. The band is generally associated with a 3 μm feature due to water adsorption and/or O–H defect in the natural sample of minerals. As the 2.7 μm feature is narrow, the limited resolution of the instrument can lead to a non-complete band. This effect is visible for the hydmin-rich-5 mixture

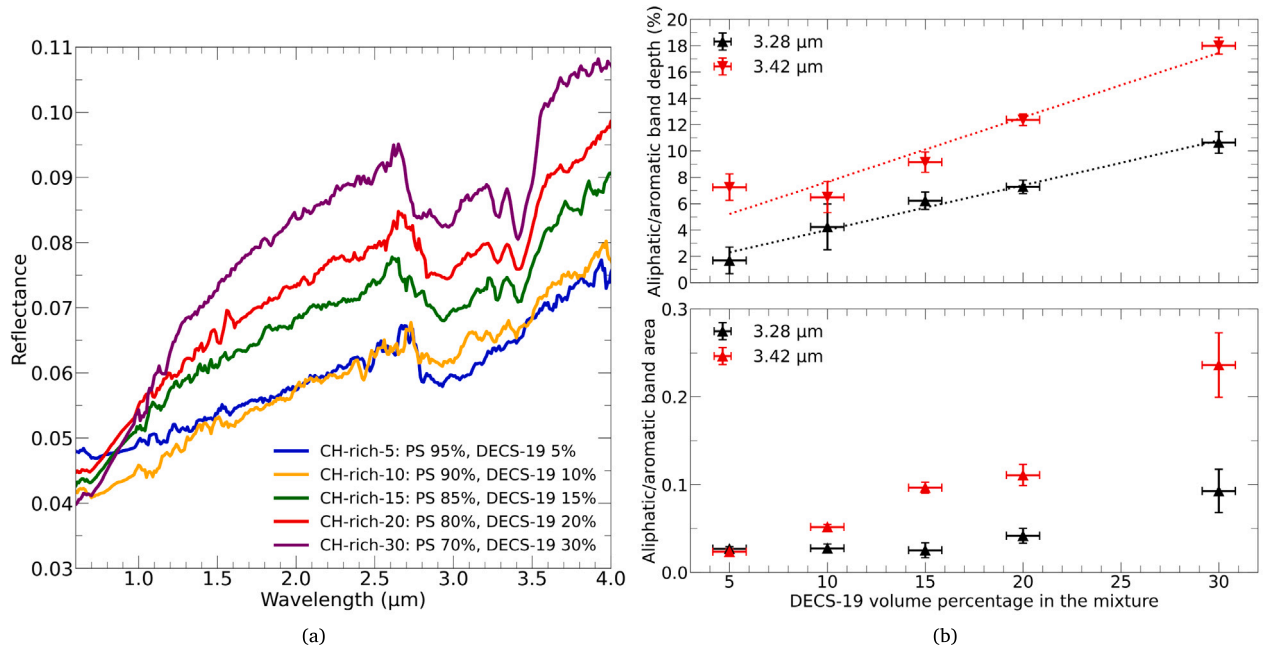

(a) (b)

Fig. 6. (a) Reflectance spectra of the mixtures CH-rich-5, -10, -15, -20, and -30, based on the PSD simulant with addition of various quantities of organics, from 5 to 30 vol.%. Spectra are smoothed on these figures using a moving average of 3 points. (b) Top: Band depth of the 3.28 and 3.42 μm features as a function of the quantity of the organic compounds in PSD. Bottom: Band area of the 3.28 and 3.42 μm features as a function of the quantity of the organic compounds in PSD. Band areas are computed respectively from 3.2 μm to 3.35 μm and from 3.35 μm to 3.6 μm.

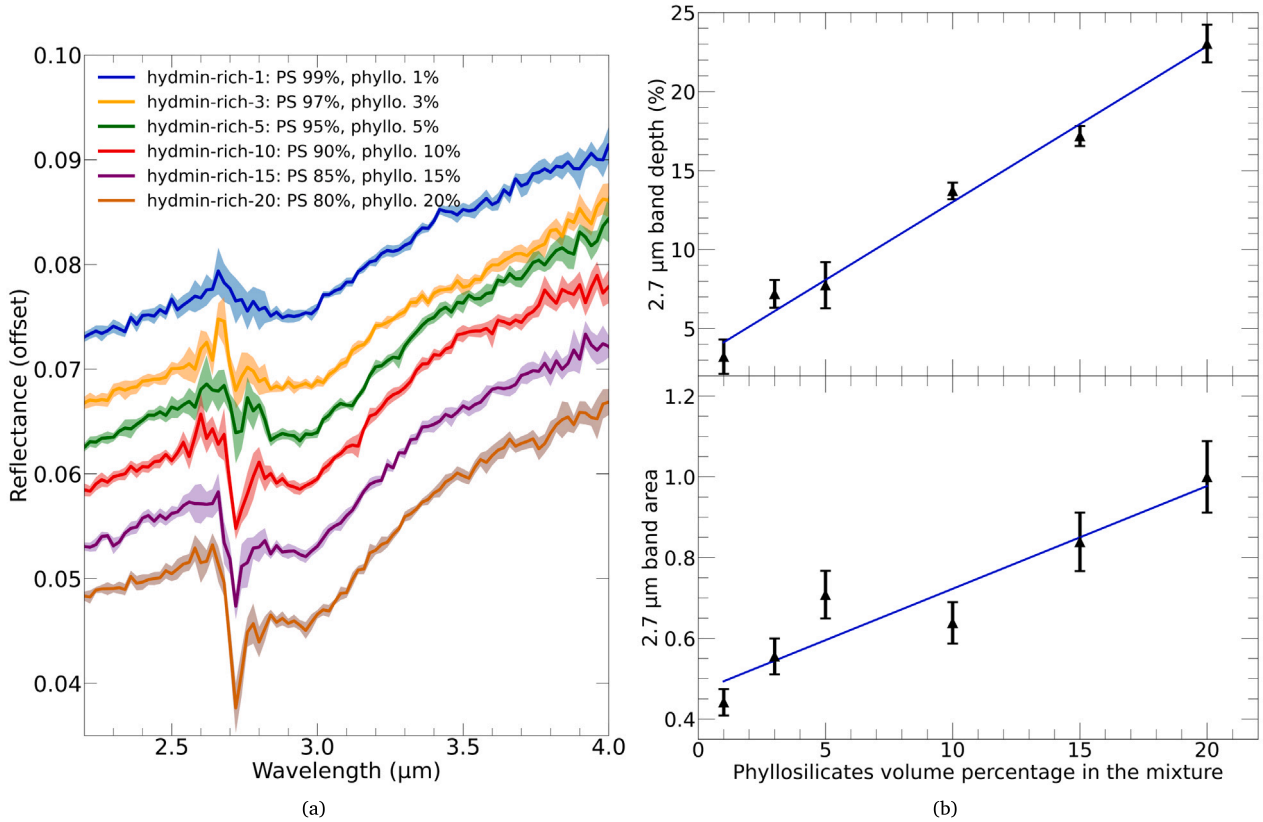

(a) (b)

Fig. 7. (a) SHADOWS reflectance spectra of the mixtures hydmin-rich-1, -3, -5, -10, -15, and -20, based on the PSD simulant with addition of various quantities of phyllosilicates, from 1 to 20 vol.%. The shaded areas correspond to the uncertainties of the measurements. (b) Top: Band depth of the 2.7 μm feature as a function of the quantity of the hydrated minerals in PSD. Bottom: Band area of the 2.7 μm feature as a function of the quantity of the hydrated minerals in PSD. Band areas are computed from 2.6 μm to 3.4 μm, hence by taking into account the 3 μm feature. Band areas are normalized to the maximum value obtained for 20 vol.% in the simulant.

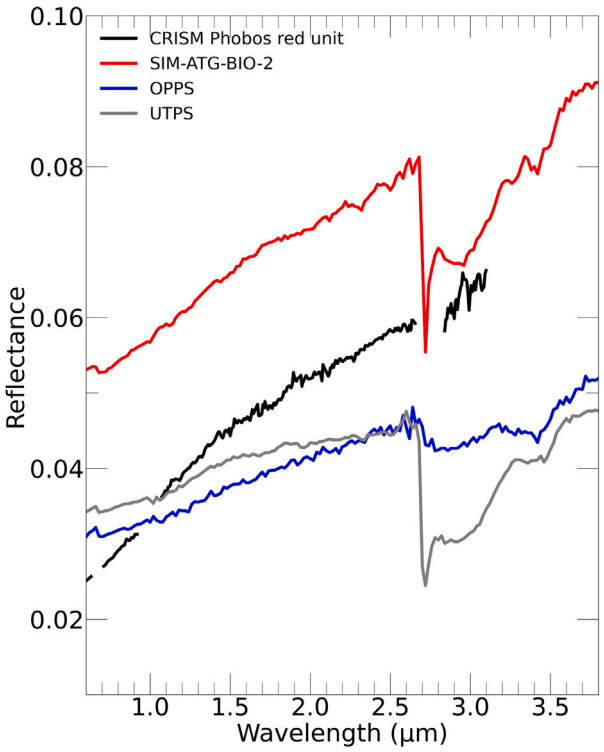

Fig. 8. Visible and near-infrared spectra of mixtures SIM-ATG-BIO-2 and SIM-SAP-1 (OPPS) compared to the Phobos red unit spectrum (Fraeman et al., 2014) reprojected to laboratory geometry (i = 0°, e = 30°). Spectrum of the UTPS simulant is also show for comparison (Miyamoto et al., 2021).

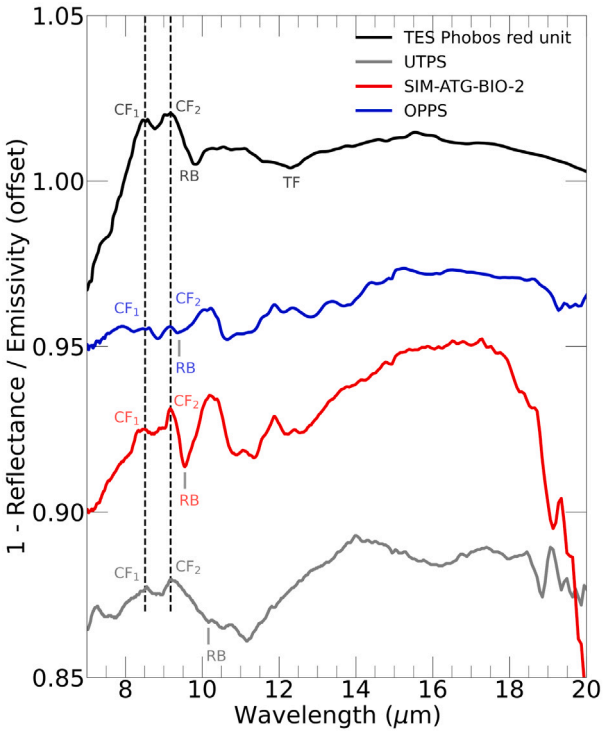

Fig. 9. Mid-infrared spectra of mixtures SIM-ATG-BIO-2 and SIM-SAP-1 (OPPS) compared to TES spectrum of Phobos from Glotch et al. (2018). Spectrum of the UTPS simulant (Miyamoto et al., 2021) is also show for comparison. The UTPS spectrum was measured on a powder composed of grains <125 μm. The two vertical dashed line represent the position of the Christiansen features of the TES Phobos spectrum at 8.59 μm and 9.17 μm. Spectra are offset for clarity.

(Fig. 7(a)). However, the band is still clearly visible and do not have effect on the detectability. This effect will be important to take into account for quantification purpose. Band depth ranges from 3% to 23%. For a same volume fraction, hydrated mineral feature are two times deeper than the organics features at 3.28 and 3.42 μm.

3.5. Update of the Phobos simulant

We tried to reproduce the main properties of the Phobos spectrum using spectra from the visible to the mid-infrared (see also Wargnier et al. 2023b), using the spectral properties observed at different geometries of observation. Table 1 describes the mixtures made for this study. We compared the different mixtures in terms of VNIR spectral slope and reflectance and MIR absorption bands positions. Spectral parameters of a laboratory simulant in the VNIR were already studied previously (Wargnier et al., 2023b). The best-fit mixture compared to CRISM spectrum of Phobos (Fraeman et al., 2012) was found to be a mixture of olivine (60 vol.%, 50–100 μm), anthracite (20 vol.%, <1 μm) and DECS-19 (20 vol.%, <50–100 μm). We chose to use this VNIR Phobos simulant as the basis of the new investigations. As discussed previously (Sections 1 and 3.4), phyllosilicates have been found to be a possible explanation of the features observed in the MIR. Hence, phyllosilicates were added to a mixture of olivine, anthracite, and DECS-19. According to pure endmembers spectra (Section 3.2), saponite, biotite, antigorite, and nepheline were selected to match the Phobos MIR spectrum. We found that a mixture composed of biotite and antigorite is indeed a good simulant for the MIR spectrum of Phobos as shown in Giuranna et al. (2011). Positions of CF, RB, and TB are consistent with the Phobos spectrum.

However, the VNIR spectrum of this simple mixture is not in agreement with the Phobos spectrum in this wavelength range. Mixtures that match well Phobos spectra from the VNIR to the MIR are quite complicated mixtures composed of 4 to 5 endmembers (SIM-ATG-BIO, SIM-NEP, SIM-ATG-SAP, and SIM-SAP). Looking at VNIR spectra of the different mixtures (Fig. 8 and Table 4), we observed that most of them are quite good in terms of spectral slope except the SIM-ATG-BIO-1 mixture. Spectral slopes of SIM-ATG-BIO-1 are too low compared to Phobos spectral slope. SIM-ATG-BIO-1 does not contain DECS-19. As seen in Wargnier et al. (2023b), DECS-19 is an important endmembers for the spectral slope in the VNIR and few percent can change drastically the slope. The steeper slopes in the visible appear to be linked with the presence of nepheline and a high quantity of DECS-19 (20 vol.%). From 1.5 to 2.4 μm, the slopes show less variations and are comprised between 1.13%/100 nm and 2.82%/100 nm. These last values are close to the slope value in the same wavelength range found in the Phobos CRISM spectrum (Fraeman et al., 2012).

Reflectance of the different mixtures is comprised between 0.03 and 0.06 at 600 nm whereas the reflectance of the Phobos spectrum at this wavelength is about 0.025. Therefore, for most of the mixtures, the reflectance is slightly higher than Phobos. Using these endmembers it is difficult to decrease the reflectance level without any significant changes for the spectral slope. All mixtures except SIM-ATG-BIO-1 exhibit two organics bands at 3.28 and 3.42 μm due to DECS-19. These bands are more or less important depending on the quantities of DECS-19 and of anthracite. Mixtures containing phyllosilicates present the 2.7 μm O–H feature. Mixtures with nepheline instead of phyllosilicates do not have this absorption band but show a 3 μm feature. Except for O–H and C–H features, other bands that can be seen in pure endmembers spectra (Fig. 4(b)) are completely removed.

In the mid-infrared range, mixtures reveal different behaviors depending on the composition (Fig. 9), in particular looking at the CF, RB, and TF. Positions of the three main features for the mixtures are given in Table 4. Mixtures containing nepheline are flatter than

Table 4
Spectral parameters of the spectroscopic simulant mixtures in the visible and near-infrared and positions of the mid-infrared features CF, RB, and TF. Comparison with CRISM and UTPS-TB spectral parameters. CRISM and UTPS parameters are derived from spectra respectively in Fraeman et al. (2012) reprojected at the same laboratory geometry and Miyamoto et al. (2021). A hyphen in the Table signifies that there is no data at this wavelength for the observation. Uncertainties on the spectral slope and reflectance measurements for the mixtures are due to SHADOWS uncertainties. The spectral slope is given in %/100 nm. SIM-SAP-1 is chosen in this work as the best simulant in the VNIR for Phobos (OPPS). Values for MIR features position are given with uncertainties of 0.05 μm. In this table, because Phobos has a unique RB, only the position of the first RB of the simulants is given.

Mixtures	Spectral slope (in %/100 nm)			Reflectance			MIR features position (μm)		
	720–900 nm	1.5–2.4 μm	3.7–4.0 μm	600 nm	1.8 μm	4.0 μm	CF(s)	RB	TF
SIM-ATG-BIO-1	0.09 ± 0.01	1.29 ± 0.03	1.05 ± 0.04	0.052 ± 0.001	0.056 ± 0.001	0.074 ± 0.002	8.34/9.17	9.55	12.20
SIM-ATG-BIO-2	3.16 ± 0.01	1.84 ± 0.04	1.26 ± 0.04	0.053 ± 0.001	0.070 ± 0.001	0.093 ± 0.002	8.34/9.17	9.55	12.15
SIM-ATG-BIO-3	3.15 ± 0.02	2.42 ± 0.05	2.55 ± 0.07	0.040 ± 0.001	0.056 ± 0.001	0.082 ± 0.002	8.34/9.16	9.55	12.14
SIM-NEP-1	3.49 ± 0.01	2.48 ± 0.05	1.45 ± 0.05	0.044 ± 0.001	0.062 ± 0.001	0.091 ± 0.002	9.13	9.61	12.20
SIM-NEP-2	5.59 ± 0.02	2.82 ± 0.05	1.59 ± 0.05	0.038 ± 0.001	0.060 ± 0.001	0.090 ± 0.002	9.16	9.57	12.20
SIM-ATG-BIO-4	2.53 ± 0.01	2.08 ± 0.06	1.04 ± 0.04	0.039 ± 0.001	0.051 ± 0.001	0.070 ± 0.002	8.34/9.18	9.55	12.09
SIM-NEP-4	5.38 ± 0.02	2.76 ± 0.06	1.90 ± 0.06	0.030 ± 0.001	0.047 ± 0.001	0.071 ± 0.002	9.34	9.57	12.20
SIM-ATG-SAP-1	2.05 ± 0.01	1.18 ± 0.02	1.69 ± 0.05	0.059 ± 0.001	0.073 ± 0.001	0.093 ± 0.002	8.41/9.20	9.54	12.80
SIM-ATG-SAP-2	3.42 ± 0.01	2.17 ± 0.03	1.80 ± 0.06	0.042 ± 0.001	0.059 ± 0.001	0.082 ± 0.002	8.41/9.20	9.54	12.80
SIM-SAP-1 (OPPS)	2.55 ± 0.01	2.42 ± 0.06	–	0.034 ± 0.001	0.045 ± 0.001	–	8.41/9.20	9.36	–
UTPS-TB	1.53 ± 0.02	1.09 ± 0.04	−0.71 ± 0.06	0.030 ± 0.001	0.037 ± 0.001	0.040 ± 0.001	8.56/9.18	10.16	11.87
CRISM	**8.78 ± 0.05**	**2.99 ± 0.06**	–	**0.025 ± 0.005**	**0.049 ± 0.003**	–	–	–	–
TES	–	–	–	–	–	–	**8.59/9.17**	**9.82**	**12.30**

the others with antigorite, biotite, and saponite; and CF are not well defined but are in the range of the double CF observed in the TES Phobos spectrum (Glotch et al., 2018). Mixtures containing saponite and the mixture of antigorite and biotite present an interesting double CF at the position of the CF given by the TES Phobos spectrum. Reststrahlen bands positions do not change within uncertainties with the composition of the mixture. Indeed, this feature is mainly related to the silicate class and therefore all phyllosilicates show a close RB in position and shape. For the different mixtures, TFs were found in the range 12.09–12.80 μm.

Although a quantitative study cannot be made of the emissivity value, as the spectra were transformed from reflectance to emission using Kirchhoff's law, it is interesting to note that the various mixtures present a high emissivity of around 0.95 at 8 μm. This order of magnitude of emissivity is in agreement with the emissivity at the same wavelength measured on Phobos by TES of approximately 0.99.

According to the spectral slopes, the reflectance, the different positions of the features, and of the overall shape of the spectrum, SIM-ATG-BIO-2 and SIM-SAP-1 were chosen as the best Phobos spectral simulants from the VNIR to the MIR. They appear to be a great compromise between the different spectral parameters described above. It should be noted that we have used here the MIR spectrum given in Glotch et al. (2018), but that the Phobos MIR spectra of Giuranna et al. (2011) show significant variations with the latter. It is therefore difficult to draw definitive conclusions in this spectral range. Although SIM-ATG-BIO-2 has spectral properties more similar to those of Phobos, SIM-SAP-1 was chosen due to its composition, which includes saponite. This mixture is interesting because endmembers are likely more representative, particularly for martian-like materials on the Phobos surface (giant impact hypothesis). It enables exploration of a composition that is very different from the UTPS-TB simulant.

The new Phobos simulant SIM-SAP-1 will be called OPPS (Observatory of Paris Phobos Simulant) in the following for the sake of clarity. The mineralogical composition of the OPPS is presented in Table 1, the bulk chemical composition from EDX analysis in Table A.2, and the SEM images in Fig. A.1.

3.6. The effects of the geometry of observation

The geometry of observation is of crucial importance for remote-sensing investigations of small bodies. Several studies have shown the variation of the reflectance and slope with the illumination angles, using remote-sensing data (e.g., Clark et al. 2002), and from laboratory investigations (e.g., Pommerol et al. 2013, Yoldi et al. 2015, Jost et al. 2016, 2017b,a, Potin et al. 2022).

In this work, we studied the variations of the organic and hydrated minerals band depth with phase angle. We also have a look at the evolution of the spectral slope with the geometry (i.e., phase reddening), and we mainly focused our measurements and analysis on the evolution of the reflectance with the phase (i.e., phase curve).

3.6.1. Band depth

Evolution of the organic band's depth.

Previous papers have shown that organic features band depth could be slightly modified (e.g., Fornasier et al. 2020, Wargnier et al. 2023a) for high phase angle. Hence, to better understand parameters that can influence organic matter detection in IR spectroscopy, it is crucial to explore the effects of observation geometry, in particular on the band depth.

We acquired 13 spectra of a mixture 70 vol.% PSD, 30 vol.% DECS-19 with phase angle from 24° to 140°. For each spectrum, we determined the band depth of the 3.28 and 3.42 μm absorption bands to plot them according to the phase angle of the measurement. The result of this investigation is given in Fig. 10. We can note the difference in the band depth between measurements in Figs. 6(b) and 10. Different measurements were acquired on this mixture and the surface observed of the mixture is thus different between the nominal geometry configuration and the BRDF measurement. In Fig. 10, we noticed a quite constant behavior of the band depth as a function of the phase angle, except at large phase angles (>100°) where the band depth is severely reduced. The band depth is also directly related to the mixture observed and to the SHADOWS reflectance measurements. The latter is strongly dependent on the surface observed by SHADOWS that varies even between measurements for the same phase angle, with different incidence and emission angles. For a given phase angle, variations of the band depth parameter are quite small, generally lower than 4%.

Evolution of the hydrated minerals band's depth.

Similar to the investigation of organics, we analyzed the evolution of the 2.7 μm band depth using BRDF measurements on the UTPS and OPPS simulants (Fig. 11). The band depth did not show a clear pattern in its evolution with the phase angle. However, it was observed that the minimum band depth was consistently computed for the larger phase angle (120–130°). This minimum observed at large phase angle demonstrates weak systematic behavior: it may only result in a 1% reduction of the band depth or the feature may be significantly reduced by a factor of two.

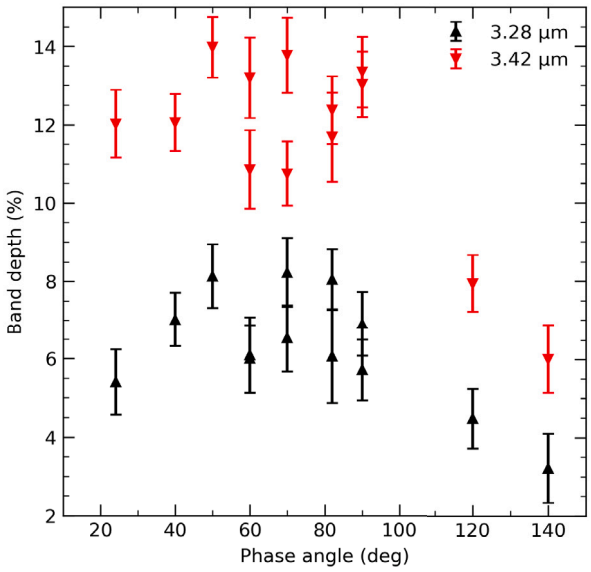

Fig. 10. Geometry observation effects on the 3.28 µm and 3.42 µm band depth for a mixture composed of PSD (70 vol.%) and DECS-19 (30 vol.%). Red triangles represent points for the 3.42 µm absorption band depth and black triangles represent points for the band depth of the 3.28 µm feature. Measurements for this mixture were made with incidence and emission angles ranging from 12° to 70°. Points at a same phase angle correspond to various incidence and emission configuration.

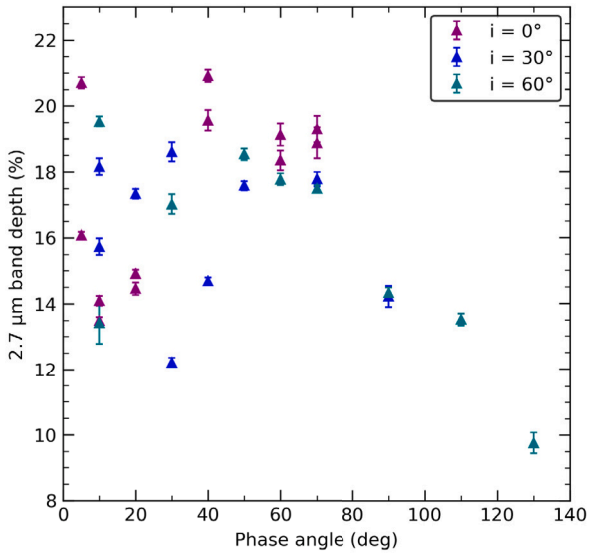

Fig. 11. Evolution of the 2.7 µm band due to hydrated minerals in the OPPS simulant with the phase angle and the incidence angle.

We do not acquire data at phase angles lower than 5° due to instrumental limitations. Our measurements were not affected by the opposition effect which generally occurs for phase angles less than 10° (Hapke, 1986; Kitazato et al., 2008; Fornasier et al., 2015, 2020). For further investigation, the evolution of the bands at very small phase angles should be examined, as only a few measurements of opposition exist in the literature (e.g., Nelson et al. 2000).

Some studies exist in the literature about variability of features with the geometry from laboratory measurements or from remote-sensing data. For example, the evolution of the 3 µm feature (Pommerol and Schmitt, 2008; Takir et al., 2015; Potin et al., 2019; Wargnier et al., 2023a), the 0.6 µm absorption band (Shepard and Cloutis, 2011), the 2.74 µm band (Fornasier et al., 2020) were investigated. All these works have shown the same effect we observed in this paper, namely that there are no significant variations in the band depth with phase angle and/or that decreases in the absorption band depth are possible for very high phase angles.

3.6.2. Phase reddening

We have computed the phase reddening coefficient γ and the zero-parameter Y_0 to provide additional information for the interpretation of future Phobos observations. The OPPS exhibits $\gamma = 0.013 \pm 0.002$ 10^{-4} nm^{-1}/° and $Y_0 = 1.9 \pm 0.1$ %.(100 nm)$^{-1}$. We found $\gamma = 0.012 \pm 0.002$ 10^{-4} nm^{-1}/° and $Y_0 = 0.83 \pm 0.09$ %.(100 nm)$^{-1}$ for the UTPS sample. These phase reddening parameters were computed based on a linear phase reddening assumption and from a spectral slope between 1.5 and 2.4 µm. For a discussion on phase reddening in the Phobos context, the reader is referred to Wargnier et al. (2023a,b). The phase reddening is a complex phenomenon and is generally attributed to the microscopic roughness (i.e., microns/sub-microns scale, Beck et al. 2012, Schröder et al. 2014) or increase of multiple scattering at large phase angle with the wavelength (Hapke et al., 2012).

3.6.3. Phase curve

One of the main objective of this paper is to examine the evolution of the reflectance with the phase angle. The phase curve provides valuable insights into the surface, particularly its texture, and can provide crucial information for optimizing future observations of the JAXA/MMX mission, such as exposure time. The measurements indicate a decrease in reflectance from 0 to 70°, followed by an increase in reflectance at phase angles greater than 70–80° (Figs. 12 and 13). The measurements appear to be quite scattered, in particular with a significant reflectance variability for the measurements at $\alpha = 5°$. This variance is due to the fact that a measurement at a given phase angle is obtained with several combinations of incidence and emission angles. In particular, the incidence angle seems to have an extremely important effect at low phase angles (Wargnier et al., 2023b). In order to quantitatively compare with other laboratory measurements or with *in situ* data, we modeled the phase curve of the Phobos simulants using the Hapke IMSA model (Hapke, 2012). A broad collection of incidence and emergence angles allows better constraining of Hapke parameters like the average roughness slope.

To avoid too many free parameters, we first set the single-lobe Henyey–Greenstein (1T-HG) function as single particle phase function into the IMSA model. However, this function fails to fit the measurements because of the strong forward-scattering that occurs at high phase angle. Therefore, we used the two-term Henyey–Greenstein (2T-HG) described in Section 2.5.2.

Using MCMC inversion to fit the IMSA model to the experimental phase curves of the simulants, we were able to constrain the parameters (Figs. 12 and 13). The six Hapke parameters are then used to model the phase curve. The residuals of this fit are relatively low, except at $\alpha = 5°$ where the data variance lead to higher residuals. Table 5 presents the derived Hapke parameters.

4. Discussion

4.1. Spectroscopic and composition similarity of OPPS with Phobos

Whereas the UTPS was primarily developed as a Tagish Lake simulant with a similar mineral composition, we developed the OPPS simulant mainly based on the spectroscopic properties of the mixture of various materials from minerals to organics. Because the VNIR spectrum of Phobos (Murchie et al., 1991; Murchie and Erard, 1996; Rivkin et al., 2002; Fraeman et al., 2012, 2014; Pajola et al., 2012, 2018; Takir et al., 2022; Mason et al., 2023) shows no clear absorption band, the composition of a Phobos simulant necessarily difficult to match with

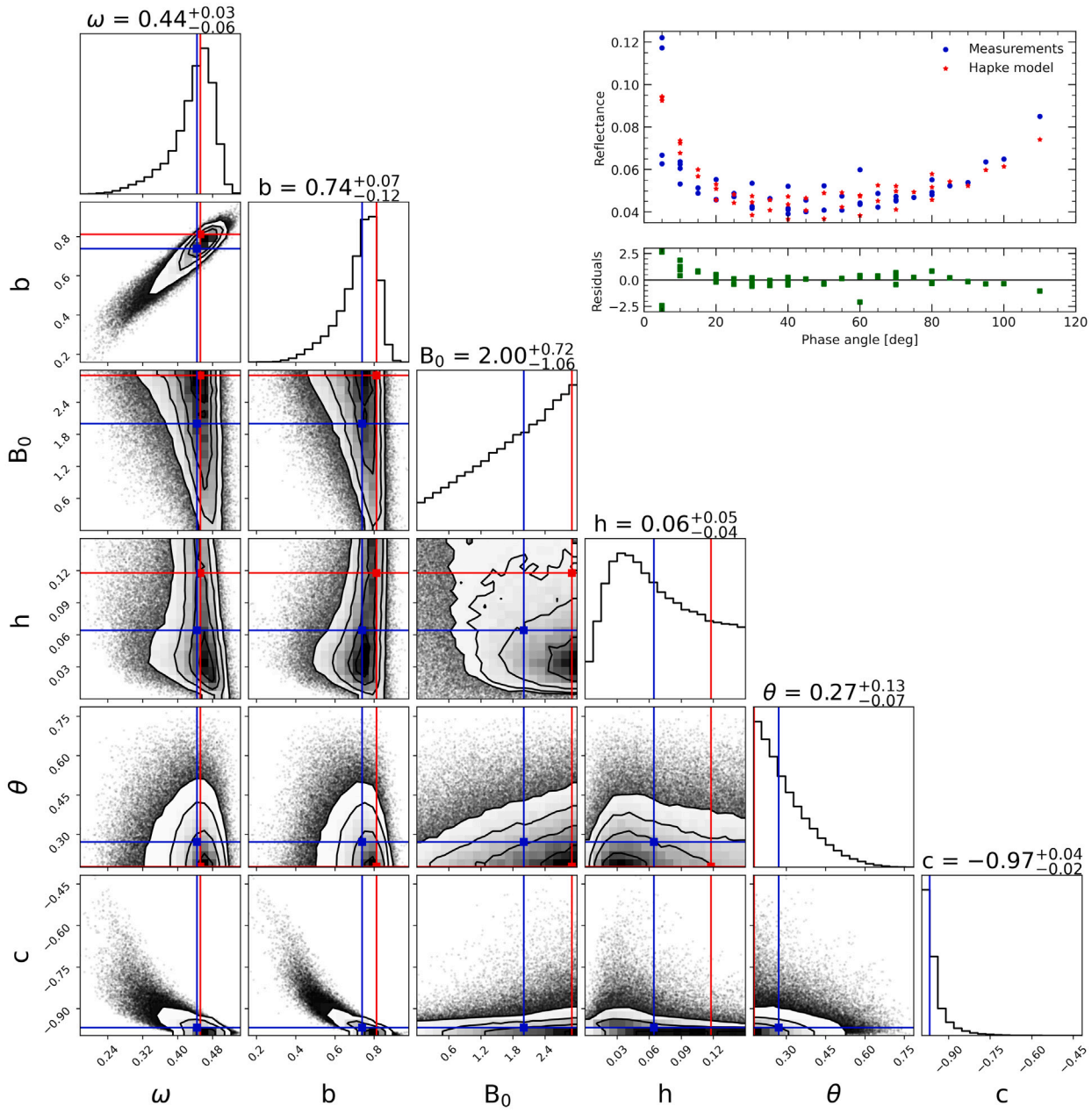

Fig. 12. Posterior probability density function (PDF) of the Hapke parameters from the UTPS phase curve inversion. Each 1D histogram represents the 45 000 accepted solutions. The 2D histograms show the correlation between the parameters. The blue line represents the median for a given parameter and the red line is the MLE. We chose to use the median of the parameter as the best-fit parameter. The values and the associated uncertainties are given as title of the 1D histogram. Top right: Hapke modelization using the best-fit parameters found from the MCMC inversion, compared to the experimental UTPS phase curve. The residuals are also plotted, and given in percent. (For interpretation of the references to color in this figure legend, the reader is referred to the web version of this article.)

the unknown Phobos' surface composition. Assumptions are therefore necessary when trying to develop a Phobos simulant. As discussed in Section 2.1, some materials (olivine, saponite) used for the development of the OPPS simulant were found in both martian regolith/rocks and extraterrestrial samples. Other materials (anthracite and DECS-19) are not expected to be present in the exact same form in the Phobos regolith but they are useful proxies for simulating the spectroscopic properties. Additionally, the objective of a simulant is not to reproduce perfectly the surface of the body of interest; rather it is to provide the best possible match of one of the properties of the surface (mechanical, spectroscopic, photometric, composition, ...). In particular, Miyamoto et al. (2021), Poggiali et al. (2022), and Wargnier et al. (2023b) have demonstrated the necessity of dark opaque materials to reduce the reflectance level of the samples to reach the low albedo of Phobos. The MIR properties help to constrain the possible composition, but the spectroscopic properties in this wavelength range are also affected by a large numbers of parameters. For example, the shape and contrast of the RB could also be modified by grain size (Salisbury et al., 1991). Since the grain sizes used in the mixtures are the same for a given endmember in this study, we do not observe a relative modification of the RBs. However, the RBs (~9.5 μm) of our Phobos simulants are systematically shifted toward shorter wavelengths compared to the Phobos spectrum (~9.8 μm). Interestingly, using ion irradiation to simulate space weathering, Brunetto et al. (2020) noticed a shift of the RB toward longer wavelengths for the irradiated surface which could explain the difference between fresh and altered samples. In order to be easily reproduced, we also chose to find a good spectroscopic and photometric simulant with less possible endmembers. In addition to the

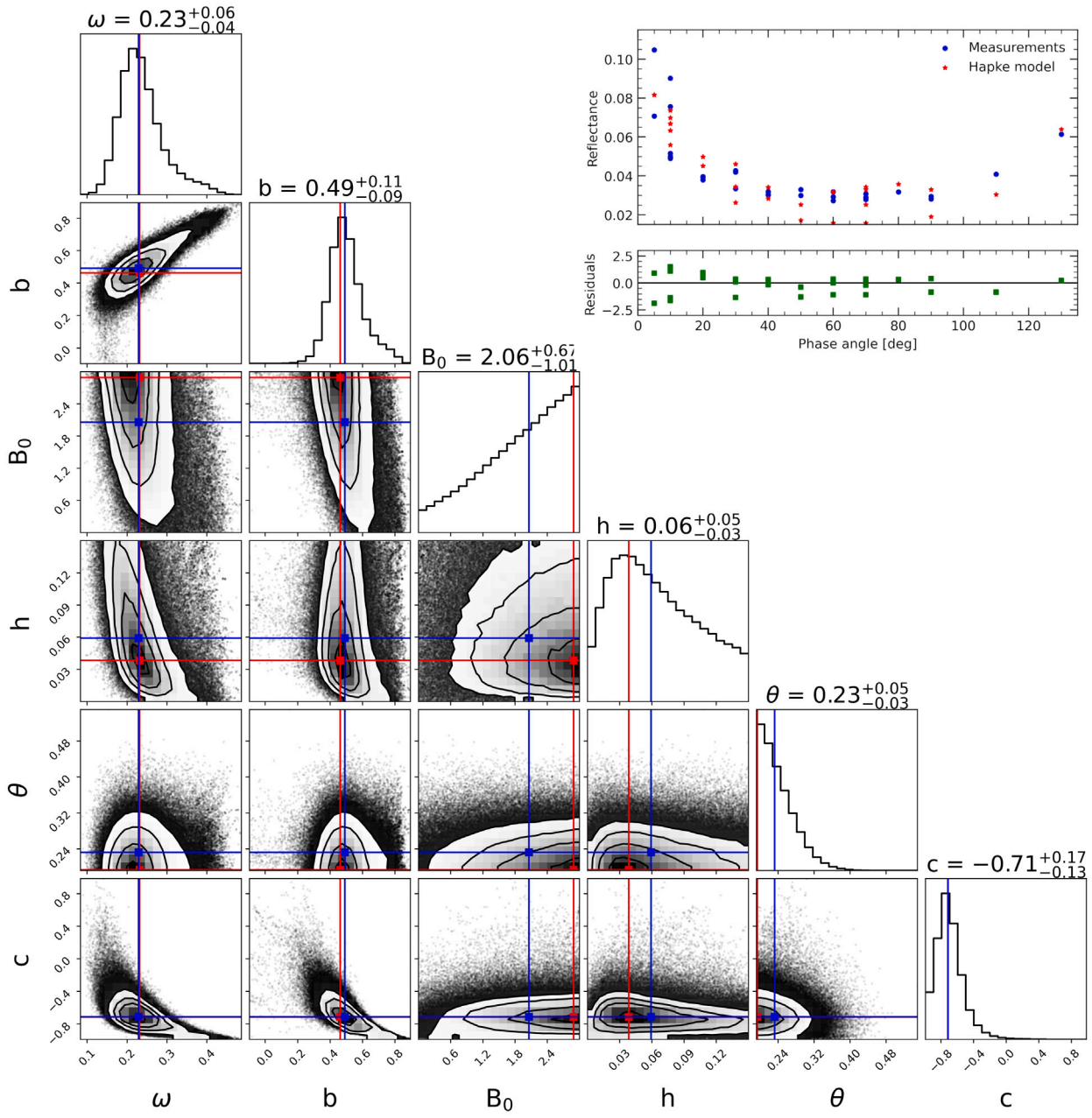

Fig. 13. Posterior probability density function (PDF) of the Hapke parameters from the OPPS phase curve inversion. Each 1D histogram represents the 45 000 accepted solutions. The 2D histograms show the correlation between the parameters. The blue line represents the median for a given parameter and the red line is the MLE. We chose to use the median of the parameter as the best-fit parameter. The values and the associated uncertainties are given as title of the 1D histogram. Top right: Hapke modelization using the best-fit parameters found from the MCMC inversion, compared to the experimental OPPS phase curve. The residuals are also plotted, and given in percent. (For interpretation of the references to color in this figure legend, the reader is referred to the web version of this article.)

UTPS simulant proposed by Miyamoto et al. (2021), we believe that the OPPS simulant can be another interesting Phobos and Deimos simulant for further studies.

4.2. Comparison of the Hapke parameters

It appears very challenging to compare directly Hapke opposition effect parameters values obtained in laboratory and from remote-sensing data. The opposition effect especially appears to be stronger with *in situ* data and the reflectance increases also extremely rapidly at large phase angles in laboratory indicated a strong forward-scattering (e.g., Fornasier et al. 2024). However, we can more easily compare the obtained Hapke parameters with those associated to other laboratory experiments. Some studies are of particular interest in the case of Phobos. For example, Beck et al. (2012) made a photometric studies of meteorites including carbonaceous chondrites (Tagish Lake, Orgueil, Allende), diogenite (tatahouine), ordinary chondrite (Forest Vale, H4) and MAC 88 105 lunar meteorite, Pommerol et al. (2013) obtained the phase curve of the JSC Mars-1 analog, and Mandon et al. (2021) measured the bi-directional reflectance distribution function (BRDF) of a martian meteorite (shergottite). However, Mandon et al. (2021) does not apply any inversion technique to model parameters to their phase curve. We therefore decided to perform the inversion on this dataset using the same method as for our measurements, to allow quantitative comparison with the other studies. The comparison of the lunar and martian meteorites with the Phobos surface and Phobos simulants is of interest, given the expectation that materials formed at

Table 5
Hapke parameters derived from experimental phase curve at 0.6 μm measured with SHADOWS on different samples. The inversion was made using the MCMC method.

Sample type	Sample	w	g or b[f]	c	$B_{sh,0}$	h_{sh}	$\bar{\theta}$	References
Powder	UTPS	$0.44^{+0.03}_{-0.06}$	$0.74^{+0.07}_{-0.12}$	$-0.97^{+0.04}_{-0.02}$	$2.00^{+0.72}_{-1.06}$	$0.06^{+0.05}_{-0.04}$	$15.46^{+2.29}_{-1.15}$	This work
	OPPS	$0.23^{+0.06}_{-0.04}$	$0.49^{+0.11}_{-0.09}$	$-0.71^{+0.17}_{-0.13}$	$2.06^{+0.67}_{-1.01}$	$0.06^{+0.05}_{-0.03}$	$13.18^{+2.86}_{-1.72}$	This work
	Tagish Lake[a]	0.157	0.431	−0.436	0.334	0.023	14.1	Beck et al. (2012)
	Allende[a]	0.399	0.366	−0.318	0.720	0.020	12.8	Beck et al. (2012)
	Lunar Meteorite[a]	0.850	0.746	−0.956	0.843	0.000	25.7	Beck et al. (2012)
	JSC Mars-1[b]	0.526	0.187	0.454	1.0	0.083	13.3	Pommerol et al. (2013)
	NWA 4766[c]	$0.94^{+0.02}_{-0.02}$	$-0.03^{+0.27}_{-0.24}$	$0.15^{+0.71}_{-0.99}$	$1.85^{+0.80}_{-1.01}$	$0.11^{+0.03}_{-0.05}$	$24.64^{+9.74}_{-6.87}$	Mandon et al. (2021) and this work
Phobos[d]		0.070	−0.13	N/A	4^{+6}_{-1}	0.055 ± 0.025	22 ± 2	Simonelli et al. (1998)
Phobos[e]		0.074 ± 0.002	−0.301 ± 0.007	N/A	2.283	0.0573	24	Fornasier et al. (2024)

[a] For these samples, Beck et al. (2012) used estimate uncertainties from Shepard and Helfenstein (2007).
[b] The reader is referred to Pommerol et al. (2013) for associated uncertainties of the Hapke parameters. The B_0 parameter was set with bounds [0,1].
[c] We used the BRDF data of NWA 4766, a basaltic shergottite, from Mandon et al. (2021) to retrieve the Hapke parameters using the same inversion methods as our samples. It is important to note that the laboratory measurements from Beck et al. (2012) and Mandon et al. (2021) were performed on non-sieved powder but with an average size of 20 μm.
[d] Phobos Hapke parameters derived in Simonelli et al. (1998) from Viking mission data acquired with a clear filter.
[e] Phobos Hapke parameters derived in Fornasier et al. (2024) from the Mars Express HRSC/SRC dataset in the green filter.
[f] g for 1T-HG and b for 2T-HG.

high temperatures, such as basalt, should be present at least partially at the surface in the giant impact scenario.

4.2.1. Single-scattering albedo

The single-scattering albedo (SSA) of the UTPS and the OPPS show significant differences (Table 5). The SSA value for UTPS falls between the values for the Allende meteorite and the JSC Mars-1 analog, but both are larger than the Tagish Lake meteorite SSA.

As it can be noticed in Table 5, the single-scattering albedo ω (SSA) appears to be much higher with laboratory experiments, compared to the remote-sensing data. All dark samples including Tagish Lake, Allende have a SSA larger than 0.1. In particular, despite the very dark appearance of the simulants and the reflectance measurements (3%–4% at 600 nm), the SSA of these samples are 30 to 60 times higher than the value of the Phobos surface derived from photometric observations (Simonelli et al., 1998; Fornasier et al., 2024). The discrepancy between laboratory investigations and in-situ data can be attributed to two main factors. First, the grain size distribution is not the same in the laboratory as it is on the surface of small bodies. While the grain sizes used in this work are relatively small (<100 μm), asteroids generally have a wider grain size distribution (e.g., Dellagiustina et al. 2019, Michikami et al. 2019, Burke et al. 2021, Ogawa et al. 2022), sometimes with the presence of boulders (e.g., Dellagiustina et al. 2019, Michikami et al. 2019) that scatter light differently than small grains. This grain size effect could lead to the observation of a higher SSA. The other main reason is linked to the space environment in which asteroids evolve. Surface grains are exposed to space weathering, which modifies their spectroscopic, photometric, and chemical properties, and the low-gravity environment implies also that the surface is likely organized differently from the samples studied in the laboratory, with voids between particles, high micro-/macro-porosity, and high micro-/macro-roughness. The aforementioned differences imply that the laboratory phase curves always exhibit different behavior compared to small bodies phase curves derived from remote-sensing data. This results in a different SSA when applying the Hapke model.

It is also essential to note that the SSA is not really something observable, but rather a modeling parameter that describes the light behavior on this grain. More precisely, it represents the albedo in the ideal case of an isolated single particle.

4.2.2. Opposition effect

The opposition effect is a relatively well-known effect that occurs in planetary surface and leads to a nonlinear increase of the reflectance at low phase angles (e.g., Hapke et al. 1998). Despite the fact that laboratory measurements at a very low phase angle are rare, it is possible to extrapolate the SHOE trend for very small phase angles from measurements at $\alpha = 5°–10°$ using photometric model. By applying the Hapke IMSA model, we have been able to obtain the relative opposition effect (Beck et al., 2012), defined as the ratio of the reflectance at $\alpha = 0°$ to that at $\alpha = 30°$ (i = 0°, e = 30°). Fig. 14 shows the relative opposition effect intensity (ROEI) as a function of the reflectance for the carbonaceous chondrites investigated in Beck et al. (2012), for the JSC Mars-1 analog (Pommerol et al., 2013), for the NWA 4766 shergottite (Mandon et al., 2021), and for the two Phobos simulants from this work. It appears that the simulants have an SSA similar to Tagish Lake, Orgueil, or Allende, but a stronger opposition effect. The ROIE of the simulants is closer than Tagish Lake to the value found for the Phobos surface from remote sensing data (Fornasier et al., 2024). It is also important to note that the shergottite is far from the Phobos values in both SSA and ROIE.

The data obtained in this study were insufficient to accurately determine the SHOE parameters of the Hapke model. However, they do provide some insight into the behavior at small phase angles. From Hapke IMSA inversion, the intensity of the opposition effect (B_0) is the same within the error bars for both simulants, but larger compared to other laboratory investigations such as Tagish Lake. The half-width of the shadow-hiding opposition effect h_{sh} of the simulants appears to be larger than that of carbonaceous chondrites, but smaller than that of the JSC Mars soil analog and the NWA 4766 shergottite. The CBOE could not be constrained due to laboratory limitations, so we assumed that the entire opposition surge was only due to SHOE. Our findings indicate that Phobos simulants contain opaque scatterers in the sample, with $B_{0,sh} > 1$ (Shepard and Helfenstein, 2007). Future laboratory work should focus on studying the opposition effect, particularly the CBOE.

4.2.3. Surface roughness and phase function

The roughness is comparable for all samples, except for the lunar meteorite studied in Beck et al. (2012), which exhibits approximately twice the values of the others. The b and c parameters of the Phobos simulants indicate a predominantly forward-scattered surface for both, but with a higher and narrower lobe for the UTPS. The UTPS exhibits a scattering behavior similar to that of the lunar meteorite studied in Beck et al. (2012), while OPPS is more similar to the Forest Vale meteorite (Beck et al., 2012). Notably, the shergottite NWA4766 is particularly similar to the Tatahouine meteorite (Beck et al., 2012) in terms of both scattering and opposition effect properties (see Figs. 14 and 15). The JSC Mars-1 (Pommerol et al., 2013) analog exhibits different scattering properties compared to CCs, NWA 4766, and Phobos simulants, with a back-scattering broader lobe.

4.2.4. Hapke model interpretation and limitations

The Hapke model is an interesting tool to try to better understand the surface of planetary bodies. It is particularly invaluable for the

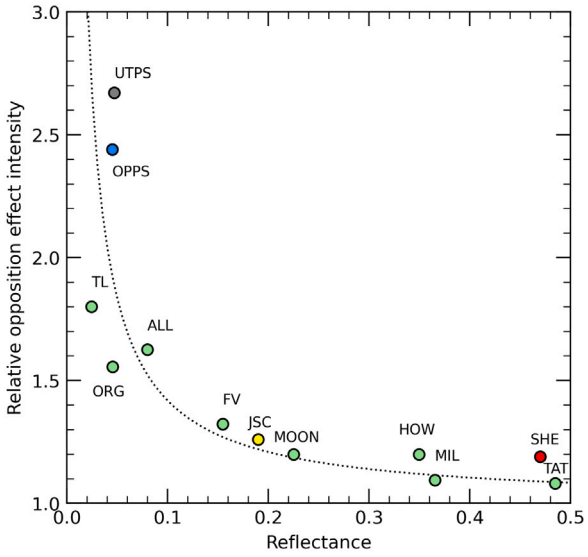

Fig. 14. Relative opposition effect intensity [ratio of the reflectance at $\alpha = 0°$ to that at $\alpha = 30°$ (i = 0°, e = 30°)] of laboratory samples: meteorites (green points) from Beck et al. (2012), JSC Mars-1 analog (yellow point) from Pommerol et al. (2013) and a martian meteorite (basaltic shergottite, NWA 4766; red point) from Mandon et al. (2021) and the two simulants of this study (gray and blue points). Note the small difference in the wavelength used in this work (λ = 600 nm) and in Beck et al. (2012) (λ = 650 nm). The reader is referred to Beck et al. (2012) for more informations about the samples (green points). Phobos ROIE has been found to be higher than the Phobos simulant, with a value of 3.6 (Fornasier et al., 2024). (For interpretation of the references to color in this figure legend, the reader is referred to the web version of this article.)
Source: Figure adapted from Beck et al. (2012).

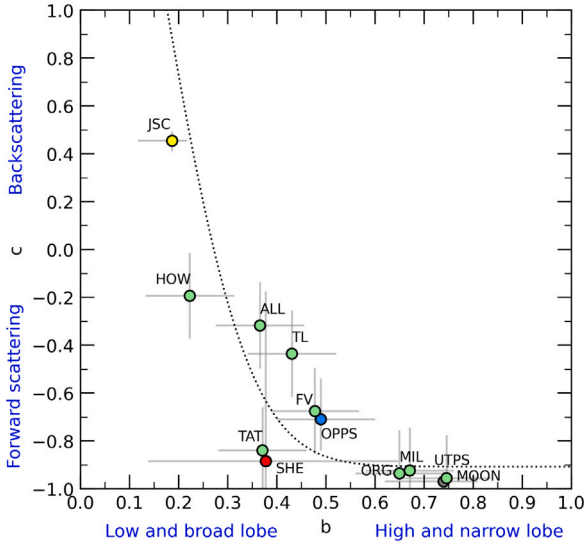

Fig. 15. Asymmetry parameter c as a function of the shape parameter b. The dotted line represents the hockey stick relation (Hapke, 2012).

interpretation of spectroscopic and photometric data from remote-sensing measurements. Because modifications of the reflectance and light scattering could be due to several properties of a surface, and because of the nonlinearity and the relatively large number of free parameters, the global minimum of the model may be complicated to find. The model reflects the extremely complex light scattering process with intrinsic correlations between parameters and functions; like the asymmetric factor and the SSA, or the multiple scattering and the shadow-roughness functions. Therefore, retrieval of the physical properties of the samples from the derived parameters appears to be limited. A perfect BRDF data set should present data from 0° to 180° of phase angle with different incidence angle as suggested by Schmidt and Fernando (2015). High incidence measurements are particularly useful for constraining the photometric parameters, especially the surface roughness $\bar{\theta}$, as noted by Schmidt and Fernando (2015) and Schmidt and Bourguignon (2019). However, it is extremely complicated to obtain such a dataset, and this study presents measurements between 5° and 130°. Then, we found some difficulties to well constrain the B_0, h, and $\bar{\theta}$ parameters. Data at smaller phase angle (<3°) are necessary for B_0 and at large phase angle (>120°) for $\bar{\theta}$.

Additionally, it is well known that b and c are strongly dependent. We have observed a bimodal distribution for b and/or c in several test runs of the MCMC technique. This link between the two parameters is commonly referred to as the hockey-stick relation, as discussed in Hapke (2012), Fernando et al. (2013), and Schmidt and Fernando (2015). Fig. 15 shows this effect with the laboratory measurements performed in Beck et al. (2012), in Pommerol et al. (2013), in Mandon et al. (2021), and in this work.

The two Phobos simulants in this study are spectroscopically and photometrically different from the NWA 4766 shergottite. However, they are closer to it than the JSC Mars-1 analog or other meteorites. The NWA 4766 shergottite is a typical basaltic material from Mars. Regarding the giant impact hypothesis, it would be worthwhile to investigate whether the spectroscopic and photometric behavior of Phobos can be replicated by reproducing space weathering on a Martian meteorite.

4.3. Implications for MMX observations of Phobos and Deimos

4.3.1. MIRS

With its spectral range (0.9–3.6 μm), MIRS will be able to detect for the first time signatures of hydrated minerals and organics, if present on the surface of Phobos (Barucci et al., 2021). Indeed, the presence of these signatures will give pivotal information about the origins of the two moons.

Observations of the Bennu surface for the OSIRIS-REx mission have shown that faint features with a few percent absorption band depth (~3%) can be detected with a S/N > 100 (Simon et al., 2020a). Hence, the MIRS spectrometer onboard MMX will be able to detect and characterize the 3.4 μm organics bands for more than 10 vol.% (i.e., 4.51 wt% aromatic carbon and 0.87 wt% aliphatic carbon). In particular conditions, this threshold will be probably reduced. For 5 vol.%, corresponding to 0.42 wt% aliphatic carbon and 2.21 wt% aromatic carbon, the detection will be more uncertain as the band depth is around 1%, except for the 3.42 μm in PSD (see Fig. 6(b)). Such a feature can be complicated to detect by remote-sensing IR spectroscopy.

We compared the band depth and band center of our mixtures containing organics in various quantities with low-albedo asteroids. Values for the spectral parameters of these asteroids are given by Hromakina et al. (2022). Simulants with 10, 15, 20 vol.% are close to asteroids of type B, C, P, or X. Of course, we probably do not expect large quantities of organic matter that cover the entire surface of Phobos, but some local variability is still possible. For example, for Bennu, Simon et al. (2020b) have found C–H band depth varies from 1% to more than 10% in some precise locations. Hence, if an organic signature is present on Phobos, we can probably expect the 3.4 μm band depth to be included between 2 and 10%. The expected value of the band depth at 3.4 μm will depend on the formation scenario for Phobos. In the hypothesis of the asteroid capture scenario, for a hydrous asteroid, the 3.4 μm C–H feature will exist with a maximum band depth of 10% (Takir et al., 2019; Hromakina et al., 2022). For a partially dehydrated asteroid, the spectrum will present a 3.4 μm organic absorption band with a maximum depth of 5% (Takir et al., 2019). For a dehydrated asteroid, the existence of the 3.4 μm feature is more uncertain and it will be possibly linked with the presence of IOM (Kaplan et al., 2019). In the others scenarios for the

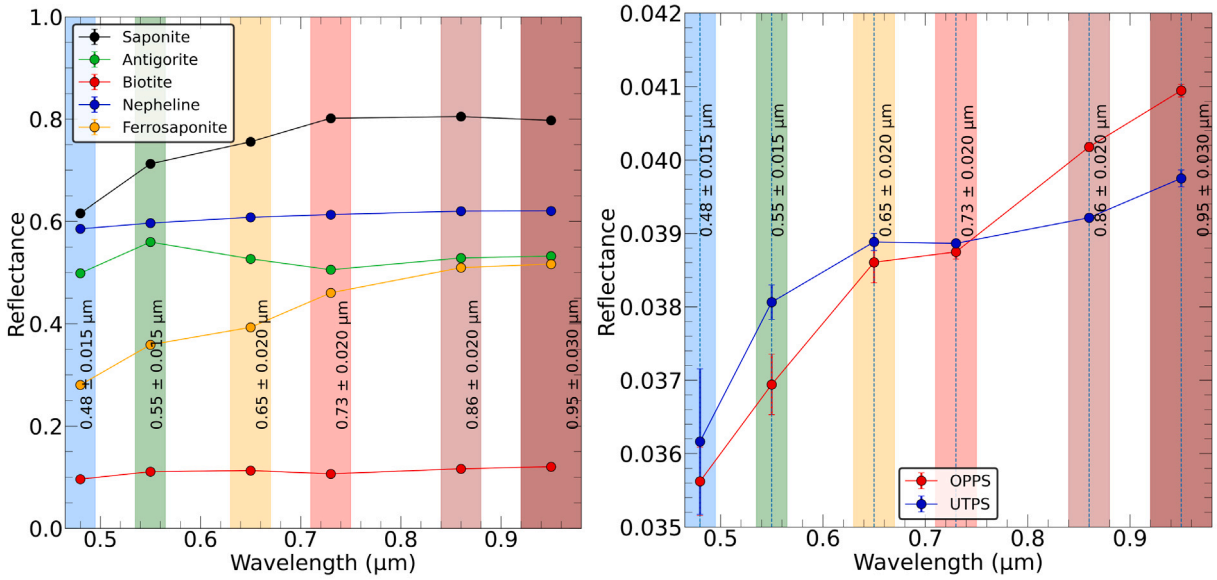

Fig. 16. Converted OROCHI spectra obtained from SHADOWS and SHINE measurements of phyllosilicates (50–100 μm). The OROCHI spectra were obtained assuming rectangular filters. The ferrosaponite (0–125 μm) spectrum was obtained from the RELAB database.

Phobos' origins and in particular, within the giant impact scenario, the C–H stretching modes of aliphatic and aromatic groups will be absent or only due to exogenous contribution (De Sanctis et al., 2019).

While the 30 vol.% case of DECS-19 (i.e., ~18 wt% of aliphatic and aromatic carbon) represents an extreme case with a deep organic band depth; values of 5 to 20 vol.% appear to be quite realistic, with band depth values consistent with previous remote-sensing observations of organic-rich small bodies and with Ryugu sample band depth measurements by MicrOmega (Pilorget et al., 2021). Direct measurements on Ryugu samples shows a organic content around 5% (Quirico et al., 2023; Stroud et al., 2024). These results could help in understanding the organic content of Phobos materials from remote sensing measurements prior to sample return.

Hydrated minerals 2.7 μm signature are particularly persistent in the near-infrared. A very small quantity in a mixture with others silicates and/or opaque materials can make appear the feature (Poggiali et al., 2022, 2023). If present, a 2.7 μm O–H band depth from few percents to almost 40% can be expected (Takir et al., 2019; Pilorget et al., 2021) in the MIRS wavelength range considering a plausible quantity of phyllosilicate as expected in the case of the captured asteroid hypothesis. According to Fraeman et al. (2014), the possible 2.7 μm feature detected in CRISM data would have a band depth between 1 and 10%, depending on the observed Phobos region. The 2.7 μm band for 1 vol.% of phyllosilicates (i.e., 0.24 wt% OH groups) is still slightly visible but it is included in the noise. Hence, detectability for 1 vol.% of phyllosilicates (band depth ~3%) will be more challenging. For 3 vol.% of hydrated minerals (i.e., 0.73 wt% OH groups), the feature is already intense and reach a detectable band depth of 7%. If present, this O–H feature will be detected by the MIRS spectrometer unambiguously for the first time observing without gaps in the spectral range 0.9–3.6 μm, achieving the best spectral resolution for Phobos observations so far (Barucci et al., 2021).

However, it is also interesting to note that phyllosilicate signatures including the 2.7 μm absorption band can be altered by space weathering processes (Noguchi et al., 2023; Le Pivert-Jolivet et al., 2023; Matsuoka et al., 2023). It has been shown that remote sensing observation of Ryugu from Hayabusa2 shows a two times shallower 2.7 μm band depth compared to measurement on the returned sample (Pilorget et al., 2021). The discrepancy is attributed to the fact that orbital observations only look at the uppermost layer of the surface, whereas the sample collected during the mission includes material from the subsurface layer that may have undergone limited or no alteration by space weathering processes. It is important to consider that this effect may not be systematic and could be challenging to quantify on other bodies. However, it is important to bear this in mind when comparing orbital data with laboratory data.

The detectability of both organics and hydrated minerals could strongly depend on several parameters including grain size, relative grain size between the endmembers, porosity, mixing, and composition. Therefore, the detectability limits derived from this work are not an absolute result but give indications for the future observations of the Phobos surface. This will be particularly helpful to interpret the remote-sensing observations of MIRS and quantify the Phobos surface composition before the analysis of the sample return scheduled in 2031. It is also of note that observations with a large phase angle result in a reduction in the band depth (Section 3.6.1). To avoid a reduction in the band contrast and therefore of the band depth, it is recommended that MIRS observations avoid excessive phase angles.

As demonstrated in this study, obtaining measurements at various geometries can also provide valuable additional information about the surface. However, the exact interpretation can be debated as models have difficulties explaining all physical effects that occur in complex environments such as planetary regolith. Measuring the BRDF of return samples from Ryugu, Bennu, and/or Phobos could be an interesting endeavor. This would enable a comparison of BRDF measurements in both laboratory and remote-sensing contexts from the same body, providing a better understanding of laboratory experiment results.

4.3.2. TENGOO/OROCHI

Considering the wavelength range of the measurements performed on our dataset, our results can be useful not only for interpretation of MIRS data but also in support for the OROCHI observations. The 390 nm filter is unfortunately not cover by our measurements. For the other filters, we converted our spectra in OROCHI spectrum by considering rectangular filters (S. Kameda, personal communication).

Fraeman et al. (2014) found a possible 0.65 μm feature possibly linked to the presence of Fe-bearing phyllosilicate in the red unit. This band has been recently confirmed by the analysis of the NOMAD data (Mason et al., 2023). OROCHI will investigate this broad and shallow feature. Our spectra (Fig. 16(a)) show that saponite is the only

phyllosilicate of this study that exhibits such feature. Despite this band being really reduced because of a poor iron saponite, it is still visible and we computed a band depth (using a continuum defined as a straight line between the points at 0.55 μm and 0.73 μm) of ~1%. To compare with a Fe-rich phyllosilicate, we used a ferrosaponite (0–125 μm) spectrum of the RELAB database (id:c1jb762a). As expected, the band depth is more important in this case (~5%). However, when looking at the OROCHI OPPS resampled spectrum (Fig. 16(b)) the 0.65 μm absorption band is not visible and probably removed by the opaques. This implies that, to have a visible 0.65 μm band, the Phobos surface should contains Fe-phyllosilicate particularly rich in Fe, and probably associated to less opaque materials than the OPPS. The CRISM data analyzed by Fraeman et al. (2014) reveal 0.65 μm-band depths between 0.5 and 5%. Therefore, if the feature is detectable by OROCHI, it may implies that the investigated part of the surface is particularly rich (and possibly >40%–50%) in iron-bearing phyllosilicate such as ferrosaponite. In this case, such an observation would favor the formation of Phobos and Deimos by a giant impact. Others minerals could play a role in this feature such as nontronite or cronstedtite (Fraeman et al., 2014), but the band might be due to nanophase iron particles (Fraeman et al., 2014). Such iron particles can be created by space weathering process (Pieters et al., 2000) such as ion irradiation (Hapke, 2001; Brunetto and Strazzulla, 2005) or temperature alteration (Lasue et al., 2022).

The OROCHI spectra will also allow to observe the visible spectral slope of Phobos. In particular, the data at 0.48 μm and 0.86 μm will be used for this purpose. The UTPS shows a spectral slope (0.48–0.86 μm) of 2.22 ± 0.06%/100 nm, whereas the OPPS exhibits a higher slope of 3.37 ± 0.05%/100 nm. The visible slope obtained from OROCHI observations could provide additional information that may aid in the interpretation of Phobos' composition.

5. Conclusion

We presented an experimental work on Phobos simulants. This work was, first, dedicated to a development of a Phobos simulant, for laboratory studies of physical change of the surface and for evaluation of organics and hydrated minerals detectability. This experimental study of a Phobos simulant led to several main results:

- According to spectral slope, reflectance in the VNIR and to positions of the Christiansen features, the reststrahlen band, and the transparency feature in the mid-infrared, a mixture of different (OPPS) endmembers composed of silicates, organics, and opaque materials, was found to be consistent with the Phobos spectra. One of the best match was obtained with a mixture made of olivine (20 vol.%, 50–100 μm), anthracite (20 vol.%, <1 μm), the DECS-19 coal (20 vol.%, 50–100 μm), and saponite (40 vol.%, 50–100 μm).
- We studied the detectability of CH-rich organic that could be found on Phobos in the case of captured asteroid hypothesis. MIRS will allow for the first time to observe Phobos in the CH stretching mode regions, characteristic of organic compounds usually found on small bodies. In this context, we have explored the feasibility of CH-rich organic detection in a Phobos simulant mostly composed of silicates and coal. Our results show that organics are detectable for 5.4 wt% of CH_x in the simulant. If Phobos is indeed linked to a D-type captured asteroid, organic matter is expected (Jones et al., 1990; Brown, 2016; Barucci et al., 2018). However, detectability will be probably strongly dependent on the composition of dark materials, grain size, organic source, etc. A definitive conclusion about the detectability is challenging, but anyway these bands at 3.4 μm are weak and it will be necessary to maximize the chances of seeing it with MIRS by observing Phobos at a low phase angle and with a maximum exposure time in order to increase the S/N.
- We also investigated the detectability of hydrated minerals. Up to now, the 2.7 μm O–H feature was not unambiguously detected on Phobos, but, if present, MIRS will be able to detect this feature. Using the same Phobos simulant of the organic study, we investigated the detectability of this absorption band. Our results show that the 2.7 μm O–H feature is intense and will be probably detectable for MIRS for more than 0.24 wt% of OH groups of the phyllosilicates. These quantities of hydrated minerals could be expected on Phobos (Rivkin et al., 2002; Fraeman et al., 2014; Takir et al., 2019).
- Our work shows that the inversion of the Hapke equation is a strenuous task as the parameters are correlated. Using Monte-Carlo Markov Chain bayesian inference, we were able to explore the parameters space and obtained the best-fit parameters of the experimental data. Some parameters may be difficult to constrain with laboratory data (B_0, h_{sh}, and θ), while other parameters can be determined unambiguously (ω, b, c). The SSA of the Phobos simulants falls within the same range as that of some carbonaceous chondrites, such as Tagish Lake and Allende. The opposition effect of the simulants seems to be higher than that of any other meteorites used for comparison.

This work was made in the context of the MMX mission and of the future MIRS observation of the martians moons. It aimed at better understanding spectro-photometric properties of Phobos laboratory simulants for the interpretation of the MIRS and TENGOO/OROCHI data. In the next papers, we will try to explore, in laboratory using the Phobos simulants, different effects that are present or occur on a surface of an airless body such as Phobos. In particular, porosity/roughness at the micro- and macro-scale, and space weathering are of interest for the surface of small bodies because spectroscopic and photometric remote sensing observations are affected by these parameters. However, these effects are non-exhaustive and further investigations could be dedicated to the study of other samples, e.g. more linked to a basaltic mars composition. We believe that the study of variation of geometry effects such as phase reddening and phase curve variations for different types of surfaces may be useful for other spectro-photometric observations of small bodies.

CRediT authorship contribution statement

Antonin Wargnier: Writing – original draft, Resources, Methodology, Investigation, Formal analysis, Data curation, Conceptualization. **Thomas Gautier:** Writing – review & editing, Validation, Supervision, Resources, Methodology, Funding acquisition, Conceptualization. **Alain Doressoundiram:** Writing – review & editing, Project administration, Conceptualization. **Giovanni Poggiali:** Writing – review & editing, Validation, Resources, Methodology, Conceptualization. **Pierre Beck:** Writing – review & editing, Resources, Investigation, Conceptualization. **Olivier Poch:** Writing – review & editing, Investigation, Data curation. **Eric Quirico:** Writing – review & editing, Investigation. **Tomoki Nakamura:** Writing – review & editing, Conceptualization. **Hideaki Miyamoto:** Writing – review & editing, Resources. **Shingo Kameda:** Writing – review & editing, Resources. **Pedro H. Hasselmann:** Writing – review & editing, Formal analysis. **Nathalie Ruscassier:** Writing – review & editing, Investigation. **Arnaud Buch:** Writing – review & editing, Resources. **Sonia Fornasier:** Writing – review & editing. **Maria Antonietta Barucci:** Writing – review & editing.

Declaration of competing interest

The authors declare that they have no known competing financial interests or personal relationships that could have appeared to influence the work reported in this paper.

Table A.1
End members' characteristics and properties.

Compound	Grain size	Density (g cm^{-3})	Density references	Origins
Nesosilicates				
Olivine (Mg-rich)	50–100 μm	~3.3	Sultana et al. (2023)	Donghai Pellocci Crystal Products
Phyllosilicates				
Biotite	50–100 μm	~2.8	Kremer pigmente	Canada
Antigorite	50–100 μm	~2.6	Anthony (1990)	Haute-Garonne (France)
Saponite SapCa-2	50–100 μm	~2.3	Anthony (1990)	California (USA)
Feldspathoid				
Nepheline (eleolite)	50–100 μm	~2.6	Anthony (1990)	Brevig (Norway)
Organic compounds				
Titan tholins (95% N_2:5% CH_4)	~400 nm	~1	Carrasco et al. (2009)	LATMOS (PAMPRE)
DECS-19	50–100 μm	1.75	Vinogradoff et al. (2021)	Penn State Coal Sample Bank
Opaque materials				
Anthracite	<1 μm	1.62	Sultana et al. (2023)	La Mûre museum (France)

Data and materials availability

All spectroscopic data are available for further studies on the SSHADE database: (1) VNIR data (doi: https://doi.org/10.26302/SSHADE/EXPERIMENT_LB_20240713_001), (2) MIR data (doi: https://doi.org/10.26302/SSHADE/EXPERIMENT_OP_20240717_001), (3) BRDF data (doi: https://doi.org/10.26302/SSHADE/EXPERIMENT_OP_20240717_002). Data are also available in the Zenodo repository (doi: https://dx.doi.org/10.5281/zenodo.11087841). Some OPPS simulant may remain at LESIA and can be shared on reasonable request to the corresponding author.

Acknowledgments

This work was carried out in support for the MIRS instrument onboard the future MMX mission, with the financial support of the Centre National d'Etudes Spatiales, France (CNES). T.G and A.W thank the support from Agence National de la Recherche, France under the grant ANR-20-CE49-0004-01. We gratefully acknowledge iUMTEK for the LIBS analysis of the biotite sample. A. W. thanks Jamila El Bekri (LGPM) for technical support during the preparation of the samples and Cyril Breton (LGPM) for the measurements of grain size by laser diffraction method. We thank also Olivier Brissaud (IPAG) for the help with the SHADOWS and SHINE instruments. We are grateful to the La Mûre Museum (France) and the Université Grenoble Alpes (UGA, France) for donating the anthracite sample. We also acknowledge the Muséum National d'Histoire Naturelle (MNHN, France) for providing us antigorite (12 M.) and nepheline (MNHN-MIN-2011-4569) samples. This research utilizes a ferrosaponite (0–125 μm) spectrum acquired by Janice L. Bishop (id:c1jb762a) with the NASA RELAB facility at Brown University. We thank the two anonymous reviewers for the precious comments and suggestions that contributed to improve the manuscript.

Appendix A. Samples characterization: SEM images, EDX, and grain size distribution

The following presents the results of the sample characterization performed, including SEM images of the mixtures and individual components (Fig. A.1), grain size distribution (Fig. A.2), characteristics of the endmembers (Table A.1), EDX elementary analysis (Table A.3), and bulk chemical composition of the OPPS simulant (Table A.2).

Appendix B. Comparison of the different Hapke's inversion methods

This appendix presents the results of the various inversion methods of the Hapke equation explored in this study. The values of each parameter for each method and for UTPS and OPPS simulants are shown in Table B.1.

Table A.2
Elemental composition of the OPPS given by EDX analysis. Minor elements (<0.1%) and light elements are not reported.

Elements	Atomic (%)
C	39.4
Na	2.2
Mg	24.9
Al	2.3
Si	24.9
K	0.1
Ca	4.7
Fe	1.5

Table A.3
EDX analysis of principal endmembers used in this work.

Minerals	Elements	Atomic (%)	Weight (%)
Antigorite	Mg	19.5	23.2
	Si	15.8	21.7
	Fe	2.3	6.2
Augite	Na	1.2	1.3
	Mg	8.1	9.2
	Al	4.4	5.5
	Si	19.2	25.1
	Ca	5.6	10.4
	Ti	0.1	0.2
	Fe	1.4	3.6
Biotite	Na	0.7	0.7
	Mg	8.7	9.1
	Al	5.7	6.6
	Si	16.9	20.5
	K	4.8	8.1
	Ti	0.7	1.5
	Fe	5.9	14.2
Nepheline	Na	8.7	9.7
	Al	12.9	16.8
	Si	17.2	23.4
	K	2.1	4.0
Olivine	Mg	26.3	30.3
	Si	14.8	19.6
	Fe	3.0	7.7
Saponite	Na	1.8	2.1
	Mg	10.8	13.2
	Al	1.8	2.4
	Si	15.1	21.1
	Ca	3.8	7.7
	K	0.1	0.3

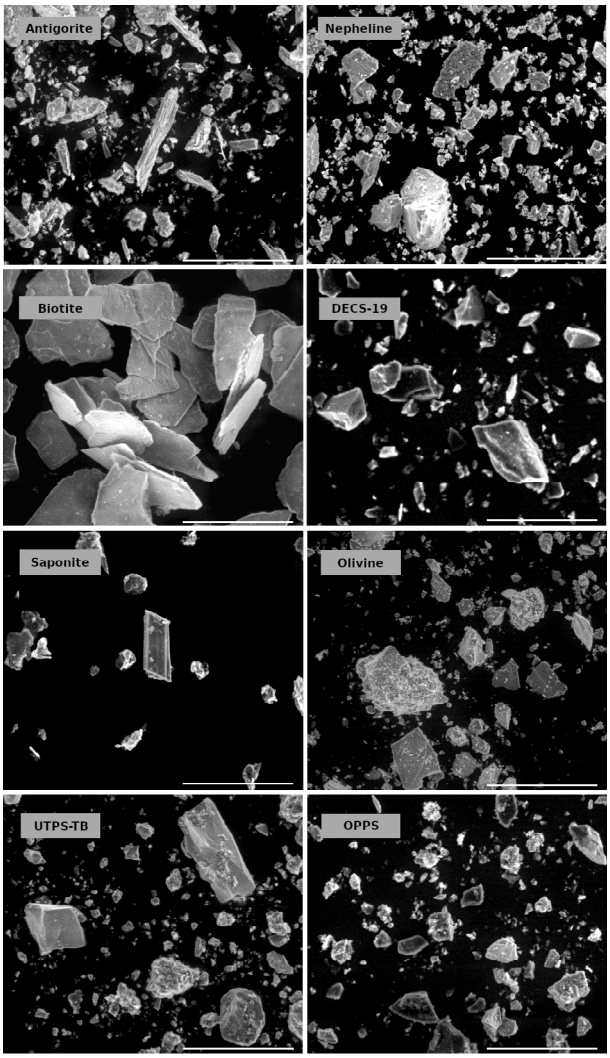

Fig. A.1. SEM images of some endmembers and of the two Phobos simulants used in this work. Note that the scale bar is the same for all SEM images and represents 100 μm.

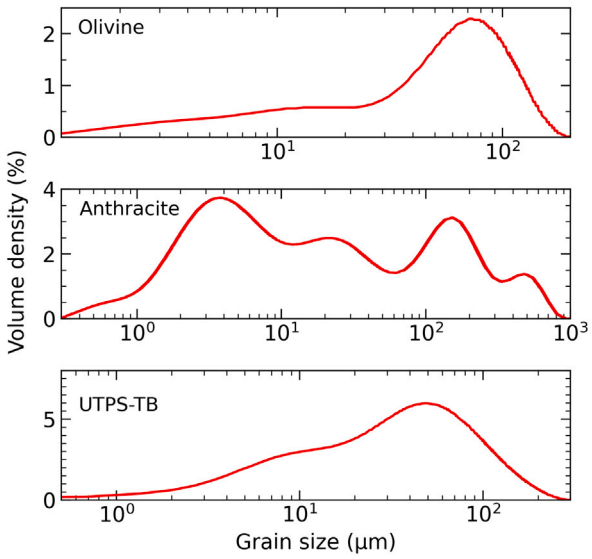

Fig. A.2. Granulometry of some samples used in this study from laser diffraction measurements.

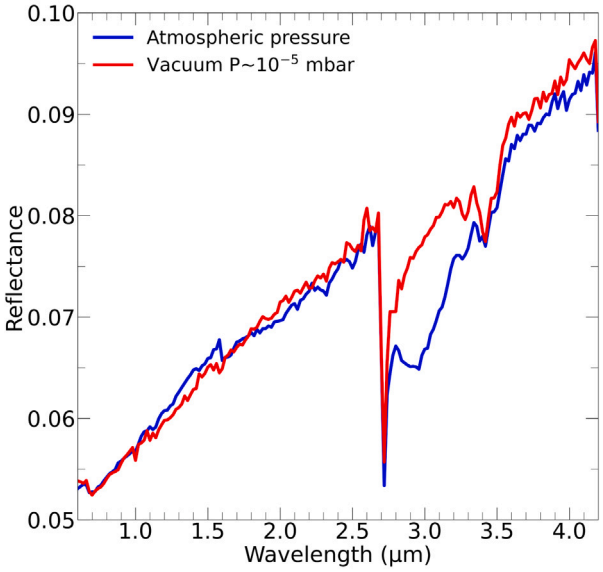

Fig. C.1. Comparison of two measurements made on the same sample (here, SIM-ATG-BIO-2) in vacuum (P~10^{-5} mbar) and at atmospheric pressure. It shows that the 3 μm band for this sample is almost only linked to the adsorbed atmospheric water trap in the mixture powder.

Appendix C. Vacuum effect for measurements

Vacuum measurements require the presence of a window at the top of the chamber. Measurements in different observation geometries cannot be performed in vacuum because the presence of a window could affect the results with refraction and multiple reflection. However, we evaluated the spectroscopic effect of vacuum by measuring some samples at i = 0° and e = 30° in the principal plane. Fig. C.1 shows a comparison between measurements taken at atmospheric pressure and at a pressure of 10^{-5} mbar. We observed a complete removal of the 3 μm feature.

Table B.1
Comparison of the best-fit Hapke parameters obtained after the various inversion methods investigated. The CBOE effect was not considered. The italic values indicated that the parameters is at one of the bounds set for the inversion.

Methods	Sample	w	b	c	$B_{sh,0}$	h_{sh}	$\bar{\theta}$	RMS
LM	UTPS	0.47 ± 0.02	0.80 ± 0.05	−0.98 ± 0.01	*3.0 ± 2.3*	*0.15 ± 0.21*	*11 ± 29*	0.0095
	OPPS	0.23 ± 0.15	0.46 ± 0.17	−0.70 ± 0.33	*3.0 ± 3.3*	0.036 ± 0.17	*11 ± 19*	0.0109
Basin-hopping	UTPS	0.41 ± 0.04	0.85 ± 0.04	−0.995 ± 0.003	*3.0 ± 0.01*	0.28 ± 0.18	*11 ± 0.01*	0.0095
	OPPS	0.23 ± 0.05	0.46 ± 0.08	−0.71 ± 0.14	*3.0 ± 0.01*	0.036 ± 0.04	*11 ± 0.01*	0.0109
MCMC	UTPS	$0.44^{+0.03}_{-0.06}$	$0.74^{+0.07}_{-0.12}$	$-0.97^{+0.04}_{-0.02}$	$2.00^{+0.72}_{-1.06}$	$0.06^{+0.05}_{-0.04}$	$15.46^{+2.29}_{-1.15}$	0.0101
	OPPS	$0.23^{+0.06}_{-0.04}$	$0.49^{+0.11}_{-0.09}$	$-0.71^{+0.17}_{-0.13}$	$2.06^{+0.67}_{-1.01}$	$0.06^{+0.05}_{-0.03}$	$13.18^{+2.86}_{-1.72}$	0.0126

References

Alexander, C.M.O.D., Cody, G.D., De Gregorio, B.T., Nittler, L.R., Stroud, R.M., 2017. The nature, origin and modification of insoluble organic matter in chondrites, the major source of Earth's C and N. Chemie Erde / Geochem. 77 (2), 227–256. http://dx.doi.org/10.1016/j.chemer.2017.01.007.

Anthony, J., 1990. Handbook of Mineralogy. In: Handbook of Mineralogy, Mineral Data Pub., URL: https://books.google.fr/books?id=PEsSAQAAIAAJ.

Bardyn, A., Baklouti, D., Cottin, H., Fray, N., Briois, C., Paquette, J., Stenzel, O., Engrand, C., Fischer, H., Hornung, K., Isnard, R., Langevin, Y., Lehto, H., Le Roy, L., Ligier, N., Merouane, S., Modica, P., Orthous-Daunay, F.-R., Rynö, J., Schulz, R., Silén, J., Thirkell, L., Varmuza, K., Zaprudin, B., Kissel, J., Hilchenbach, M., 2017. Carbon-rich dust in comet 67P/Churyumov-Gerasimenko measured by COSIMA/Rosetta. Mon. Not. R. Astron. Soc. 469, S712–S722. http://dx.doi.org/10.1093/mnras/stx2640.

Barucci, M.A., Perna, D., Popescu, M., Fornasier, S., Doressoundiram, A., Lantz, C., Merlin, F., Fulchignoni, M., Dotto, E., Kanuchova, S., 2018. Small D-type asteroids in the NEO population: new targets for space missions. Mon. Not. R. Astron. Soc. 476 (4), 4481–4487. http://dx.doi.org/10.1093/mnras/sty532.

Barucci, M.A., Reess, J.-M., Bernardi, P., Doressoundiram, A., Fornasier, S., Le Du, M., Iwata, T., Nakagawa, H., Nakamura, T., André, Y., Aoki, S., Arai, T., Baldit, E., Beck, P., Buey, J.-T., Canalias, E., Castelnau, M., Charnoz, S., Chaussidon, M., Chapron, F., Ciarletti, V., Delbo, M., Dubois, B., Gauffre, S., Gautier, T., Genda, H., Hassen-Khodja, R., Hervet, G., Hyodo, R., Imbert, C., Imamura, T., Jorda, L., Kameda, S., Kouach, D., Kouyama, T., Kuroda, T., Kurokawa, H., Lapaw, L., Lasue, J., Le Deit, L., Ledot, A., Leyrat, C., Le Ruyet, B., Matsuoka, M., Merlin, F., Miyamoto, H., Moynier, F., Nguyen Tuong, N., Ogohara, K., Osawa, T., Parisot, J., Pistre, L., Quertier, B., Raymond, S.N., Rocard, F., Sakanoi, T., Sato, T.M., Sawyer, E., Tache, F., Trémolières, S., Tsuchiya, F., Vernazza, P., Zeganadin, D., 2021. MIRS: an imaging spectrometer for the MMX mission. Earth Planets Space 73 (1), 211. http://dx.doi.org/10.1186/s40623-021-01423-2.

Beck, P., Pommerol, A., Thomas, N., Schmitt, B., Moynier, F., Barrat, J.-A., 2012. Photometry of meteorites. Icarus 218 (1), 364–377. http://dx.doi.org/10.1016/j.icarus.2011.12.005.

Brissaud, O., Schmitt, B., Bonnefoy, N., Douté, S., Rabou, P., Grundy, W., Fily, M., 2004. Spectrogonio radiometer for the study of the bidirectional reflectance and polarization functions of planetary surfaces. 1. Design and tests. Appl. Opt. 43 (9), 1926–1937. http://dx.doi.org/10.1364/AO.43.001926.

Brown, M.E., 2016. The 3–4 μm spectra of jupiter trojan asteroids. Astron. J. 152 (6), 159. http://dx.doi.org/10.3847/0004-6256/152/6/159, arXiv:1606.03013.

Brunetto, R., Lantz, C., Nakamura, T., Baklouti, D., Le Pivert-Jolivet, T., Kobayashi, S., Borondics, F., 2020. Characterizing irradiated surfaces using IR spectroscopy. Icarus 345, 113722. http://dx.doi.org/10.1016/j.icarus.2020.113722.

Brunetto, R., Strazzulla, G., 2005. Elastic collisions in ion irradiation experiments: A mechanism for space weathering of silicates. Icarus 179 (1), 265–273. http://dx.doi.org/10.1016/j.icarus.2005.07.001.

Burke, K.N., DellaGiustina, D.N., Bennett, C.A., Walsh, K.J., Pajola, M., Bierhaus, E.B., Nolan, M.C., Boynton, W.V., Brodbeck, J.I., Connolly, Jr., H.C., Deshapriya, J.D.P., Dworkin, J.P., Elder, C.M., Golish, D.R., Hoover, R.H., Jawin, E.R., McCoy, T.J., Michel, P., Molaro, J.L., Nolau, J.O., Padilla, J., Rizk, B., Robbins, S.J., Sahr, E.M., Smith, P.H., Stewart, S.J., Susorney, H.C.M., Enos, H.L., Lauretta, D.S., 2021. Particle size-frequency distributions of the OSIRIS-REx candidate sample sites on asteroid (101955) bennu. Remote Sens. 13 (7), 1315. http://dx.doi.org/10.3390/rs13071315.

Carrasco, N., Schmitz-Afonso, I., Bonnet, J.-Y., Quirico, E., Thissen, R., Dutuit, O., Bagag, A., Laprévote, O., Buch, A., Giulani, A., Adandé, G., Ouni, F., Hadamcik, E., Szopa, C., Cernogora, G., 2009. Chemical characterization of titan's tholins: Solubility, morphology and molecular structure revisited. J. Phys. Chem. A 113 (42), 11195–11203. http://dx.doi.org/10.1021/jp904735q.

Choukroun, M., Altwegg, K., Kührt, E., Biver, N., Bockelée-Morvan, D., Drążkowska, J., Hérique, A., Hilchenbach, M., Marschall, R., Pätzold, M., Taylor, M.G.G.T., Thomas, N., 2020. Dust-to-gas and refractory-to-ice mass ratios of comet 67p/churyumov-gerasimenko from rosetta observations. Space Sci. Rev. 216 (3), 44. http://dx.doi.org/10.1007/s11214-020-00662-1.

Clark, B.E., Helfenstein, P., Bell, J.F., Peterson, C., Veverka, J., Izenberg, N.I., Domingue, D., Wellnitz, D., McFadden, L., 2002. NEAR infrared spectrometer photometry of asteroid 433 eros. Icarus 155 (1), 189–204. http://dx.doi.org/10.1006/icar.2001.6748.

Clark, R.N., Roush, T.L., 1984. Reflectance spectroscopy: quantitative analysis techniques for remotesensing applications. J. Geophys. Res. 89, 6329–6340. http://dx.doi.org/10.1029/JB089iB07p06329.

Cloutis, E.A., Gaffey, M.J., Smith, D.G.W., Lambert, R.S.J., 1990. Reflectance spectra of mafic silicate-opaque assemblages with applications to meteorite spectra. Icarus 84 (2), 315–333. http://dx.doi.org/10.1016/0019-1035(90)90041-7.

Cloutis, E.A., Hardersen, P.S., Reddy, V., Gaffey, M.J., Bailey, D.T., Craig, M.A., 2009. Metal-orthopyroxene and metal-olivine mixtures: Spectral reflectance properties and implications for asteroid spectroscopy. In: 40th Annual Lunar and Planetary Science Conference. In: Lunar and Planetary Science Conference, p. 1332.

Cloutis, E.A., Hudon, P., Hiroi, T., Gaffey, M.J., 2012a. Spectral reflectance properties of carbonaceous chondrites: 3. CR chondrites. Icarus 217 (1), 389–407. http://dx.doi.org/10.1016/j.icarus.2011.11.004.

Cloutis, E.A., Hudon, P., Hiroi, T., Gaffey, M.J., 2012b. Spectral reflectance properties of carbonaceous chondrites 4: Aqueously altered and thermally metamorphosed meteorites. Icarus 220 (2), 586–617. http://dx.doi.org/10.1016/j.icarus.2012.05.018.

Cooper, B.L., Salisbury, J.W., Killen, R.M., Potter, A.E., 2002. Midinfrared spectral features of rocks and their powders. J. Geophys. Res. (Planets) 107 (E4), 5017. http://dx.doi.org/10.1029/2000JE001462.

Craddock, R.A., 1994. The origin of PHOBOS and deimos. In: Lunar and Planetary Science Conference. In: Lunar and Planetary Science Conference, p. 293.

Craddock, R.A., 2011. Are Phobos and Deimos the result of a giant impact? Icarus 211 (2), 1150–1161. http://dx.doi.org/10.1016/j.icarus.2010.10.023.

Cuadros, J., Mavris, C., Michalski, J.R., 2022. Possible widespread occurrence of vermiculite on mars. Appl. Clay Sci. 228, 106643. http://dx.doi.org/10.1016/j.clay.2022.106643, URL: https://www.sciencedirect.com/science/article/pii/S0169131722002381.

De Sanctis, M.C., Ammannito, E., McSween, H.Y., Raponi, A., Marchi, S., Capaccioni, F., Capria, M.T., Carrozzo, F.G., Ciarniello, M., Fonte, S., Formisano, M., Frigeri, A., Giardino, M., Longobardo, A., Magni, G., McFadden, L.A., Palomba, E., Pieters, C.M., Tosi, F., Zambon, F., Raymond, C.A., Russell, C.T., 2017. Localized aliphatic organic material on the surface of Ceres. Science 355 (6326), 719–722. http://dx.doi.org/10.1126/science.aaj2305.

De Sanctis, M.C., Vinogradoff, V., Raponi, A., Ammannito, E., Ciarniello, M., Carrozzo, F.G., De Angelis, S., Raymond, C.A., Russell, C.T., 2019. Characteristics of organic matter on Ceres from VIR/Dawn high spatial resolution spectra. Mon. Not. R. Astron. Soc. 482 (2), 2407–2421. http://dx.doi.org/10.1093/mnras/sty2772.

Dellagiustina, D.N., Emery, J.P., Golish, D.R., Rozitis, B., Bennett, C.A., Burke, K.N., Ballouz, R.-L., Becker, K.J., Christensen, P.R., Drouet D'Aubigny, C.Y., Hamilton, V.E., Reuter, D.C., Rizk, B., Simon, A.A., Asphaug, E., Bandfield, J.L., Barnouin, O.S., Barucci, M.A., Bierhaus, E.B., Binzel, R.P., Bottke, W.F., Bowles, N.E., Campins, H., Clark, B.C., Clark, B.E., Connolly, H.C., Daly, M.G., Leon, J.D., Delbo', M., Deshapriya, J.D.P., Elder, C.M., Fornasier, S., Hergenrother, C.W., Howell, E.S., Jawin, E.R., Kaplan, H.H., Kareta, T.R., Le Corre, L., Li, J.-Y., Licandro, J., Lim, L.F., Michel, P., Molaro, J., Nolan, M.C., Pajola, M., Popescu, M., Garcia, J.L.R., Ryan, A., Schwartz, S.R., Shultz, N., Siegler, M.A., Smith, P.H., Tatsumi, E., Thomas, C.A., Walsh, K.J., Wolner, C.W.V., Zou, X.-D., Lauretta, D.S., Osiris-Rex Team, 2019. Properties of rubble-pile asteroid (101955) Bennu from OSIRIS-REx imaging and thermal analysis. Nat. Astron. 3, 341–351. http://dx.doi.org/10.1038/s41550-019-0731-1.

DeMeo, F.E., Binzel, R.P., Slivan, S.M., Bus, S.J., 2009. An extension of the Bus asteroid taxonomy into the near-infrared. Icarus 202 (1), 160–180. http://dx.doi.org/10.1016/j.icarus.2009.02.005.

Ellis, B.S., Neukampf, J., Bachmann, O., Harris, C., Forni, F., Magna, T., Laurent, O., Ulmer, P., 2022. Biotite as a recorder of an exsolved Li-rich volatile phase in upper-crustal silicic magma reservoirs. Geology 50 (4), 481–485. http://dx.doi.org/10.1130/G49484.1.

Fernando, J., Schmidt, F., Ceamanos, X., Pinet, P., Douté, S., Daydou, Y., 2013. Surface reflectance of Mars observed by CRISM/MRO: 2. Estimation of surface photometric properties in Gusev Crater and Meridiani Planum. J. Geophys. Res. (Planets) 118 (3), 534–559. http://dx.doi.org/10.1029/2012JE004194, arXiv:1303.4549.

Fletcher, R., 2000. Practical Methods of Optimization. Wiley, http://dx.doi.org/10.1002/9781118723203.

Foreman-Mackey, D., Hogg, D.W., Lang, D., Goodman, J., 2013. emcee: The MCMC hammer. Publ. ASP 125 (925), 306. http://dx.doi.org/10.1086/670067, arXiv:1202.3665.

Fornasier, S., Dotto, E., Hainaut, O., Marzari, F., Boehnhardt, H., De Luise, F., Barucci, M.A., 2007. Visible spectroscopic and photometric survey of Jupiter Trojans: Final results on dynamical families. Icarus 190 (2), 622–642. http://dx.doi.org/10.1016/j.icarus.2007.03.033, arXiv:0704.0350.

Fornasier, S., Hasselmann, P.H., Barucci, M.A., Feller, C., Besse, S., Leyrat, C., Lara, L., Gutierrez, P.J., Oklay, N., Tubiana, C., Scholten, F., Sierks, H., Barbieri, C., Lamy, P.L., Rodrigo, R., Koschny, D., Rickman, H., Keller, H.U., Agarwal, J., A'Hearn, M.F., Bertaux, J.-L., Bertini, I., Cremonese, G., Da Deppo, V., Davidsson, B., Debei, S., De Cecco, M., Fulle, M., Groussin, O., Güttler, C., Hviid, S.F., Ip, W., Jorda, L., Knollenberg, J., Kovacs, G., Kramm, R., Kührt, E., Küppers, M., La Forgia, F., Lazzarin, M., Lopez Moreno, J.J., Marzari, F., Matz, K.-D., Michalik, H., Moreno, F., Mottola, S., Naletto, G., Pajola, M., Pommerol, A., Preusker, F., Shi, X., Snodgrass, C., Thomas, N., Vincent, J.-B., 2015. Spectrophotometric properties of the nucleus of comet 67p/Churyumov–Gerasimenko from the OSIRIS instrument onboard the ROSETTA spacecraft. Astron. Astrophys. 583 (A30).

Fornasier, S., Hasselmann, P.H., Deshapriya, J.D.P., Barucci, M.A., Clark, B.E., Praet, A., Hamilton, V.E., Simon, A., Li, J.-Y., Cloutis, E.A., Merlin, F., Zou, X.-D., Lauretta, D.S., 2020. Phase reddening on asteroid Bennu from visible and near-infrared spectroscopy. Astron. Astrophys. 644, A142. http://dx.doi.org/10.1051/0004-6361/202039552, arXiv:2011.09339.

Fornasier, S., Wargnier, A., Hasselmann, P.H., Matz, K.-D., Tirsch, D., Gautier, T., Doressoundiram, A., Barucci, M.A., 2024. Phobos photometric properties from Mars Express HRSC observations. Astron. Astrophys. 125 (12), e06583. http://dx.doi.org/10.1029/2020JE006583.

Fraeman, A.A., Arvidson, R.E., Murchie, S.L., Rivkin, A., Bibring, J.-P., Choo, T.H., Gondet, B., Humm, D., Kuzmin, R.O., Manaud, N., Zabalueva, E.V., 2012. Analysis of disk-resolved OMEGA and CRISM spectral observations of Phobos and Deimos. J. Geophys. Res. (Planets) 117, E00J15. http://dx.doi.org/10.1029/2012JE004137.

Fraeman, A.A., Murchie, S.L., Arvidson, R.E., Clark, R.N., Morris, R.V., Rivkin, A.S., Vilas, F., 2014. Spectral absorptions on Phobos and Deimos in the visible/near infrared wavelengths and their compositional constraints. Icarus 229, 196–205. http://dx.doi.org/10.1016/j.icarus.2013.11.021.

Giuranna, M., Roush, T.L., Duxbury, T., Hogan, R.C., Carli, C., Geminale, A., Formisano, V., 2011. Compositional interpretation of PFS/MEx and TES/MGS thermal infrared spectra of Phobos. Planet. Space Sci. 59 (13), 1308–1325. http://dx.doi.org/10.1016/j.pss.2011.01.019.

Glotch, T.D., Edwards, C.S., Yesiltas, M., Shirley, K.A., McDougall, D.S., Kling, A.M., Bandfield, J.L., Herd, C.D.K., 2018. MGS-TES spectra suggest a basaltic component in the regolith of Phobos. J. Geophys. Res. (Planets) 123 (10), 2467–2484. http://dx.doi.org/10.1029/2018JE005647.

Gunderson, K., Thomas, N., Whitby, J.A., 2006. First measurements with the physikalisches institut radiometric experiment (PHIRE). Planet. Space Sci. 54 (11), 1046–1056. http://dx.doi.org/10.1016/j.pss.2005.12.020.

Hamilton, V.E., 2000. Thermal infrared emission spectroscopy of the pyroxene mineral series. J. Geophys. Res. 105 (E4), 9701–9716. http://dx.doi.org/10.1029/1999JE001112.

Hamilton, V.E., Keller, L.P., Haenecour, P., Barnes, J.J., Hill, D., Connolly, Jr., H.C., Lauretta, D.S., 2024. Mineralogy of Bennu from spectral analysis of the sample returned by OSIRIS-REx. In: Lunar and Planetary Science Conference. In: Lunar and Planetary Science Conference, p. 2498.

Hamilton, V.E., Simon, A.A., Christensen, P.R., Reuter, D.C., Clark, B.E., Barucci, M.A., Bowles, N.E., Boynton, W.V., Brucato, J.R., Cloutis, E.A., Connolly, H.C., Donaldson Hanna, K.L., Emery, J.P., Enos, H.L., Fornasier, S., Haberle, C.W., Hanna, R.D., Howell, E.S., Kaplan, H.H., Keller, L.P., Lantz, C., Li, J.-Y., Lim, L.F., McCoy, T.J., Merlin, F., Nolan, M.C., Praet, A., Rozitis, B., Sandford, S.A., Schrader, D.L., Thomas, C.A., Zou, X.-D., Lauretta, D.S., Osiris-Rex Team, 2019. Evidence for widespread hydrated minerals on asteroid (101955) Bennu. Nat. Astron. 3, 332–340. http://dx.doi.org/10.1038/s41550-019-0722-2.

Hapke, B., 1981. Bidirectional reflectance spectroscopy. I - Theory. J. Geophys. Res. 86, 3039–3054. http://dx.doi.org/10.1029/JB086iB04p03039.

Hapke, B., 1984. Bidirectional reflectance spectroscopy 3. Correction for macroscopic roughness. Icarus 59 (1), 41–59. http://dx.doi.org/10.1016/0019-1035(84)90054-X.

Hapke, B., 1986. Bidirectional reflectance spectroscopy. 7. The extinction coefficient and the opposition effect. Icarus 67, 264–280.

Hapke, B., 1993. Theory of reflectance and emittance spectroscopy.

Hapke, B., 2001. Space weathering from Mercury to the asteroid belt. J. Geophys. Res. 106 (E5), 10039–10074. http://dx.doi.org/10.1029/2000JE001338.

Hapke, B., 2002. Bidirectional reflectance spectroscopy. 5. The coherent backscatter opposition effect and anisotropic scattering. Icarus 157, 523–534.

Hapke, B., 2008. Bidirectional reflectance spectroscopy. 6. Effects of porosity. Icarus 195, 918–926.

Hapke, B., 2012. Bidirectional reflectance spectroscopy. 7. The single particle phase function hockey stick relation. Icarus 221, 1079–1083.

Hapke, B., 2012. Theory of reflectance and emittance spectroscopy. http://dx.doi.org/10.1017/CBO9781139025683.

Hapke, B., Denevi, B., Sato, H., Braden, S., Robinson, M., 2012. The wavelength dependence of the lunar phase curve as seen by the Lunar Reconnaissance Orbiter wide-angle camera. J. Geophys. Res. (Planets) 117, E00H15. http://dx.doi.org/10.1029/2011JE003916.

Hapke, B., Nelson, R., Smythe, W., 1998. The opposition effect of the moon: Coherent backscatter and shadow hiding. Icarus 133 (1), 89–97. http://dx.doi.org/10.1006/icar.1998.5907.

Hatakeda, K., Yada, T., Abe, M., Okada, T., Nakato, A., Yogata, K., Miyazaki, A., Kumagai, K., Nishimura, M., Hitomi, Y., Soejima, H., Nagashima, K., Yoshitake, M., Iwamae, A., Furuya, S., Usui, T., Kitazato, K., 2023. Homogeneity and heterogeneity in near-infrared FTIR spectra of Ryugu returned samples. Earth Planets Space 75 (1), 46. http://dx.doi.org/10.1186/s40623-023-01784-w.

Helfenstein, P., Shepard, M.K., 2011. Testing the Hapke photometric model: Improved inversion and the porosity correction. Icarus 215 (1), 83–100. http://dx.doi.org/10.1016/j.icarus.2011.07.002.

Helfenstein, P., Veverka, J., 1989. Physical characterization of asteroid surfaces from photometric analysis. In: Binzel, R.P., Gehrels, T., Matthews, M.S. (Eds.), Asteroids II. pp. 557–593.

Helfenstein, P., Veverka, J., Hillier, J., 1997. The lunar opposition effect: A test of alternative models. Icarus 128 (1), 2–14. http://dx.doi.org/10.1006/icar.1997.5726.

Hromakina, T., Barucci, M.A., Belskaya, I., Fornasier, S., Merlin, F., Praet, A., Poggiali, G., Matsuoka, M., 2022. Search for carbon-bearing compounds on low-albedo asteroids. Mon. Not. R. Astron. Soc. 514 (1), 21–33. http://dx.doi.org/10.1093/mnras/stac1338.

Hyodo, R., Genda, H., Charnoz, S., Rosenblatt, P., 2017. On the impact origin of phobos and deimos. I. Thermodynamic and physical aspects. Astrophys. J. 845 (2), 125. http://dx.doi.org/10.3847/1538-4357/aa81c4, arXiv:1707.06282.

Jones, T.D., Lebofsky, L.A., Lewis, J.S., Marley, M.S., 1990. The composition and origin of the C, P, and D asteroids: Water as a tracer of thermal evolution in the outer belt. Icarus 88 (1), 172–192. http://dx.doi.org/10.1016/0019-1035(90)90184-B.

Jost, B., Pommerol, A., Poch, O., Brouet, Y., Fornasier, S., Carrasco, N., Szopa, C., Thomas, N., 2017a. Bidirectional reflectance of laboratory cometary analogues to interpret the spectrophotometric properties of the nucleus of comet 67p/Churyumov–Gerasimenko. Planet. Space Sci. 148, 1–11. http://dx.doi.org/10.1016/j.pss.2017.09.009.

Jost, B., Pommerol, A., Poch, O., Gundlach, B., Leboeuf, M., Dadras, M., Blum, J., Thomas, N., 2016. Experimental characterization of the opposition surge in fine-grained water-ice and high albedo ice analogs. Icarus 264, 109–131. http://dx.doi.org/10.1016/j.icarus.2015.09.020.

Jost, B., Pommerol, A., Poch, O., Yoldi, Z., Fornasier, S., Hasselmann, P.H., Feller, C., Carrasco, N., Szopa, C., Thomas, N., 2017b. Bidirectional reflectance and VIS-NIR spectroscopy of cometary analogues under simulated space conditions. Planet. Space Sci. 145, 14–27. http://dx.doi.org/10.1016/j.pss.2017.07.009.

Kameda, S., Ozaki, M., Enya, K., Fuse, R., Kouyama, T., Sakatani, N., Suzuki, H., Osada, N., Kato, H., Miyamoto, H., Yamazaki, A., Nakamura, T., Okamoto, T., Ishimaru, T., Hong, P., Ishibashi, K., Takashima, T., Ishigami, R., Kuo, C.-L., Abe, S., Goda, Y., Murao, H., Fujishima, S., Aoyama, T., Hagiwara, K., Mizumoto, S., Tanaka, N., Murakami, K., Matsumoto, M., Tanaka, K., Sakuta, H., 2021. Design of telescopic nadir imager for geomorphology (TENGOO) and observation of surface reflectance by optical chromatic imager (OROCHI) for the Martian Moons Exploration (MMX). Earth Planets Space 73 (1), 218. http://dx.doi.org/10.1186/s40623-021-01462-9.

Kaplan, H.H., Milliken, R.E., Alexander, C.M.O., Herd, C.D.K., 2019. Reflectance spectroscopy of insoluble organic matter (IOM) and carbonaceous meteorites. Meteorit. Planet. Sci. 54 (5), 1051–1068. http://dx.doi.org/10.1111/maps.13264.

Kaplan, H.H., Simon, A.A., Hamilton, V.E., Thompson, M.S., Sandford, S.A., Barucci, M.A., Cloutis, E.A., Brucato, J., Reuter, D.C., Glavin, D.P., Clark, B.E., Dworkin, J.P., Campins, H., Emery, J.P., Fornasier, S., Zou, X.D., Lauretta, D.S., 2021. Composition of organics on asteroid (101955) Bennu. Astron. Astrophys. 653, L1. http://dx.doi.org/10.1051/0004-6361/202141167.

Kitazato, K., Clark, B.E., Abe, M., Abe, S., Takagi, Y., Hiroi, T., Barnouin-Jha, O.S., Abell, P.A., Lederer, S.M., Vilas, F., 2008. Near-infrared spectrophotometry of Asteroid 25143 Itokawa from NIRS on the Hayabusa spacecraft. Icarus 194 (1), 137–145. http://dx.doi.org/10.1016/j.icarus.2007.08.029.

Kitazato, K., Milliken, R.E., Iwata, T., Abe, M., Ohtake, M., Matsuura, S., Arai, T., Nakauchi, Y., Nakamura, T., Matsuoka, M., Senshu, H., Hirata, N., Hiroi, T., Pilorget, C., Brunetto, R., Poulet, F., Riu, L., Bibring, J.-P., Takir, D., Domingue, D.L., Vilas, F., Barucci, M.A., Perna, D., Palomba, E., Galiano, A., Tsumura, K., Osawa, T., Komatsu, M., Nakato, A., Arai, T., Takato, N., Matsunaga, T., Takagi, Y., Matsumoto, K., Kouyama, T., Yokota, Y., Tatsumi, E., Sakatani, N., Yamamoto, Y., Okada, T., Sugita, S., Honda, R., Morota, T., Kameda, S., Sawada, H., Honda, C., Yamada, M., Suzuki, H., Yoshioka, K., Hayakawa, M., Ogawa, K., Cho, Y., Shirai, K., Shimaki, Y., Hirata, N., Yamaguchi, A., Ogawa, N., Terui, F., Yamaguchi, T., Takei, Y., Saiki, T., Nakazawa, S., Tanaka, S., Yoshikawa, M., Watanabe, S., Tsuda, Y., 2019. The surface composition of asteroid 162173 Ryugu from Hayabusa2 near-infrared spectroscopy. Science 364 (6437), 272–275. http://dx.doi.org/10.1126/science.aav7432.

Kuehrt, E., Giese, B., Keller, H.U., Ksanfomality, L.V., 1992. Interpretation of the KRFM-infrared measurements of phobos. Icarus 96 (2), 213–218. http://dx.doi.org/10.1016/0019-1035(92)90075-I.

Kuramoto, K., Kawakatsu, Y., Fujimoto, M., Araya, A., Barucci, M.A., Genda, H., Hirata, N., Ikeda, H., Imamura, T., Helbert, J., Kameda, S., Kobayashi, M., Kusano, H., Lawrence, D.J., Matsumoto, K., Michel, P., Miyamoto, H., Morota, T., Nakagawa, H., Nakamura, T., Ogawa, K., Otake, H., Ozaki, M., Russell, S., Sasaki, S., Sawada, H., Senshu, H., Tachibana, S., Terada, N., Ulamec, S., Usui, T., Wada, K., Watanabe, S.-i., Yokota, S., 2022. Martian moons exploration MMX: sample return mission to Phobos elucidating formation processes of habitable planets. Earth Planets Space 74 (1), 12. http://dx.doi.org/10.1186/s40623-021-01545-7.

Landsman, Z.A., Schultz, C.D., Britt, D.T., Peppin, M., Kobrick, R.L., Metzger, P.T., Orlovskaya, N., 2021. Phobos regolith simulants PGI-1 and PCA-1. Adv. Space Res. 67 (10), 3308–3327. http://dx.doi.org/10.1016/j.asr.2021.01.024.

Lasue, J., Pinet, P., Beck, P., Toplis, M., Munsch, P., Oustric, M., 2022. Spectral behavior of regolith analogues weathered by heating under reducing conditions. In: European Planetary Science Congress. EPSC2022–840. http://dx.doi.org/10.5194/epsc2022-840.

Le Pivert-Jolivet, T., Brunetto, R., Pilorget, C., Bibring, J.-P., Nakato, A., Hamm, V., Hatakeda, K., Lantz, C., Loizeau, D., Riu, L., Yogata, K., Baklouti, D., Poulet, F., Aléon-Toppani, A., Carter, J., Langevin, Y., Okada, T., Yada, T., Hitomi, Y., Kumagai, K., Miyazaki, A., Nagashima, K., Nishimura, M., Usui, T., Abe, M., Saiki, T., Tanaka, S., Nakazawa, S., Tsuda, Y., Watanabe, S., 2023. Space weathering record and pristine state of Ryugu samples from MicrOmega spectral analysis. Nat. Astron. 7, 1445–1453. http://dx.doi.org/10.1038/s41550-023-02092-9.

Levenberg, K., 2018. A method for the solution of certain non-linear problems in least squares. Quart. Appl. Math. 2, 164–168. http://dx.doi.org/10.1090/qam/10666.

Li, J.-Y., Helfenstein, P., Buratti, B.J., Takir, D., Clark, B.E., 2015. Asteroid photometry. pp. 129–150,

Liu, W.-P., Yin, W., Ye, B.-L., Zhao, T.-L., Yao, Q.-Z., Li, Y.-L., Fu, S.-Q., Zhou, G.-T., 2023. Reliable spectroscopic identification of minerals associated with serpentinization: Relevance to Mars exploration. Icarus 394, 115440. http://dx.doi.org/10.1016/j.icarus.2023.115440.

Lovering, T.G., 1972. Distribution of Minor Elements in Biotite Samples from Felsic Intrusive Rocks As a Tool for Correlation. Geol. Surv. Bull. 1314-D.

Mandon, L., Beck, P., Quantin-Nataf, C., Dehouck, E., Pommerol, A., Yoldi, Z., Cerubini, R., Pan, L., Martinot, M., Sautter, V., 2021. Martian meteorites reflectance and implications for rover missions. Icarus 366, 114517. http://dx.doi.org/10.1016/j.icarus.2021.114517, arXiv:2203.10051.

Marquardt, D.W., 1963. An algorithm for least-squares estimation of nonlinear parameters. J. Soc. Ind. Appl. Math. 11 (2), 431–441, URL: http://www.jstor.org/stable/2098941.

Martin, A.C., Emery, J.P., Loeffler, M.J., 2022. Spectral effects of regolith porosity in the mid-IR - Forsteritic olivine. Icarus 378, 114921. http://dx.doi.org/10.1016/j.icarus.2022.114921.

Martin, A.C., Emery, J.P., Loeffler, M., Donaldson Hanna, K.L., 2024. Investigation of high porosity regoliths with mid-infrared reflectance and emissivity spectra. In: Lunar and Planetary Science Conference. In: Lunar and Planetary Science Conference, p. 2498.

Mason, J.P., Patel, M.R., Pajola, M., Cloutis, E.D., Alday, J., Olsen, K.S., Marriner, C., Holmes, J.A., Sellers, G., Thomas, N., Almeida, M., Read, M., Nakagawa, H., Thomas, I.R., Ristic, B., Willame, Y., Depiesse, C., Daerden, F., Vandaele, A.C., Lopez-Moreno, J.J., Bellucci, G., 2023. Ultraviolet and visible reflectance spectra of phobos and deimos as measured by the ExoMars-TGO/NOMAD-UVIS spectrometer. J. Geophys. Res.: Planets 128 (12), e2023JE008002. http://dx.doi.org/10.1029/2023JE008002, URL: https://agupubs.onlinelibrary.wiley.com/doi/abs/10.1029/2023JE008002. arXiv:https://agupubs.onlinelibrary.wiley.com/doi/pdf/10.1029/2023JE008002. e2023JE008002 2023JE008002.

Matsuoka, M., Kagawa, E.-i., Amano, K., Nakamura, T., Tatsumi, E., Osawa, T., Hiroi, T., Milliken, R., Domingue, D., Takir, D., Brunetto, R., Barucci, A., Kitazato, K., Sugita, S., Fujioka, Y., Sasaki, O., Kobayashi, S., Iwata, T., Morota, T., Yokota, Y., Kouyama, T., Honda, R., Kameda, S., Cho, Y., Yoshioka, K., Sawada, H., Hayakawa, M., Sakatani, N., Yamada, M., Suzuki, H., Honda, C., Ogawa, K., Shirai, K., Lantz, C., Rubino, S., Yurimoto, H., Noguchi, T., Okazaki, R., Yabuta, H., Naraoka, H., Sakamoto, K., Tachibana, S., Yada, T., Nishimura, M., Nakato, A., Miyazaki, A., Yogata, K., Abe, M., Okada, T., Usui, T., Yoshikawa, M., Saiki, T., Tanaka, S., Terui, F., Nakazawa, S., Watanabe, S.-i., Tsuda, Y., 2023. Space weathering acts strongly on the uppermost surface of Ryugu. Commun. Earth Environ. 4 (1), 335. http://dx.doi.org/10.1038/s43247-023-00991-3.

McGuire, A.F., Hapke, B.W., 1995. An experimental study of light scattering by large, irregular particles. Icarus 113 (1), 134–155. http://dx.doi.org/10.1006/icar.1995.1012.

McLennan, S.M., Anderson, R.B., Bell, J.F., Bridges, J.C., Calef, F., Campbell, J.L., Clark, B.C., Clegg, S., Conrad, P., Cousin, A., Des Marais, D.J., Dromart, G., Dyar, M.D., Edgar, L.A., Ehlmann, B.L., Fabre, C., Forni, O., Gasnault, O., Gellert, R., Gordon, S., Grant, J.A., Grotzinger, J.P., Gupta, S., Herkenhoff, K.E., Hurowitz, J.A., King, P.L., Le Mouélic, S., Leshin, L.A., Léveillé, R., Lewis, K.W., Mangold, N., Maurice, S., Ming, D.W., Morris, R.V., Nachon, M., Newsom, H.E., Ollila, A.M., Perrett, G.M., Rice, M.S., Schmidt, M.E., Schwenzer, S.P., Stack, K., Stolper, E.M., Sumner, D.Y., Treiman, A.H., VanBommel, S., Vaniman, D.T., Vasavada, A., Wiens, R.C., Yingst, R.A., Kemppinen, O., Bridges, N., Johnson, J.R., Minitti, M., Cremers, D., Farmer, J., Godber, A., Wadhwa, M., Wellington, D., McEwan, I., Newman, C., Richardson, M., Charpentier, A., Peret, L., Blank, J., Weigle, G., Li, S., Milliken, R., Robertson, K., Sun, V., Baker, M., Edwards, C., Farley, K., Griffes, J., Miller, H., Newcombe, M., Pilorget, C., Siebach, K., Brunet, C., Hipkin, V., Marchand, G., Sánchez, P.S., Favot, L., Cody, G., Steele, A., Flückiger, L., Lees, D., Nefian, A., Martin, M., Gailhanou, M., Westall, F., Israël, G., Agard, C., Baroukh, J., Donny, C., Gaboriaud, A., Guillemot, P., Lafaille, V., Lorigny, E., Paillet, A., Pérez, M., Yana, C., Armiens-Aparicio, C., Rodríguez, J.C., Blázquez, I.C., Gómez, F.G., Gómez-Elvira, J., Hettrich, S., Malvitte, A.L., Jiménez, M.M., Martínez-Frías, J., Martín-Soler, J., Martín-Torres, F.J., Jurado, A.M., Mora-Sotomayor, L., Caro, G.M., López, S.N., Peinado-González, V., Pla-García, J., Manfredi, J.A.R., Romeral-Planelló, S.A.S., Martinez, E.S., Redondo, J.T., Urqui-O'Callaghan, R., Mier, M.-P.Z., Chipera, S., Lacour, J.-L., Mauchien, P., Sirven, J.-B., Manning, H., Fairén, A., Hayes, A., Joseph, J., Squyres, S., Sullivan, R., Thomas, P., Dupont, A., Lundberg, A., Melikechi, N., Mezzacappa, A., DeMarines, J., Grinspoon, D., Reitz, G., Prats, B., Atlaskin, E., Genzer, M., Harri, A.-M., Haukka, H., Kahanpää, H., Kauhanen, J., Kemppinen, O., Paton, M., Polkko, J., Schmidt, W., Siili, T., Wray, J., Wilhelm, M.B., Poitrasson, F., Patel, K., Gorevan, S., Indyk, S., Paulsen, G., Bish, D., Schieber, J., Gondet, B., Langevin, Y., Geffroy, C., Baratoux, D., Berger, G., Cros, A., d'Uston, C., Lasue, J., Lee, Q.-M., Meslin, P.-Y., Pallier, E., Parot, Y., Pinet, P., Schröder, S., Toplis, M., Lewin, É., Brunner, W., Heydari, E., Achilles, C., Oehler, D., Sutter, B., Cabane, M., Coscia, D., Israël, G., Szopa, C., Robert, F., Sautter, V., Buch, A., Stalport, F., Coll, P., François, P., Raulin, F., Teinturier, S., Cameron, J., DeLapp, D., Dingler, R., Jackson, R.S., Johnstone, S., Lanza, N., Little, C., Nelson, T., Williams, R.B., Jones, A., Kirkland, L., Baker, B., Cantor, B., Caplinger, M., Davis, S., Duston, B., Edgett, K., Fay, D., Hardgrove, C., Harker, D., Herrera, P., Jensen, E., Kennedy, M.R., Krezoski, G., Krysak, D., Lipkaman, L., Malin, M., McCartney, E., McNair, S., Nixon, B., Posiolova, L., Ravine, M., Salamon, A., Saper, L., Stoiber, K., Supulver, K., Van Beek, J., Van Beek, T., Zimdar, R., French, K.L., Iagnemma, K., Miller, K., Summons, R., Goesmann, F., Goetz, W., Hviid, S., Johnson, M., Lefavor, M., Lyness, E., Breves, E., Fassett, C., Blake, D.F., Bristow, T., Edwards, L., Haberle, R., Hoehler, T., Hollingsworth, J., Kahre, M., Keely, L., McKay, C., Wilhelm, M.B., Bleacher, L., Brinckerhoff, W., Choi, D., Dworkin, J.P., Eigenbrode, J., Floyd, M., Freissinet, C., Garvin, J., Glavin, D., Harpold, D., Jones, A., Mahaffy, P., Martin, D.K., McAdam, A., Pavlov, A., Raaen, E., Smith, M.D., Stern, J., Tan, F., Trainer, M., Meyer, M., Posner, A., Voytek, M., Anderson, R.C., Aubrey, A., Beegle, L.W., Behar, A., Blaney, D., Brinza, D., Christensen, L., Crisp, J.A., DeFlores, L., Ehlmann, B., Feldman, J., Feldman, S., Flesch, G., Jun, I., Keymeulen, D., Maki, J., Mischna, M., Morookian, J.M., Parker, T., Pavri, B., Schoppers, M., Sengstacken, A., Simmonds, J.J., Spanovich, N., Juarez, M.d.l.T., Webster, C.R., Yen, A., Archer, P.D., Cucinotta, F., Jones, J.H., Niles, P., Rampe, E., Nolan, T., Fisk, M., Radziemski, L., Barraclough, B., Bender, S., Berman, D., Dobrea, E.N., Tokar, R., Williams, R.M.E., Cleghorn, T., Huntress, W., Manhès, G., Hudgins, J., Olson, T., Stewart, N., Sarrazin, P., Vicenzi, E., Wilson, S.A., Bullock, M., Ehresmann, B., Hamilton, V., Hassler, D., Peterson, J., Rafkin, S., Zeitlin, C., Fedosov, F., Golovin, D., Karpushkina, N., Kozyrev, A., Litvak, M., Malakhov, A., Mitrofanov, I., Mokrousov, M., Nikiforov, S., Prokhorov, V., Sanin, A., Tretyakov, V., Varenikov, A., Vostrukhin, A., Kuzmin, R., Wolff, M., Botta, O., Drake, D., Bean, K., Lemmon, M., Lee, E.M., Sucharski, R., Hernández, M.Á.d., Ávalos, J.J.B., Ramos, M., Kim, M.-H., Malespin, C., Plante, I., Muller, J.-P., Navarro-González, R., Ewing, R., Boynton, W., Downs, R., Fitzgibbon, M., Harshman, K., Morrison, S., Dietrich, W., Kortmann, O., Palucis, M., Williams, A., Lugmair, G., Wilson, M.A., Rubin, D., Jakosky, B., Balic-Zunic, T., Frydenvang, J., Jensen, J.K.v., Kinch, K., Koefoed, A., Madsen, M.B., Stipp, S.L.S., Boyd, N., Pradler, I., Jacob, S., Owen, T., Rowland, S., Atlaskin, E., Savijärvi, H., Boehm, E., Böttcher, S., Burmeister, S., Guo, J., Köhler, J., García, C.M., Mueller-Mellin, R., Wimmer-Schweingruber, R., McConnochie, T., Benna, M., Franz, H., Bower, H., Brunner, A., Blau, H., Boucher, T., Carmosino, M., Atreya, S., Elliott, H., Halleaux, D., Rennó, N., Wong, M., Pepin, R., Elliott, B., Spray, J., Thompson, L., Williams, J., Vasconcelos, P., Bentz, J., Nealson, K., Popa, R., Kah, L.C., Moersch, J., Tate, C., Day, M., Kocurek, G., Hallet, B., Sletten, R., Francis, R., McCullough, E., Cloutis, E., ten Kate, I.L., Kuzmin, R., Arvidson, R., Fraeman, A., Scholes, D., Slavney, S., Stein, T., Ward, J., Berger, J., Moores, J.E., 2014. Elemental geochemistry of sedimentary rocks at Yellowknife Bay, Gale Crater, Mars. Science 343 (6169), 1244734. http://dx.doi.org/10.1126/science.1244734.

McMillan, N.J., Harmon, R.S., De Lucia, F.C., Miziolek, A.M., 2007. Laser-induced breakdown spectroscopy analysis of minerals: Carbonates and silicates. Spectrochim. Acta 62 (12), 1528–1536. http://dx.doi.org/10.1016/j.sab.2007.10.037.

Michikami, T., Honda, C., Miyamoto, H., Hirabayashi, M., Hagermann, A., Irie, T., Nomura, K., Ernst, C.M., Kawamura, M., Sugimoto, K., Tatsumi, E., Morota, T., Hirata, N., Noguchi, T., Cho, Y., Kameda, S., Kouyama, T., Yokota, Y., Noguchi, R., Hayakawa, M., Hirata, N., Honda, R., Matsuoka, M., Sakatani, N., Suzuki, H., Yamada, M., Yoshioka, K., Sawada, H., Hemmi, R., Kikuchi, H., Ogawa, K., Watanabe, S.-i., Tanaka, S., Yoshikawa, M., Tsuda, Y., Sugita, S., 2019. Boulder size and shape distributions on asteroid Ryugu. Icarus 331, 179–191. http://dx.doi.org/10.1016/j.icarus.2019.05.019.

Miyamoto, H., Niihara, T., Wada, K., Ogawa, K., Senshu, H., Michel, P., Kikuchi, H., Hemmi, R., Nakamura, T., Nakamura, A.M., Hirata, N., Sasaki, S., Asphaug, E., Britt, D.T., Abell, P.A., Ballouz, R.-L., Banouin, O.S., Baresi, N., Barucci, M.A., Biele, J., Grott, M., Hino, H., Hong, P.K., Imada, T., Kameda, S., Kobayashi, M., Libourel, G., Mogi, K., Murdoch, N., Nishio, Y., Okamoto, S., Ota, Y., Otsuki, M., Otto, K.A., Sakatani, N., Shimizu, Y., Takemura, T., Terada, N., Tsukamoto, M., Usui, T., Willner, K., 2021. Surface environment of Phobos and Phobos simulant UTPS. Earth Planets Space 73 (1), 214. http://dx.doi.org/10.1186/s40623-021-01406-3.

Morlok, A., Klemme, S., Weber, I., Stojic, A., Sohn, M., Hiesinger, H., Helbert, J., 2019. Mid-infrared spectroscopy of planetary analogs: A database for planetary remote sensing. Icarus 324, 86–103. http://dx.doi.org/10.1016/j.icarus.2019.02.010, arXiv:2302.09987.

Morlok, A., Renggli, C., Charlier, B., Namur, O., Klemme, S., Reitze, M.P., Weber, I., Stojic, A.N., Bauch, K.E., Hiesinger, H., Helbert, J., 2023. A mid-infrared study of

synthetic glass and crystal mixtures analog to the geochemical terranes on mercury. Icarus 396, 115498. http://dx.doi.org/10.1016/j.icarus.2023.115498.

Moroz, L.V., Arnold, G., Korochantsev, A.V., Wäsch, R., 1998. Natural solid bitumens as possible analogs for cometary and asteroid organics:. 1. Reflectance spectroscopy of pure bitumens. Icarus 134 (2), 253–268. http://dx.doi.org/10.1006/icar.1998.5955.

Murchie, S.L., Britt, D.T., Head, J.W., Pratt, S.F., Fisher, P.C., Zhukov, B.S., Kuzmin, A.A., Ksanfomality, L.V., Zharkov, A.V., Nikitin, G.E., Fanale, F.P., Blaney, D.L., Bell, J.F., Robinson, M.S., 1991. Color heterogeneity of the surface of phobos: Relationships to geological features and comparison to meteorites analogs. J. Geophys. Res. 96 (B4), 5295–5945.

Murchie, S., Erard, S., 1996. Spectral properties and heterogeneity of phobos from measurements by phobos 2. Icarus 123, 63–86.

Mustard, J.F., Glotch, T.D., 2019. Theory of reflectance and emittance spectroscopy of geologic materials in the visible and infrared regions. In: Bishop, J.L., Bell, J.F., Moersch, J.E. (Eds.), Remote Compositional Analysis: Techniques for Understanding Spectroscopy, Mineralogy, and Geochemistry of Planetary Surfaces. pp. 21–41. http://dx.doi.org/10.1017/9781316888872.004.

Mustard, J.F., Hays, J.E., 1997. Effects of hyperfine particles on reflectance spectra from 0.3 to 25 μm. Icarus 125 (1), 145–163. http://dx.doi.org/10.1006/icar.1996.5583.

Nakamura, T., Matsumoto, M., Amano, K., Enokido, Y., Zolensky, M.E., Mikouchi, T., Genda, H., Tanaka, S., Zolotov, M.Y., Kurosawa, K., Wakita, S., Hyodo, R., Nagano, H., Nakashima, D., Takahashi, Y., Fujioka, Y., Kikuiri, M., Kagawa, E., Matsuoka, M., Brearley, A.J., Tsuchiyama, A., Uesugi, M., Matsuno, J., Kimura, Y., Sato, M., Milliken, R.E., Tatsumi, E., Sugita, S., Hiroi, T., Kitazato, K., Brownlee, D., Joswiak, D.J., Takahashi, M., Ninomiya, K., Takahashi, T., Osawa, T., Terada, K., Brenker, F.E., Tkalcec, B.J., Vincze, L., Brunetto, R., Aléon-Toppani, A., Chan, Q.H.S., Roskosz, M., Viennet, J.-C., Beck, P., Alp, E.E., Michikami, T., Nagaashi, Y., Tsuji, T., Ino, Y., Martinez, J., Han, J., Dolocan, A., Bodnar, R.J., Tanaka, M., Yoshida, H., Sugiyama, K., King, A.J., Fukushi, K., Suga, H., Yamashita, S., Kawai, T., Inoue, K., Nakato, A., Noguchi, T., Vilas, F., Hendrix, A.R., Jaramillo-Correa, C., Domingue, D.L., Dominguez, G., Gainsforth, Z., Engrand, C., Duprat, J., Russell, S.S., Bonato, E., Ma, C., Kawamoto, T., Wada, T., Watanabe, S., Endo, R., Enju, S., Riu, L., Rubino, S., Tack, P., Takeshita, S., Takeichi, Y., Takeuchi, A., Takigawa, A., Takir, D., Tanigaki, T., Taniguchi, A., Tsukamoto, K., Yagi, T., Yamada, S., Yamamoto, K., Yamashita, Y., Yasutake, M., Uesugi, K., Umegaki, I., Chiu, I., Ishizaki, T., Okumura, S., Palomba, E., Pilorget, C., Potin, S.M., Alasli, A., Anada, S., Araki, Y., Sakatani, N., Schultz, C., Sekizawa, O., Sitzman, S.D., Sugiura, K., Sun, M., Dartois, E., De Pauw, E., Dionnet, Z., Djouadi, Z., Falkenberg, G., Fujita, R., Fukuma, T., Gearba, I.R., Hagiya, K., Hu, M.Y., Kato, T., Kawamura, T., Kimura, M., Kubo, M.K., Langenhorst, F., Lantz, C., Lavina, B., Lindner, M., Zhao, J., Vekemans, B., Baklouti, D., Bazi, B., Borondics, F., Nagasawa, S., Nishiyama, G., Nitta, K., Mathurin, J., Matsumoto, T., Mitsukawa, I., Miura, H., Miyake, A., Miyake, Y., Yurimoto, H., Okazaki, R., Yabuta, H., Naraoka, H., Sakamoto, K., Tachibana, S., Connolly, H.C., Lauretta, D.S., Yoshitake, M., Yoshikawa, M., Yoshikawa, K., Yoshihara, K., Yokota, Y., Yogata, K., Yano, H., Yamamoto, Y., Yamamoto, D., Yamada, M., Yamada, T., Yada, T., Wada, K., Usui, T., Tsukizaki, R., Terui, F., Takeuchi, H., Takei, Y., Iwamae, A., Soejima, H., Shirai, K., Shimaki, Y., Senshu, H., Sawada, H., Saiki, T., Ozaki, M., Ono, G., Okada, T., Ogawa, N., Ogawa, K., Noguchi, R., Noda, H., Nishimura, M., Namiki, N., Nakazawa, S., Morota, T., Miyazaki, A., Miura, A., Mimasu, Y., Matsumoto, K., Kumagai, K., Kouyama, T., Kikuchi, S., Kawahara, K., Kameda, S., Iwata, T., Ishihara, Y., Ishiguro, M., Ikeda, H., Hosoda, S., Honda, R., Honda, C., Hitomi, Y., Hirata, N., Hirata, N., Hayashi, T., Hayakawa, M., Hatakeda, K., Furuya, S., Fukai, R., Fujii, A., Cho, Y., Arakawa, M., Abe, M., Watanabe, S., Tsuda, Y., 2023. Formation and evolution of carbonaceous asteroid Ryugu: Direct evidence from returned samples. Science 379 (6634), abn8671. http://dx.doi.org/10.1126/science.abn8671.

Nakato, A., Yada, T., Nishimura, M., Yogata, K., Miyazaki, A., Nagashima, K., Hatakeda, K., Kumagai, K., Hitomi, Y., Soejima, H., Bibring, J.-P., Pilorget, C., Hamm, V., Brunetto, R., Riu, L., Lourit, L., Loizeau, D., Le Pivert-Jolivet, T., Lequertier, G., Moussi-Soffys, A., Abe, M., Okada, T., Usui, T., Nakazawa, S., Saiki, T., Tanaka, S., Terui, F., Yoshikawa, M., Watanabe, S.-i., Tsuda, Y., 2023. Variations of the surface characteristics of Ryugu returned samples. Earth Planets Space 75 (1), 45. http://dx.doi.org/10.1186/s40623-022-01754-8.

Nelson, R., Hapke, B., Smythe, W., Spilker, L., 2000. The opposition effect in simulated planetary regoliths. Reflectance and circular polarization ratio change at small phase angle. Icarus 147 (2), 545–558. http://dx.doi.org/10.1006/icar.2000.6454, URL: https://www.sciencedirect.com/science/article/pii/S0019103500964546.

Newville, M., Stensitzki, T., Allen, D.B., Ingargiola, A., 2015. LMFIT: Non-linear least-square minimization and curve-fitting for python. http://dx.doi.org/10.5281/zenodo.11813.

Noguchi, T., Matsumoto, T., Miyake, A., Igami, Y., Haruta, M., Saito, H., Hata, S., Seto, Y., Miyahara, M., Tomioka, N., Ishii, H.A., Bradley, J.P., Ohtaki, K.K., Dobrică, E., Leroux, H., Le Guillou, C., Jacob, D., de la Peña, F., Laforet, S., Marinova, M., Langenhorst, F., Harries, D., Beck, P., Phan, T.H.V., Rebois, R., Abreu, N.M., Gray, J., Zega, T., Zanetta, P.-M., Thompson, M.S., Stroud, R., Burgess, K., Cymes, B.A., Bridges, J.C., Hicks, L., Lee, M.R., Daly, L., Bland, P.A., Zolensky, M.E., Frank, D.R., Martinez, J., Tsuchiyama, A., Yasutake, M., Matsuno, J., Okumura, S., Mitsukawa, I., Uesugi, K., Uesugi, M., Takeuchi, A., Sun, M., Enju, S., Takigawa, A., Michikami, T., Nakamura, T., Matsumoto, M., Nakauchi, Y., Abe, M., Arakawa, M., Fujii, A., Hayakawa, M., Hirata, N., Hirata, N., Honda, R., Honda, C., Hosoda, S., Iijima, Y.-i., Ikeda, H., Ishiguro, M., Ishihara, Y., Iwata, T., Kawahara, K., Kikuchi, S., Kitazato, K., Matsumoto, K., Matsuoka, M., Mimasu, Y., Miura, A., Morota, T., Nakazawa, S., Namiki, N., Noda, H., Noguchi, R., Ogawa, N., Ogawa, K., Okada, T., Okamoto, C., Ono, G., Ozaki, M., Saiki, T., Sakatani, N., Sawada, H., Senshu, H., Shimaki, Y., Shirai, K., Sugita, S., Takei, Y., Takeuchi, H., Tanaka, S., Tatsumi, E., Terui, F., Tsukizaki, R., Wada, K., Yamada, M., Yamada, T., Yamamoto, Y., Yano, H., Yokota, Y., Yoshihara, K., Yoshikawa, M., Yoshikawa, K., Fukai, R., Furuya, S., Hatakeda, K., Hayashi, T., Hitomi, Y., Kumagai, K., Miyazaki, A., Nakato, A., Nishimura, M., Soejima, H., Suzuki, A.I., Usui, T., Yada, T., Yamamoto, D., Yogata, K., Yoshitake, M., Connolly, H.C., Lauretta, D.S., Yurimoto, H., Nagashima, K., Kawasaki, N., Sakamoto, N., Okazaki, R., Yabuta, H., Naraoka, H., Sakamoto, K., Tachibana, S., Watanabe, S.-i., Tsuda, Y., 2023. A dehydrated space-weathered skin cloaking the hydrated interior of Ryugu. Nat. Astron. 7, 170–181. http://dx.doi.org/10.1038/s41550-022-01841-6.

Ogawa, K., Sakatani, N., Kadono, T., Arakawa, M., Honda, R., Wada, K., Shirai, K., Shimaki, Y., Ishibashi, K., Yokota, Y., Saiki, T., Imamura, H., Tsuda, Y., Nakazawa, S., Takagi, Y., Hayakawa, M., Yano, H., Okamoto, C., Iijima, Y., Morota, T., Kameda, S., Tatsumi, E., Cho, Y., Yoshioka, K., Sawada, H., Matsuoka, M., Yamada, M., Kouyama, T., Suzuki, H., Honda, C., Sugita, S., 2022. Particle size distributions inside and around the artificial crater produced by the Hayabusa2 impact experiment on Ryugu. Earth Planets Space 74 (1), 153. http://dx.doi.org/10.1186/s40623-022-01713-3.

Orthous-Daunay, F.-R., Quirico, E., Beck, P., Brissaud, O., Dartois, E., Pino, T., Schmitt, B., 2013. Mid-infrared study of the molecular structure variability of insoluble organic matter from primitive chondrites. Icarus 223 (1), 534–543. http://dx.doi.org/10.1016/j.icarus.2013.01.003.

Pajola, M., Lazzarin, M., Berini, I., Marzari, F., Turrini, D., Magrin, S., La Forgia, F., Thomas, N., Küppers, M., Moissl, R., Ferri, F., Barbieri, C., Rickman, H., Sierks, H., the OSIRIS Team, 2012. Spectrophotometric investigation of Phobos with the Rosetta OSIRIS-NAC camera and implications for its collisional capture. Mon. Not. R. Astron. Soc. 427, 3230–3243.

Pajola, M., Lazzarin, M., Dalle Ore, C.M., Cruikshank, D.P., Roush, T.L., Magrin, S., Bertini, I., La Forgia, F., Barbieri, C., 2013. Phobos as a D-type captured asteroid, spectral modeling from 0.25 to 4.0 μm. Astrophys. J. 777 (2), 127. http://dx.doi.org/10.1088/0004-637X/777/2/127.

Pajola, M., Roush, T., Dalle Ore, C., Marzo, G.A., Simioni, E., 2018. Phobos MRO/CRISM visible and near-infrared (0.5–2.5 μm) spectral modeling. Planet. Space Sci. 154, 63–71.

Pang, K.D., Pollack, J.B., Veverka, J., Lane, A.L., Ajello, J.M., 1978. The composition of Phobos: Evidence for carbonaceous chondrite surface from spectral analysis. Science 199, 64–66.

Pieters, C.M., Taylor, L.A., Noble, S.K., Keller, L.P., Hapke, B., Morris, R.V., Allen, C.C., McKay, D.S., Wentworth, S., 2000. Space weathering on airless bodies: Resolving a mystery with lunar samples. Meteorit. Planet. Sci. 35 (5), 1101–1107. http://dx.doi.org/10.1111/j.1945-5100.2000.tb01496.x.

Pignatale, F.C., Charnoz, S., Rosenblatt, P., Hyodo, R., Nakamura, T., Genda, H., 2018. On the impact origin of Phobos and Deimos. III. Resulting composition from different impactors. Astrophys. J. 853 (2), 118. http://dx.doi.org/10.3847/1538-4357/aaa23e, arXiv:1712.05154.

Pilorget, C., Okada, T., Hamm, V., Brunetto, R., Yada, T., Loizeau, D., Riu, L., Usui, T., Moussi-Soffys, A., Hatakeda, K., Nakato, A., Yogata, K., Abe, M., Aléon-Toppani, A., Carter, J., Chaigneau, M., Crane, B., Gondet, B., Kumagai, K., Langevin, Y., Lantz, C., Le Pivert-Jolivet, T., Lequertier, G., Lourit, L., Miyazaki, A., Nishimura, M., Poulet, F., Arakawa, M., Hirata, N., Kitazato, K., Nakazawa, S., Namiki, N., Saiki, T., Sugita, S., Tachibana, S., Tanaka, S., Yoshikawa, M., Tsuda, Y., Watanabe, S., Bibring, J.-P., 2021. First compositional analysis of Ryugu samples by the MicrOmega hyperspectral microscope. Nat. Astron. 6, 221–225. http://dx.doi.org/10.1038/s41550-021-01549-z.

Pisello, A., Ferrari, M., De Angelis, S., Vetere, F.P., Porreca, M., Stefani, S., Perugini, D., 2022. Reflectance of silicate glasses in the mid-infrared region (MIR): Implications for planetary research. Icarus 388, 115222. http://dx.doi.org/10.1016/j.icarus.2022.115222.

Poggiali, G., Iannini Lelarge, S., Brucato, J.R., Barucci, M.A., Masotta, M., Corazzi, M.A., Fornaro, T., Brown, A.J., Mandon, L., Randazzo, N., 2023. Laboratory measurements of anhydrous minerals mixed with hyperfine hydrated minerals to support interpretation of infrared reflectance observations of planetary surfaces. Icarus 394, 115449. http://dx.doi.org/10.1016/j.icarus.2023.115449.

Poggiali, G., Matsuoka, M., Barucci, M.A., Brucato, J.R., Beck, P., Fornasier, S., Doressoundiram, A., Merlin, F., Alberini, A., 2022. Phobos and Deimos surface composition: search for spectroscopic analogues. Mon. Not. R. Astron. Soc. 516 (1), 465–476. http://dx.doi.org/10.1093/mnras/stac2226.

Pommerol, A., Schmitt, B., 2008. Strength of the H_2O near-infrared absorption bands in hydrated minerals: Effects of measurement geometry. J. Geophys. Res. (Planets) 113 (E12), E12008. http://dx.doi.org/10.1029/2008JE003197.

Pommerol, A., Thomas, N., Jost, B., Beck, P., Okubo, C., McEwen, A.S., 2013. Photometric properties of Mars soils analogs. J. Geophys. Res. (Planets) 118 (10), 2045–2072. http://dx.doi.org/10.1002/jgre.20158.

Potin, S., Beck, P., Schmitt, B., Moynier, F., 2019. Some things special about NEAs: Geometric and environmental effects on the optical signatures of hydration. Icarus 333, 415–428. http://dx.doi.org/10.1016/j.icarus.2019.06.026, arXiv:1907.01783.

Potin, S., Brissaud, O., Beck, P., Schmitt, B., Magnard, Y., Correia, J.-J., Rabou, P., Jocou, L., 2018. SHADOWS: a spectro-gonio radiometer for bidirectional reflectance studies of dark meteorites and terrestrial analogs: design, calibrations, and performances on challenging surfaces. Appl. Opt. 57 (28), 8279. http://dx.doi.org/10.1364/AO.57.008279, arXiv:2002.04606.

Potin, S.M., Douté, S., Kugler, B., Forbes, F., 2022. The impact of asteroid shapes and topographies on their reflectance spectroscopy. Icarus 376, 114806. http://dx.doi.org/10.1016/j.icarus.2021.114806, arXiv:2111.11290.

Quirico, E., Bonal, L., Kebukawa, Y., Amano, K., Yabuta, H., Phan, V.T.H., Beck, P., Rémusat, L., Dartois, E., Engrand, C., Martins, Z., Bejach, L., Dazzi, A., Deniset-Besseau, A., Duprat, J., Mathurin, J., Montagnac, G., Barosch, J., Cody, G.D., De Gregorio, B., Enokido, Y., Hashiguchi, M., Kamide, K., Kilcoyne, D., Komatsu, M., Matsumoto, M., Mostefaoui, S., Nittler, L., Ohigashi, T., Okumura, T., Sandford, S., Shigenaka, M., Stroud, R., Suga, H., Takahashi, Y., Takeichi, Y., Tamenori, Y., Verdier-Paoletti, M., Wakabayashi, D., Yamashita, S., Nakamura, T., Naraoka, H., Noguchi, T., Okazaki, R., Yurimoto, H., Sakamoto, K., Tachibana, S., Watanabe, S.-I., Tsuda, Y., Yada, T., Nishimura, M., Nakato, A., Miyazaki, A., Yogata, K., Abe, M., Okada, T., Usui, T., Yoshikawa, M., Saiki, T., Tanaka, S., Terui, F., Nakazawa, S., 2023. Compositional heterogeneity of insoluble organic matter extracted from asteroid Ryugu samples. Meteorit. Planet. Sci. http://dx.doi.org/10.1111/maps.14097, arXiv:https://onlinelibrary.wiley.com/doi/pdf/10.1111/maps.14097. URL: https://onlinelibrary.wiley.com/doi/abs/10.1111/maps.14097.

Quirico, E., Montagnac, G., Rouzaud, J.-N., Bonal, L., Bourot-Denise, M., Duber, S., Reynard, B., 2009. Precursor and metamorphic condition effects on Raman spectra of poorly ordered carbonaceous matter in chondrites and coals. Earth Planet. Sci. Lett. 287 (1–2), 185–193. http://dx.doi.org/10.1016/j.epsl.2009.07.041.

Quirico, E., Moroz, L.V., Schmitt, B., Arnold, G., Faure, M., Beck, P., Bonal, L., Ciarniello, M., Capaccioni, F., Filacchione, G., Erard, S., Leyrat, C., Bockelée-Morvan, D., Zinzi, A., Palomba, E., Drossart, P., Tosi, F., Capria, M.T., De Sanctis, M.C., Raponi, A., Fonti, S., Mancarella, F., Orofino, V., Barucci, A., Blecka, M.I., Carlson, R., Despan, D., Faure, A., Fornasier, S., Gudipati, M.S., Longobardo, A., Markus, K., Mennella, V., Merlin, F., Piccioni, G., Rousseau, B., Taylor, F., 2016. Refractory and semi-volatile organics at the surface of comet 67P/Churyumov-Gerasimenko: Insights from the VIRTIS/Rosetta imaging spectrometer. Icarus 272, 32–47. http://dx.doi.org/10.1016/j.icarus.2016.02.028.

Raponi, A., Ciarniello, M., Capaccioni, F., Mennella, V., Filacchione, G., Vinogradoff, V., Poch, O., Beck, P., Quirico, E., De Sanctis, M.C., Moroz, L.V., Kappel, D., Erard, S., Bockelée-Morvan, D., Longobardo, A., Tosi, F., Palomba, E., Combe, J.-P., Rousseau, B., Arnold, G., Carlson, R.W., Pommerol, A., Pilorget, C., Fornasier, S., Bellucci, G., Barucci, A., Mancarella, F., Formisano, M., Rinaldi, G., Istiqomah, I., Leyrat, C., 2020. Infrared detection of aliphatic organics on a cometary nucleus. Nat. Astron. 4, 500–505. http://dx.doi.org/10.1038/s41550-019-0992-8, arXiv:2009.14476.

Redin, Y., Redina, A., Malyutina, A., Dultsev, V., Kalinin, Y., Abramov, B., Borisenko, A., 2023. Distinctive features of the major and trace element composition of Biotite from igneous rocks associated with various types of mineralization on the example of the shakhtama intrusive complex (eastern transbaikalia). Minerals 13 (10), 1334. http://dx.doi.org/10.3390/min13101334.

Rickman, D., Patel, M.R., Pearson, V.K., Wilson, S., Edmunson, J., 2016. A carbonaceous chondrite based simulant of Phobos. In: Earth and Space 2016. pp. 576–583. http://dx.doi.org/10.1061/9780784479971.054. arXiv:https://ascelibrary.org/doi/pdf/10.1061/9780784479971.054. URL: https://ascelibrary.org/doi/abs/10.1061/9780784479971.054.

Rivkin, A.S., Brown, R.H., Trilling, D.E., Bell, J.F., Plassmann, J.H., 2002. Near-infrared spectrophotometry of Phobos and Deimos. Icarus 156 (1), 64–75. http://dx.doi.org/10.1006/icar.2001.6767.

Rivkin, A.S., Emery, J.P., Howell, E.S., Kareta, T., Noonan, J.W., Richardson, M., Sharkey, B.N.L., Sickafoose, A.A., Woodney, L.M., Cartwright, R.J., Lindsay, S., Mcclure, L.T., 2022. The nature of low-albedo small bodies from 3 μm spectroscopy: One group that formed within the ammonia snow line and one that formed beyond it. Planet. Sci. J. 3 (7), 153. http://dx.doi.org/10.3847/PSJ/ac7217, arXiv:2205.09166.

Ronnet, T., Vernazza, P., Mousis, O., Brugger, B., Beck, P., Devouard, B., Witasse, O., Cipriani, F., 2016. Reconciling the orbital and physical properties of the martian moons. Astrophys. J. 828 (2), 109. http://dx.doi.org/10.3847/0004-637X/828/2/109, arXiv:1607.02350.

Rosenblatt, P., 2011. The origins of the Martian moons revisited. Astron. Astrophys. 19, 44. http://dx.doi.org/10.1007/s00159-011-0044-6.

Rubin, A.E., 1997. Mineralogy of meteorite groups. Meteorit. Planet. Sci. 32, 231–247. http://dx.doi.org/10.1111/j.1945-5100.1997.tb01262.x.

Salisbury, J.W., D'Aria, D.M., Jarosewich, E., 1991. Midinfrared (2.5-13.5 μm) reflectance spectra of powdered stony meteorites. Icarus 92 (2), 280–297. http://dx.doi.org/10.1016/0019-1035(91)90052-U.

Salisbury, J.W., Wald, A., D'Aria, D.M., 1994. Thermal-infrared remote sensing and Kirchhoff's law. 1. Laboratory measurements. J. Geophys. Res. 99, 11897–11911. http://dx.doi.org/10.1029/93JB03600.

Salisbury, J.W., Walter, L.S., 1989. Thermal Infrared (2.5-13.5 Um) Spectroscopic Remote Sensing of Igneous Rock Types on Particulate Planetary Surfaces. J. Geophys. Res. 94, 9192–9202. http://dx.doi.org/10.1029/JB094iB07p09192.

Sautter, V., Payre, V., 2021. Alkali magmatism on Mars: an unexpected diversity. C. R. Géosci. 353 (S2), 61–90. http://dx.doi.org/10.5802/crgeos.64.

Schmidt, F., Bourguignon, S., 2019. Efficiency of BRDF sampling and bias on the average photometric behavior. Icarus 317, 10–26. http://dx.doi.org/10.1016/j.icarus.2018.06.025, arXiv:1806.03898.

Schmidt, F., Fernando, J., 2015. Realistic uncertainties on Hapke model parameters from photometric measurement. Icarus 260, 73–93. http://dx.doi.org/10.1016/j.icarus.2015.07.002, arXiv:1506.08089.

Schröder, S.E., Grynko, Y., Pommerol, A., Keller, H.U., Thomas, N., Roush, T.L., 2014. Laboratory observations and simulations of phase reddening. Icarus 239, 201–216. http://dx.doi.org/10.1016/j.icarus.2014.06.010, arXiv:1701.05822.

Shepard, M.K., Cloutis, E., 2011. Laboratory measurements of band depth variation with observation geometry. In: 42nd Annual Lunar and Planetary Science Conference. In: Lunar and Planetary Science Conference, p. 1043.

Shepard, M.K., Helfenstein, P., 2007. A test of the Hapke photometric model. J. Geophys. Res. (Planets) 112 (E3), E03001. http://dx.doi.org/10.1029/2005JE002625.

Simon, A.A., Kaplan, H.H., Cloutis, E., Hamilton, V.E., Lantz, C., Reuter, D.C., Trang, D., Fornasier, S., Clark, B.E., Lauretta, D.S., 2020a. Weak spectral features on (101995) Bennu from the OSIRIS-REx Visible and InfraRed Spectrometer. Astron. Astrophys. 644, A148. http://dx.doi.org/10.1051/0004-6361/202039688.

Simon, A.A., Kaplan, H.H., Hamilton, V.E., Lauretta, D.S., Campins, H., Emery, J.P., Barucci, M.A., DellaGiustina, D.N., Reuter, D.C., Sandford, S.A., Golish, D.R., Lim, L.F., Ryan, A., Rozitis, B., Bennett, C.A., 2020b. Widespread carbon-bearing materials on near-Earth asteroid (101955) Bennu. Science 370 (6517), eabc3522. http://dx.doi.org/10.1126/science.abc3522.

Simonelli, D.P., Wisz, M., Switala, A., Adinolfi, D., Veverka, J., Thomas, P.C., Helfenstein, P., 1998. Photometric properties of PHOBOS surface materials from viking images. Icarus 131 (1), 52–77. http://dx.doi.org/10.1006/icar.1997.5800.

Stroud, R.M., Barosch, J., Bonal, L., Burgess, K., Cody, G.D., De Gregorio, B.T., Daly, L., Dartois, E., Dobrică, E., Duprat, J., Engrand, C., Harries, D., Hashiguchi, M., Ishii, H., Kebukawa, Y., Kilcoyne, A.D., Langenhorst, F., Lee, M.R., Nittler, L.R., Quirico, E., Okumura, T., Remusat, L., Sandford, S., Yabuta, H., Abe, M., Abreu, N.M., Bagot, P.A.J., Beck, P., Bejach, L., Bland, P.A., Bridges, J.C., Cymes, B.A., Dazzi, A., de la Peña, F., Deniset-Besseau, A., Enju, S., Enokido, Y., Frank, D.R., Gray, J., Haruta, M., Hata, S., Hicks, L., Igami, Y., Jacob, D., Kamide, K., Komatsu, M., Laforet, S., Leroux, H., Le Guillou, C., Martins, Z., Marinova, M., Martinez, J., Mathurin, J., Matsumoto, M., Matsumoto, T., Matsuno, J., McFadzean, S., Michikami, T., Mitsukawa, I., Miyake, A., Miyahara, M., Miyazaki, A., Montagnac, G., Mostefaoui, S., Nakamura, T., Nakato, A., Naraoka, H., Nakauchi, Y., Nakazawa, S., Nishimura, M., Noguchi, T., Ohtaki, K., Ohigashi, T., Okada, T., Okumura, S., Okazaki, R., Phan, T.H.V., Rebois, R., Sakamoto, K., Saiki, T., Saito, H., Seto, Y., Shigenaka, M., Smith, W., Suga, H., Sun, M., Tachibana, S., Takahashi, Y., Takeichi, Y., Takeuchi, A., Takigawa, A., Tamenori, Y., Tanaka, S., Terui, F., Thompson, M.S., Tomioka, N., Tsuchiyama, A., Tsuda, Y., Uesugi, K., Uesugi, M., Usui, T., Verdier-Paoletti, M., Wakabayashi, D., Watanabe, S.-i., Yada, T., Yamashita, S., Yasutake, M., Yogata, K., Yoshikawa, M., Yurimoto, H., Zanetta, P.-M., Zega, T., Zolensky, M.E., 2024. Electron microscopy observations of the diversity of ryugu organic matter and its relationship to minerals at the micro- to nano-scale. Meteorit. Planet. Sci. http://dx.doi.org/10.1111/maps.14128, arXiv:https://onlinelibrary.wiley.com/doi/pdf/10.1111/maps.14128. URL: https://onlinelibrary.wiley.com/doi/abs/10.1111/maps.14128.

Sultana, R., 2021. Propriétés Optiques d'Analogues des Surfaces des Petits Corps Primitifs du Système Solaire (Ph.D. thesis). URL: http://www.theses.fr/2021GRALU026. supervised by P. Beck Sciences de la Terre et de l'Univers et de l'Environnement Université Grenoble Alpes 2021.

Sultana, R., Poch, O., Beck, P., Schmitt, B., Quirico, E., 2021. Visible and near-infrared reflectance of hyperfine and hyperporous particulate surfaces. Icarus 357, 114141. http://dx.doi.org/10.1016/j.icarus.2020.114141, arXiv:2010.16136.

Sultana, R., Poch, O., Beck, P., Schmitt, B., Quirico, E., Spadaccia, S., Patty, L., Pommerol, A., Maturilli, A., Helbert, J., Alemanno, G., 2023. Reflection, emission, and polarization properties of surfaces made of hyperfine grains, and implications for the nature of primitive small bodies. Icarus 395, 115492. http://dx.doi.org/10.1016/j.icarus.2023.115492, arXiv:2302.10111.

Takir, D., Emery, J.P., 2012. Outer Main Belt asteroids: Identification and distribution of four 3-μm spectral groups. Icarus 219 (2), 641–654. http://dx.doi.org/10.1016/j.icarus.2012.02.022.

Takir, D., Matsuoka, M., Waiters, A., Kaluna, H., Usui, T., 2022. Observations of Phobos and Deimos with SpeX at NASA infrared telescope facility. Icarus 371, 114691. http://dx.doi.org/10.1016/j.icarus.2021.114691.

Takir, D., Reddy, V., Sanchez, J.A., Le Corre, L., Hardersen, P.S., Nathues, A., 2015. Phase angle effects on 3 μm absorption band on ceres: Implications for dawn mission. Astrophys. J. 804 (1), L13. http://dx.doi.org/10.1088/2041-8205/804/1/L13, arXiv:1504.02678.

Takir, D., Stockstill-Cahill, K.R., Hibbitts, C.A., Nakauchi, Y., 2019. 3-μm reflectance spectroscopy of carbonaceous chondrites under asteroid-like conditions. Icarus 333, 243–251. http://dx.doi.org/10.1016/j.icarus.2019.05.012, arXiv:1904.09453.

Vernazza, P., Beck, P., 2017. Composition of solar system small bodies. In: Elkins-Tanton, L.T., Weiss, B.P. (Eds.), Planetesimals: Early Differentiation and Consequences for Planets. pp. 269–297. http://dx.doi.org/10.1017/9781316339794.013.

Vinogradoff, V., Poggiali, G., Raponi, A., Ciarniello, M., De Angelis, S., Ferrari, M., Castillo-Rogez, J.C., Brucato, J., De Sanctis, M.-C., 2021. Laboratory investigations coupled to VIR/Dawn observations to quantify the large concentrations of organic matter on ceres. Minerals 11 (7), 719. http://dx.doi.org/10.3390/min11070719.

Wales, D.J., Doye, J.P.K., 1997. Global optimization by basin-hopping and the lowest energy structures of lennard-jones clusters containing up to 110 atoms. J. Phys. Chem. A 101 (28), 5111–5116. http://dx.doi.org/10.1021/jp970984n.

Wargnier, A., Gautier, T., Poch, O., Beck, P., Quirico, E., Buch, A., Drant, T., Perrin, Z., Doressoundiram, A., 2023a. Organic detection in the near-infrared spectral Phobos regolith laboratory analogue in preparation for the Martian Moon eXploration mission. Astron. Astrophys. 669, A146. http://dx.doi.org/10.1051/0004-6361/202245294.

Wargnier, A., Poggiali, G., Doressoundiram, A., Gautier, T., Beck, P., Buch, A., Ruscassier, N., Fornasier, S., Barucci, M.A., 2023b. Development of a new Phobos spectral simulant: spectral properties from visible to the mid-infrared range. Mon. Not. R. Astron. Soc. 524 (3), 3809–3820. http://dx.doi.org/10.1093/mnras/stad2132.

Wei, Q., Tang, Y., 2018. ^{13}C-NMR study on structure evolution characteristics of high-organic-sulfur coals from typical Chinese areas. Minerals 8 (2), 49. http://dx.doi.org/10.3390/min8020049.

Wong, I., Brown, M.E., Emery, J.P., Binzel, R.P., Grundy, W.M., Marchi, S., Martin, A.C., Noll, K.S., Sunshine, J.M., 2023. JWST near-infrared spectroscopy of the Lucy Jupiter Trojan flyby targets: Evidence for OH absorption, aliphatic organics, and CO_2. http://dx.doi.org/10.3847/PSJ/ad2fc3.

Yada, T., Abe, M., Okada, T., Nakato, A., Yogata, K., Miyazaki, A., Hatakeda, K., Kumagai, K., Nishimura, M., Hitomi, Y., Soejima, H., Yoshitake, M., Iwamae, A., Furuya, S., Uesugi, M., Karouji, Y., Usui, T., Hayashi, T., Yamamoto, D., Fukai, R., Sugita, S., Cho, Y., Yumoto, K., Yabe, Y., Bibring, J.-P., Pilorget, C., Hamm, V., Brunetto, R., Riu, L., Lourit, L., Loizeau, D., Lequertier, G., Moussi-Soffys, A., Tachibana, S., Sawada, H., Okazaki, R., Takano, Y., Sakamoto, K., Miura, Y.N., Yano, H., Ireland, T.R., Yamada, T., Fujimoto, M., Kitazato, K., Namiki, N., Arakawa, M., Hirata, N., Yurimoto, H., Nakamura, T., Noguchi, T., Yabuta, H., Naraoka, H., Ito, M., Nakamura, E., Uesugi, K., Kobayashi, K., Michikami, T., Kikuchi, H., Hirata, N., Ishihara, Y., Matsumoto, K., Noda, H., Noguchi, R., Shimaki, Y., Shirai, K., Ogawa, K., Wada, K., Senshu, H., Yamamoto, Y., Morota, T., Honda, R., Honda, C., Yokota, Y., Matsuoka, M., Sakatani, N., Tatsumi, E., Miura, A., Yamada, M., Fujii, A., Hirose, C., Hosoda, S., Ikeda, H., Iwata, T., Kikuchi, S., Mimasu, Y., Mori, O., Ogawa, N., Ono, G., Shimada, T., Soldini, S., Takahashi, T., Takei, Y., Takeuchi, H., Tsukizaki, R., Yoshikawa, K., Terui, F., Nakazawa, S., Tanaka, S., Saiki, T., Yoshikawa, M., Watanabe, S.-i., Tsuda, Y., 2021. Preliminary analysis of the Hayabusa2 samples returned from C-type asteroid Ryugu. Nat. Astron. 6, 214–220. http://dx.doi.org/10.1038/s41550-021-01550-6.

Yoldi, Z., Pommerol, A., Jost, B., Poch, O., Gouman, J., Thomas, N., 2015. VIS-NIR reflectance of water ice/regolith analogue mixtures and implications for the detectability of ice mixed within planetary regoliths. Geophys. Res. Lett. 42 (15), 6205–6212. http://dx.doi.org/10.1002/2015GL064780.